Printed Electronics from Solution-Processed 2D Materials

A THESIS PRESENTED BY

ADAM G. KELLY

UNDER THE SUPERVISION OF

PROFESSOR JONATHAN N. COLEMAN

FOR THE DEGREE OF

DOCTOR OF PHILOSOPHY

IN THE SUBJECT OF

PHYSICS

SCHOOL OF PHYSICS,

TRINITY COLLEGE DUBLIN

AUGUST, 2018

Declaration

I declare that this thesis has not been submitted as an exercise for a degree at this or any other university and it is entirely my own work.

I agree to deposit this thesis in the University's open access institutional repository or allow the library to do so on my behalf, subject to Irish Copyright Legislation and Trinity College Library conditions of use and acknowledgement.

Elements of this work that have been carried out jointly with others or by collaborators have been duly acknowledged in the text wherever included.

Adam Kelly

Printed Electronics from Solution-Processed 2D Materials

Abstract

The fervour created in the wake of the graphene gold-rush has fuelled investigative momentum over the last decade. The maturity of liquid-phase processing has meant that solution-processed layered crystals can be now be consolidated with additive manufacturing and devices based on printed nanosheet networks are now regularly reported. There are many challenges associated with printed architecture and this work aims to address the some of the issues faced by the current generation of nanosheet-network devices.

As contemporary printed devices move from lateral to vertical geometry, it was first necessary to develop a methodology for printing continuous, pinhole-free films to prevent unwanted interlayer contact. This was undertaken through a capacitor study where the devices were printed through sequential deposition of conductive graphene and dielectric hexagonal boron nitride (h-BN) nanosheet networks. Such heterostructures will only function as capacitors once the dielectric layer is continuous and, through trial and error, the dielectric layers were found to be pinhole-free at thicknesses above 1.65 μm. Impedance spectroscopy showed that such heterostructures act as series combinations of a capacitor and a resistor, with the expected dimensional scaling of the capacitance. The areal capacitance ranged from 0.24 to 1.1 nF cm^{-2}, with an average series resistance of 120 kΩ. The fitting of the Bode plots also provided an average *RC* time constant of 0.74 μs for these devices. This development thus paves the way toward more complex multilayer devices.

While a transistor based on a printed graphene network was demonstrated in 2012, there has been little progress on transistors based on printed semiconducting networks. This is likely due to the electrostatic gate field being screened by the network structure. A liquid electrolyte was thus used to electrolytically gate the entire volume of a printed network and the efficacy of this technique was demonstrated for printed films of MoS_2, WS_2, WSe_2, and $MoSe_2$. These networks showed mobilities of > 0.1 $cm^2\ V^{-1}\ s^{-1}$, on:off ratios of up to 600, and transconductances exceeding 5 milliSiemens. The transconductance was also found to scale with the thickness of the network, a feature atypical of traditional transistors. The large device capacitance, while hindering switching speeds, allows these devices to drive high

currents at relatively low drive voltages, in contrast with other devices of comparable mobility. An all-printed, vertically stacked transistor was then demonstrated with graphene source, drain, and gate electrodes, a WSe_2 channel, and a BN separator—all formed from nanosheet networks. The BN network contains the electrolyte within its porous interior, which facilitates electrolytic gating in a solid-like structure. This proof-of-concept transistor performs reasonably well, with an on:off ratio of ~ 25 and a transconductance of 22 μS.

With the aim of increasing the carrier mobility in nanosheet-network devices, MoS_2–graphene composites were investigated as active regions in printed photodetectors. Combining liquid exfoliation and inkjet printing, all-printed photodetectors were fabricated with graphene electrodes and MoS_2–graphene composite channels with various graphene mass fractions ($0 \leqslant \mathcal{M}_{f,G} \leqslant 16$ wt%). The increase in dark conductivity of the channel with $\mathcal{M}_{f,G}$ was consistent with percolation theory for composites below the percolation threshold. While the photoconductivity increased with graphene content, it did so more slowly than the dark conductivity, such that the fractional photoconductivity decayed rapidly with increasing $\mathcal{M}_{f,G}$. This indicates that both mobility and dark carrier density increase with graphene content according to percolation-like scaling laws, while photo-induced carrier density is essentially independent of graphene loading. These data show that analysis of the photoconductivity in such composites is a useful way to differentiate the effects of filler content on mobility and carrier density, parameters which are usually aggregated in the conductivity.

List of Publications

1. Kelly, A.G., Finn, D., Harvey, A., Hallam, T., & Coleman, J.N. (2016). All-printed capacitors from graphene-BN-graphene nanosheet heterostructures.* *Applied Physics Letters*, 109(2), 023107.
   *Basis for Chapter 4

2. Backes, C., Higgins, T.M., Kelly, A.G., Boland, C., Harvey, A., Hanlon, D., & Coleman, J.N. (2016). Guidelines for exfoliation, characterization and processing of layered materials produced by liquid exfoliation. *Chemistry of Materials*, 29(1), 243-255.

3. Harvey, A., Boland, J.B.., Godwin, I., Kelly, A.G., Szydłowska, B.M., Murtaza, G., Thomas, A., Lewis, D.J., & Coleman, J.N. (2017). Exploring the versatility of liquid phase exfoliation: producing 2D nanosheets from talcum powder, cat litter and beach sand. *2D Materials*, 4(2), 025054.

4. Kelly, A.G., Hallam, T., Backes, C., Harvey, A., Esmaeily, A. S., Godwin, I., Coelho, J., Nicolosi, V., Lauth, J., Kulkani, A., Kinge, S., Siebbeles, L.,Duesberg, G., & Coleman, J.N. (2017). All-printed thin-film transistors from networks of liquid-exfoliated nanosheets.* *Science*, 356(6333), 69-73.
   *Basis for Chapter 5

5. Kelly, A.G., Murphy, C., Vega-Mayoral, V., Harvey, A., Esmaeily, A.S., Hallam, T., McCloskey, D., & Coleman, J.N. (2017). Tuneable photoconductivity and mobility enhancement in printed MoS_2/graphene composites.* *2D Materials*, 4(4), 041006.
   *Basis for Chapter 6

6. Mondal, S., Dutta, K., Dutta, S., Jana, D., Kelly, A.G., & De, S. (2018). Efficient Flexible White-Light Photodetectors Based on $BiFeO_3$ Nanoparticles. *ACS Applied Nano Materials*, 1(2), 625-631.

7. Ryan, A. J., Kearney, C. J., Shen, N., Khan, U., Kelly, A.G., Probst, C., Loskill, P., Kelly, D.J., Coleman J.N., & O'Brien, F.J. (2018). Electroconductive Biohybrid Collagen/Pristine Graphene Composite Biomaterials with Enhanced Biological Activity. *Advanced Materials*, 30(15), 1706442.

Acknowledgements

I would like to begin by thanking Johnny for providing me with the opportunity to work with such an amazing group. I began this PhD believing that undergrad shenanigans were over and it was time to grow up however, I felt this going out the window the fifth time The Pav was mentioned during my interview. Over the last four years, I have always left a meeting feeling better about terrible results and always appreciated the focus and clarity that Johnny could bring to frustrating research.

I want to thank Toby for mentoring me on all things electronic. When I started, he mentioned that each PhD comes with about €20k worth of breakage so, in my last month, I think I'll take out my underspend on the Temescal. Thanks to Claudia, a patient fountain of knowledge on everything nano and for providing proper etiquette on the consumption of lab wine. A big thanks to Tom, for providing the central question of this thesis and for having no qualms about going to the pub at 11 am on the only sunny day of the year. Umar, the scientific equivalent of MacGyver from whom I learned the fine art of brute force experimentation—there is no exact science in preliminary investigation. I started my PhD paired with Graeme who taught me a bunch of things he found useful including, but not limited to, Fibbers on a Sunday. To Seb, Conor, and Dan in the office, you may brighten up five days of the week but I still feel blameless over us being told to stop using the upstairs toilet. To the rest of the group; JB, Andrew, Sonia, Aideen, Dave, Cian, Ruiyuan and Victor, I'm deeply grateful for being able to share the last four years with you. To Yash and Domhnall, you've landed on your feet with these guys. A big thanks as well to Niall and all in the ASIN group for providing me with relentless access to their labs and equipment.

To all my friends outside of Trinity, I'm pretty sure the last four years count as attempted murder on your behalf but I wouldn't change a single pint with you degenerates.

To Kejt, thank you for putting up with me over the past few years and, since I couldn't have done this without you by my side, I'll say this; te słowa są po polsku.

Finally, the biggest thanks of all to my family for the various types of support over the last 8 years. The ups and downs would have been unnavigable and this thesis would have been unachievable without you.

I'm still not getting a real job.

Contents

List of Figures

To my family and friends,
this journey could not be made alone...

A recurrent theme is that luck plays a large role in every story of success; it is almost always easy to identify a small change in the story that would have turned a remarkable achievement into a mediocre outcome.

Daniel Kahneman

1

Introduction

The frenetic pace of change in the 20th century has caused some of the largest paradigm shifts seen by this age of human civilisation. In the span of a lifetime, we have gone from the first manned flight to a manned space station, from hardback encyclopaedias to instantaneous access to the entire human archive, and from floppy disks to credible fears over artificial intelligence. It is clear that the pace of progress is

rapidly accelerating and this acceleration maps extremely well to the emergence of the field of nanoscience and, in particular, of 2D materials.

Nanoscience is the umbrella term covering both the materials and their technology and has tendrils extending back thousands of years—complexity is ever built on the shoulders of giants. The fields of nanoscience, chemistry, material science, and many fields of engineering have a common ancestor in early metallurgy as various nanomaterials were commonplace during classical antiquity. Swords forged from Damascus steel were fortified with carbon nanotubes, Mesopotamian pottery and Egyptian glassware contained colloidal nanoparticles to create iridescent patterns, and clays have long been used by indigenous tribes as medicinal, digestive, and cosmetic aids.[1]

The synthesis of fullerenes and carbon nanotubes consolidated nanoscience with material science during the 90s but it was the isolation of graphene from a graphite crystal that drove the hype that culminated in the Nobel Prize in 2010. This has catalysed investigation to the point where nanoscience publications now comprise > 5% of all scientific publications and, for better or worse, the number of nanoscience journals now numbers over 300. There has been so much certainty over the potential of these materials that an offhand comment by a colleague has become the central question of this thesis:

> "What if it turns out that 2D materials are just shit?"

This was personally startling but requires consideration given the youth of the field. The development of silicon-based electronics has built the world around us and it is extremely unlikely that 2D materials will be able to compete in the near- to mid-term but this is far from the only route to application.[2] The Internet of Things means we are likely to see electronics embedded in every aspect of our lives and this will require cheap,

semi-disposable devices. This brings many challenges which could potentially be addressed through the emergence of additive manufacturing and, in particular, its subfield of printed electronics. Printed electronics are currently based on organic polymers and this technology has now commercially matured. However, the performance of these materials is intrinsically limited which means that a research space is available where 2D materials may be able to compete within in the near future. Beyond this, the growing demand to power our world would be greatly served through the energy generation and storage capabilities of these materials. Thus, the field, and this thesis, are currently striving to answer the above question and to hopefully fulfil the potential of the nanoscale platform.

With this in mind, the aim of this work is to take steps towards addressing a prevailing challenge; effective current modulation in a semiconducting 2D network. While current modulation was shown in a printed graphene network in 2012, it is critical to demonstrate the same with a semiconductor, but progress here has been limited. This points to the complexity of the problem as many material, ink, and device issues must be resolved. One such issue concerns the nature of printed 2D networks; as they are composed of discrete particles, the networks are prone to discontinuities, or pinholes. This is a major issue as the device architecture pivots from planar to vertical and a protocol for vertical layering is thus presented in Chapter 4. This is developed through a printed capacitor study as device functionality can only be achieved once the dielectric film is continuous.

The slow progress on printed transistors can be partially attributed to the gating method. A thick 2D network will shunt a gate field meaning current modulation is confined to a relatively thin layer of material at the oxide interface. It it much more effective to use a liquid electrolyte that can fully penetrate the internal free volume as the entire network can

then be gated. The liquid electrolyte creates an enormous device capacitance which allows large currents to be driven despite the long device channels. Chapter 5 presents a method for electrolytically gating a printed 2D network and four semiconducting materials are characterised in this manner. This, integrated with the work in Chapter 4, then facilitates the demonstration of a fully printed, 2D-network transistor.

As the mobility of these devices is relatively low, much future work will focus on raising the network mobility to that of its individual constituents. A simple way to achieve this could be through a conductor/semiconductor composite where the conductive components are only present below the percolation threshold. Chapter 6 investigates the viability of this proposal through a percolation study of printed photodetectors with various graphene loadings blended into an MoS_2 network.

This thesis will conclude by reviewing the main findings and suggesting a direction for future investigations. It is hoped that the work presented herein will add value to the existing literature and facilitate further development of printed 2D electronics.

*A small note on this thesis; to preserve the flow of the narrative, the traditional Methods and Characterisation section containing descriptions of the scientific machinery has been distributed throughout the text. The techniques fundamental to the generation of 2D materials and their deposition are described in the introductory chapters with the secondary characterisation techniques described in Appendix A. On nomenclature; the term *graphene* may sloppily refer to either mono- or few-layer graphene nanosheets, dependent on context.

A scientist looking at non-scientific problems is just as dumb as the next guy.

Richard Feynman

2

2D Materials and their Synthesis

The class of materials known as layered crystals has been the focus of an enormous amount of research since the field's renaissance in 2004. While 1D nanomaterials such as carbon nanotubes have been heavily investigated since the 1980s, it was not until the unambiguous demonstration of a free-standing graphene monolayer in 2004 that 2D materials became a prominent area of research. 2D materials, in

contemporary terms, are those in which wavefunctions experience quantum confinement in a single dimension meaning an electron gas is free to move in an 'infinite' 2D plane. These planes, when stacked upon one another, form a layered crystal characterised by strong covalent bonding within the layer and weak van der Waals bonding between the layers. It is this weak interlayer bonding that allows discrete layers to be exfoliated from the bulk crystal to create free-standing monolayers. This characteristic is perhaps most commonly seen in pencilled text as the graphite crystal is shorn from pencil to page. When so isolated, the discrete monolayers show vastly different properties from their bulk form and it is these monolayer properties to which the word 'exciting' is romantically ascribed.

Despite the global abundance of various layered crystals, the synthesis of exfoliated 2D materials in practical quantities has been far from trivial. The seminal graphene paper used adhesive tape to peel nanosheets from bulk crystals and this remains an excellent method for producing high quality flakes. However, the extreme tedium and low throughput make it impractical and thoroughly incompatible with scalable manufacturing. This generally applies to bottom-up synthesis where bulk crystals are grown from an elemental precursor. A research space was thus available where existing solution processing strategies could be adapted to exfoliate large amounts of material in liquids. The liquid environment offers many advantages as dispersed media can easily be chemically modified, sorted by mass, formed into composites, and, importantly, refined into inks for deposition with a variety of established techniques. This chapter will begin by describing the characteristics of the materials, with a focus on electronic properties, and then move on to describe how layered crystals can be exfoliated and processed using a liquid medium.

2.1 The Electronic Characteristics of the 2D Family

Graphene is the face that launched a thousand grant proposals but the scope of investigation has encompassed the entire class of layered crystals in recent years. Within the family of layered materials, there is much diversity across crystal structure and stoichiometry leading to a variety of commensurate properties such as electrical conductors and semiconductors, dielectrics, ferromagnetics, catalysts, and thermoelectrics. Transition metal dichalcogenides (TMDs), transition metal oxides (TMOs), 2D compounds such as boron nitride, and single-element 2D structures such as arsenene have all featured in the literature with increasing regularity over the past decade. Such versatility across the electronic properties makes 2D materials extremely attractive for electronic applications. Within the TMDs, for example, the coordination and oxidation of the metal atoms determine whether the material will be metallic, semi-metallic, or semiconducting. This has generated much excitement as each part of an electronic device, such as the electrodes or active channel, can be constructed using a network solely composed of 2D materials.

2.1.1 Semi-metals

The story of graphene contains at its heart the power of the scientific framework, where long-standing acceptance is upended by new discovery. Beginning in the 1930s, theoretical analyses of layered crystals argued that a monolayer could not exist in isolation due to thermodynamic instability. The monolayer was modelled as a completely flat atomic sheet and, under this condition, thermal vibrations create anomalously large atomic displacements which cause the monolayer to disintegrate. Indeed, this certainly appeared to be the case as seventy years of empirical investigation could not create a free-standing

monolayer, but this was far from an impediment to general investigation. In 1947, PR Wallace calculated the band structure and linear dispersion relation of the monolayer limit of graphite, noting its semi-metallicity where free electrons "are created at higher temperatures by excitation to a band contiguous to the highest one which is normally filled."[3] Despite the apparent impossibility of creating a free-standing monolayer, its properties could still be probed as part of the parent graphite crystal and various crystallographic features were experimentally confirmed using transmission electron microscopy and x-ray diffraction.[4] It was in the infancy of carbon nanotube research that the term 'graphene' was first used to describe a graphite monolayer but, partly due to the newly discovered properties of carbon nanotubes, research into layered crystals had slowed. The field gained a second wind when Andre Geim and Konstantin Novoselov definitively isolated a monolayer of graphene (shown in Figure 2.1A) and, more importantly, patterned the samples with Hall bars to report the remarkable electronic properties.[5] They also reconciled the existential problem by showing that graphene is slightly corrugated rather than completely flat which suppresses thermal vibrations and stabilises the monolayer.[6]

Graphene crystallises as a honeycomb lattice composed of sp^2-hybridised carbon atoms, shown in Figure 2.1B.[7] Three electrons form deep valence bonds with the neighbouring atoms leaving a remaining electron, corresponding to a non-hybridised *p*-state perpendicular to the structure, to contribute to the conductivity of the system.[8] The strength of the hybridised sigma bonds makes the carbon atoms in the sheet extremely robust against dislocation meaning crystallographic defects are rare in the basal plane. The lack of lattice impurities means charge carriers can experience ballistic transport for distances over a micron—provided external scattering mechanisms can be screened.[5]

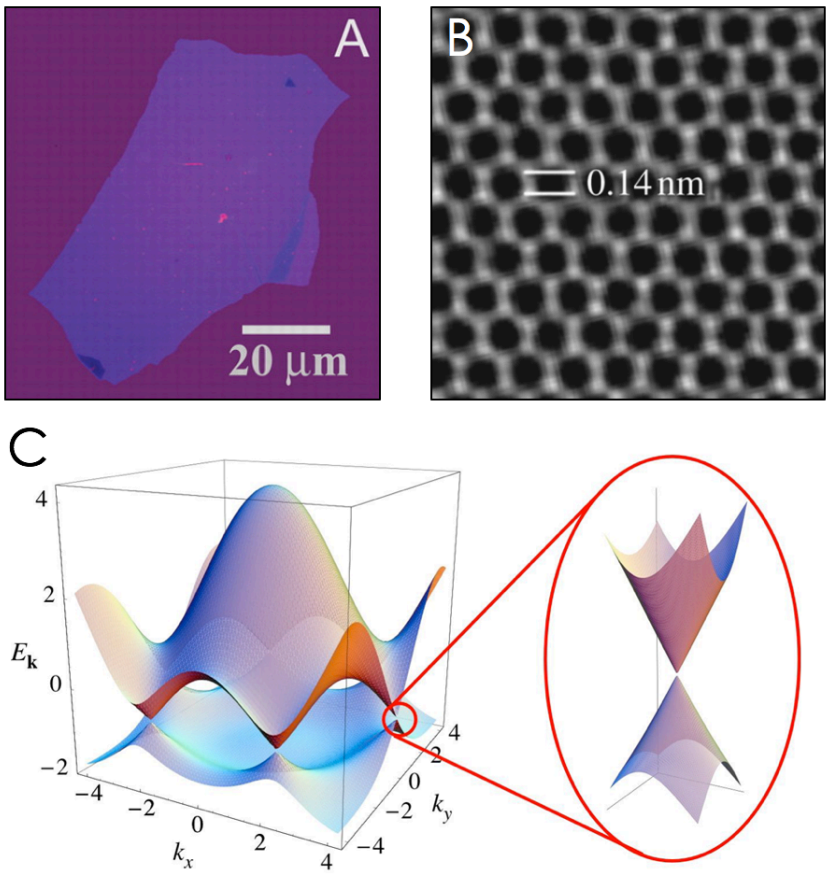

Figure 2.1: Graphene. A) AFM of the one of the first free-standing monolayers. Image from Ref. (5). B) A TEM image of the graphene lattice showing the 0.14 nm C-C bond length. Image from Ref. (7). C) The dispersion relation of graphene. The linearity at the Dirac points is shown magnified. Image from Ref. (8).

Scattering artefacts pose a significant problem as ultra-thin crystals are particularly sensitive to features such as dielectric mismatch which can significantly alter the Coulomb potential, surface roughness which affects mobility through a sixth power law, and nanosheet edges which can induce long-range Coulomb scattering.[9]

The ease in carrier transport across the basal plane is also due to to the non-negligible overlap between the orbitals of neighbouring atoms which allows the electron to form

extended states spanning over multiple in-plane sites.[8] This does not apply to vertical transport through the crystal however, as research into graphite has revealed over a thousand-fold anisotropy between in-plane and out-of-plane conductivity.[10] This is due to the interlayer van der Waals bond acting as a tunnelling barrier rather than an anisotropy in the effective mass and is a feature common to all layered crystals.

Graphene's semi-metallicity arises from the structure of its electronic bands at the vertices of the hexagonal lattice, shown in Figure 2.1C. For small excitations at these vertices, known as Dirac points, the dispersion relation is linear (shown expanded in Figure 2.1C). A consequence of a linear dispersion relation is a zero effective electron mass and the Dirac nomenclature is not simply an honorific but refers to the similarity in physical description to quantum electrodynamics (QED) for massless fermions.[6] This means that QED effects can present on a graphene sheet, albeit scaled by c/300.[8] These features confer an enormous in-plane mobility; the seminal graphene paper reported a mobility of ~ 10,000 $cm^2\ V^{-1}\ s^{-1}$ and, using clever screening techniques, values are now often reported > 250,000 $cm^2\ V^{-1}\ s^{-1}$ (*cf.* silicon ~ 3000 $cm^2\ V^{-1}\ s^{-1}$).[11]

The wealth of publications during the graphene gold-rush strove to find where graphene would be best suited in the short term. In Geim and Novoselov's follow up paper in 2007,[6] they point out

> Despite the reigning optimism about graphene-based electronics, 'graphenium' microprocessors are unlikely to appear for the next 20 years. In the meantime, many other graphene-based applications are likely to come of age. In this respect, clear parallels with nanotubes allow a highly educated guess of what to expect soon.

This prediction has been mostly fulfilled as commercial graphene applications are composite-based and polymers can be rendered conductive at less than 2% loading.[12] In the much broader field of device prototyping, ease of synthesis and the wealth of global experience has meant graphene is frequently used as an electrical conductor in 2D electronics.

2.1.2 Semiconductors

The discovery of a stable monolayer of graphene was in many ways the keys to the kingdom. It was immediately obvious that other layered crystals could be exfoliated in a similar manner and a range of stable monolayers were published the following year.[13] Among these was molybdenum disulphide (MoS_2), an inorganic layered compound first studied in the 1920s.[14] MoS_2 belongs to a subclass of layered crystals called transition metal dichalcogenides (TMDs) which, like graphite, show an exceptional set of properties as the crystal is scaled down to the monolayer.

TMDs crystallise in a generalised MX_2 stoichiometry, where M refers to a transition metal and X refers to a chalcogen of sulphur, selenium, or tellurium. Forty combinations of the elements highlighted in Figure 2.2A form layered crystals, each of which has a unique chemistry and band structure; from insulators such as HfS_2, semiconductors such as MoS_2 and WS_2, semi-metals such as WTe_2 and $TiSe_2$, to metals such as NbS_2 and VSe_2.[15] While graphene is formed of a single plane of carbon atoms, a TMD monolayer consists of a hexagonal plane of transition metal atoms contained between two offset hexagonal planes of chalcogen atoms in the form X-M-X (Figure 2.2B). This monolayer structure is ~ 0.7 nm thick[16] (*cf.* graphene ~ 0.35 nm) and stacks through van der Waals bonding to form a bulk

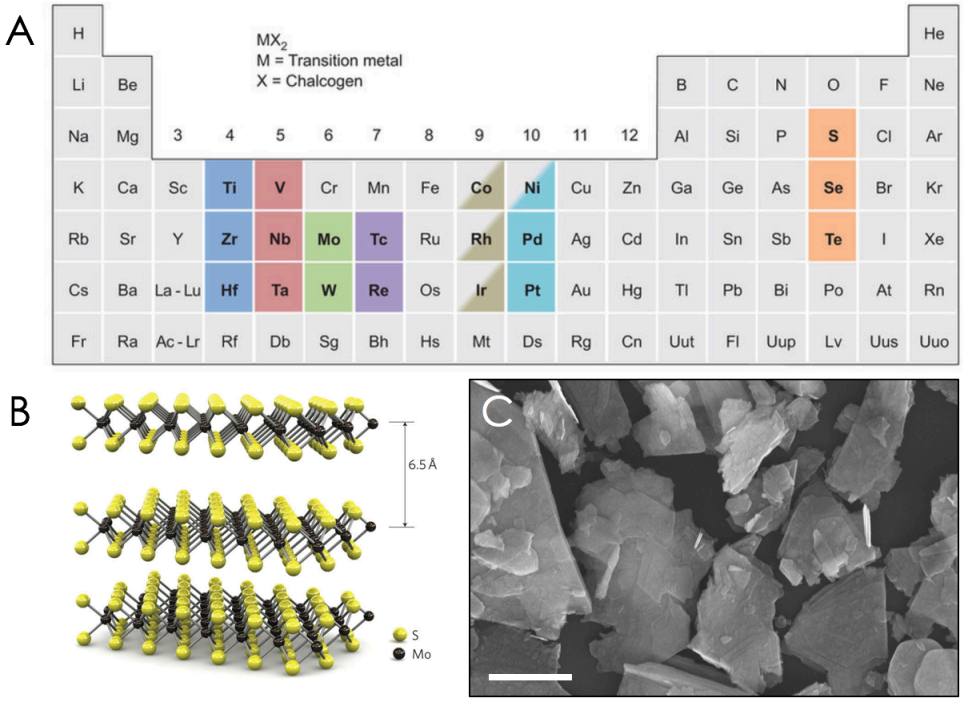

Figure 2.2: Transition metal dichalcogenides. A) Table of TMD elements. Image from Ref. (15). B) Schematic of a TMD crystal. Image from Ref. (16). C) An SEM image of MoS_2 bulk powder.

crystal. The bulk crystals themselves are typically a messy affair (Figure 2.2C) as they are composed of a broad distribution of monolayer lengths—far from the uniformity depicted in adjacent rendering.

Although all layered TMDs are composed of hexagonal planes, the X-M-X structure is not isomorphic across the various metals and chalcogens; a thermodynamically-preferable unit cell depends on the metal and chalcogen bonds leading to a variety of *polymorphs*. Further, each layer in a bulk crystal can be stacked in a number of different sequences leading to a variety of *polytypes*. The most common polymorphs are 1T (trigonal), 2H (hexagonal), and 3R (rhombohedral). Here, the integer refers to the number of monolayers in the unit cell, and each of these polymorphs can then be stacked into the various

polytypes. The 2H polymorph of MoS_2, for example, can be stacked in three different polytypes. Monolayer TMDs show only two polymorphs—trigonal prismatic and octahedral, shown in Figure 2.3A. MoS_2 is most commonly found in the semiconducting 2H phase with AbA BaB stacking (Figure 2.3A) but a metallic 1T phase with AbC AbC stacking can be induced at certain pressures and temperatures.[17]

Moving from Group IV to Group X across the transition metals corresponds to a filling of the *d*-states, and it is the *d*-electron count that gives rise to the electronic diversity. Deep covalent bonding between the metal and chalcogen *s*- and *p*-states results in bonding (σ) and anti-bonding (σ^*) bands (Figure 2.3B) and contained between these are the *d*-bands whose filling produces the semiconducting, metallic, or insulating behaviour.[15] When the *d*-bands are partially filled, the TMD (such as 2H-$NbSe_2$ and 1T-ReS_2) exhibits metallic conductivity. The 2H phase of Group VI TMDs, such as MoS_2 and WS_2, has a filled d_z-band leaving the Fermi level located between bands (Figure 2.3B) resulting in semiconducting behaviour.[18]

The band structures of the Group VI TMDs have now been heavily reported, typically using MoS_2 as a model system for the other Group VI compounds. Despite being isoelectronic, the tungsten-based compounds contain higher energy band structures compared to their molybdenum analogues due to the higher energy of filled 5*d*-state compared to the 4*d*-state.[19] The semiconducting Group VI TMDs are of particular interest not simply because of their abundance, in terms of both physical material and in the academic literature, but because of their distinct transition in electronic behaviour as the crystal is exfoliated down to the monolayer. The band structure at the Γ point of the Brillouin zone of MoS_2 contains a considerable contribution from chalcogen p_z-states that act perpendicularly to the basal plane. The exfoliation of layers from the bulk crystal thus

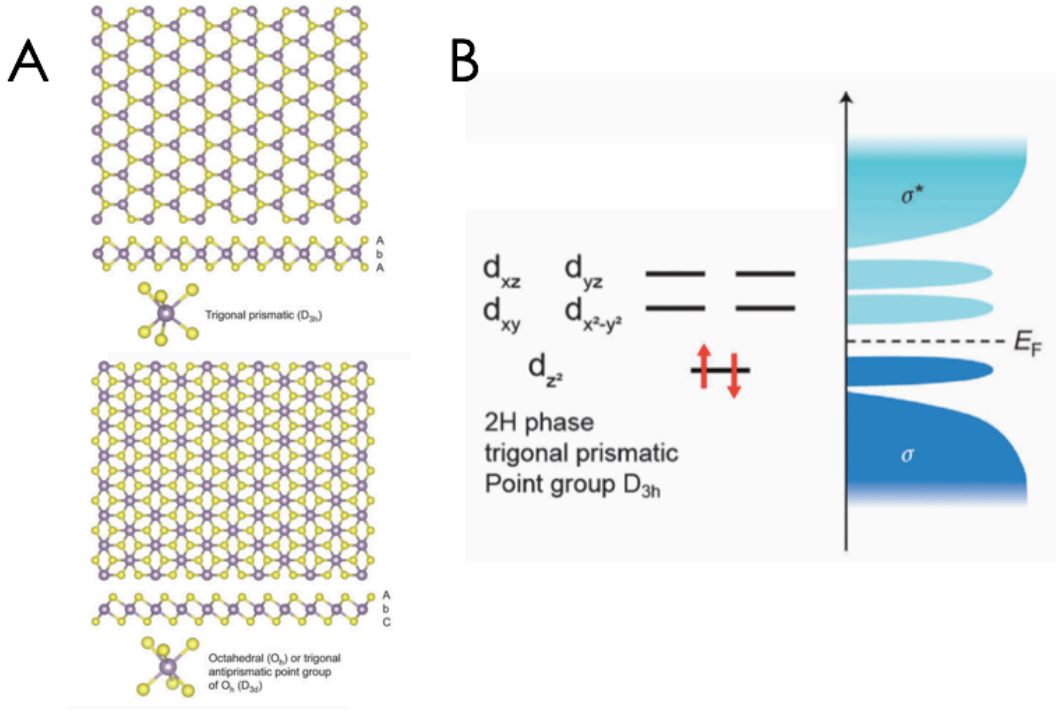

Figure 2.3: TMD band structures. A) TMD lattice structures with two different polymorphs. Image from Ref. (15). B) The band filling of Group VI TMDs. Image from Ref. (18).

has the effect of depressing the valence band maximum and raising the conduction band minimum.[20] This bandgap-widening is shown for MoS_2 in Figure 2.4 where the bulk gap of ~ 1.2 eV widens to ~ 1.8 eV in monolayer and this 50% increase is generally the case for other Group VI compounds.[15] Perhaps the most striking difference between the bulk and monolayer band structures is the transition of the bandgap from indirect to direct. With decreasing layer number, the indirect bandgap shifts upwards by ~ 0.6 eV causing a crossover to a direct-gap material in the monolayer limit and the enhancement in photoluminescence is extreme; the luminescent quantum efficiency has been reported to increase by 10^4.[21] The direct bandgaps of the Group VI monolayers are also well matched to the visible spectrum putting these materials at the heart of many recent optoelectronic

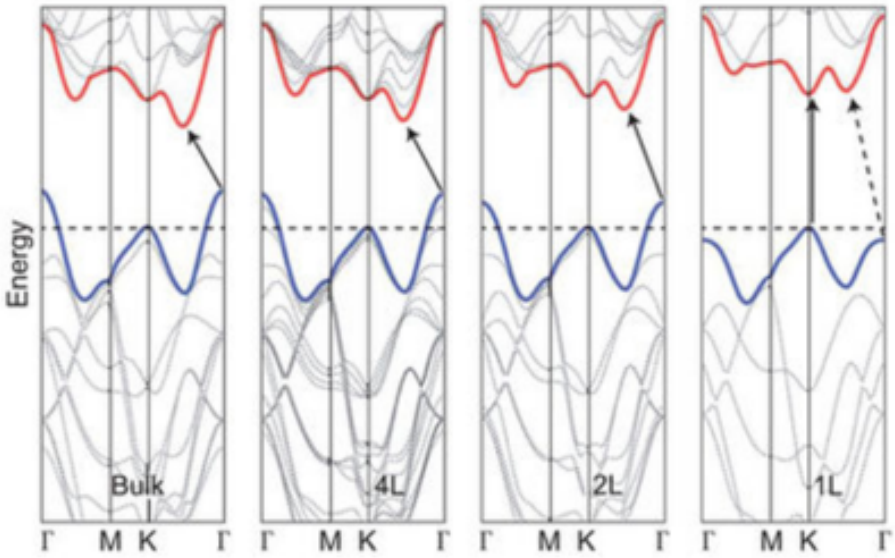

Figure 2.4: Bandgap transition with layer number. The bandgap transition from indirect to direct as the crystal is exfoliated down to the monolayer. Image from Ref. (15).

applications.[22,23,24]

The chalcogen atoms that terminate the surface layers are absent of dangling bonds which confers good ambient stability but this does not imply a high electronic quality. The most commonly reported material defects are chalcogen vacancies and anti-site substitutions (an S atom replaced by a Mo atom in MoS_2, for example) and the native n-type behaviour seen in MoS_2 has been attributed to donor states arising from such chalcogen vacancies.[25] The effect of vacancy density on charge transport is significant and this random crystallographic disruption is the suggested cause of the discrepancy in the mobility values across seemingly identical devices.[26] Furthermore, the electrical properties of Group VI devices are also known to be highly sensitive to extrinsic effects arising from surfaces and interfaces such as metal contacts, surface adsorbates, dielectric interfaces, and surface defects.[9]

The mobility of TMDs is modest compared to graphene in part due to the high vacancy density but also a far higher effective charge carrier mass. In particular, it is the intrinsic energy bandgap that has ensured that semiconducting TMDs have featured prominently in the device literature over the past decade. The mobility extracted from mono- to few-layer Group VI TMDs is on the order of several hundred $cm^2\ V^{-1}\ s^{-1}$ with the higher values coming from heavily engineered devices.[27,28,29] Das *et al.* appear to hold the state-of-the-art mobility of $\sim 700\ cm^2\ V^{-1}\ s^{-1}$ with a back-gated MoS_2 transistor and an atomic-layer deposited Al_2O_3 dielectric.[30] Such benchmark devices are hardly made in a scalable manner (yet) however there is clear value in finding the performance ceiling as the characterisation of TMD electronics is still in its infancy.

2.1.3 Insulators

While much of the focus of investigation has been on characterising and modulating current flow through the 2D materials, it is of critical importance to have non-conductive regions within the electronic architecture. There are a large variety of insulating materials available within the family of layered crystals, from everyday products such as talcum powder and cat litter,[31] to synthetically produced boron nitride (BN). It was long believed that BN did not occur naturally as elemental boron did not form any part of an essential mineral until the discovery of a rock fragment containing the cubic form of BN in southern Tibet in 2009.[32] The lack of natural occurrence did not preclude lab synthesis however and the layered, hexagonal form of BN, h-BN, has been used in cosmetics since at least the 1940s.[33]

h-BN is strongly analogous to graphite and displays almost identical crystallographic

properties leading to much of the same physical behaviour such as large thermal conductivity, chemical stability, and robust mechanical properties.[34] Like graphite, a monolayer of h-BN can be shaped into a range of nanoscale dimensionalities, each with their own physical and electronic properties (Figure 2.5A). The first nanoscale investigation of the h-BN lattice was in the form of nanotubes[35] and, shortly after the seminal graphene paper, the bulk crystal was soon exfoliated into a free-standing monolayer.[13]

Like graphene, the h-BN monolayer is characterised by deep in-plane sigma bonds formed by hybridisation of the $2s$-, $2p_x$-, and $2p_y$-states leaving the non-hybridised out-of-plane $2p_z$-state to weakly interact with adjacent layers. While these bonds are purely covalent in graphene, electrons are transferred from the boron to the nitrogen sites due to their difference in electronegativity.[36] This charge transfer is an important difference as it brings an ionic character to the bonds but also opens up a wide bandgap in the electronic structure. Despite much study on the subject, the nature of the h-BN bandgap remained elusive as ab initio calculations, predicting an indirect bandgap, could not be reconciled with optical experiments which indicated a direct gap. This was only resolved in 2016 by Gil *et al.* who conclusively demonstrated an indirect bandgap at 5.955 eV.[37]

The discrepancy in reporting on the h-BN bandgap goes beyond merely direct/indirect as values for the gap itself typically range from 5.5–6 eV.[38] The reason for this lies in the variance of stacking orders which is influenced by the ionic bonds within the basal plane (Figure 2.5B). Compared to graphene, the energetic landscape of a h-BN basal plane is heavily corrugated due to the non-uniform distribution of charge across the atomic sites.[36] In a bulk h-BN crystal, the van der Waals interaction will fix the interlayer distance at 0.33 nm but the individual layers can then slide into an energetically favourable stacking order

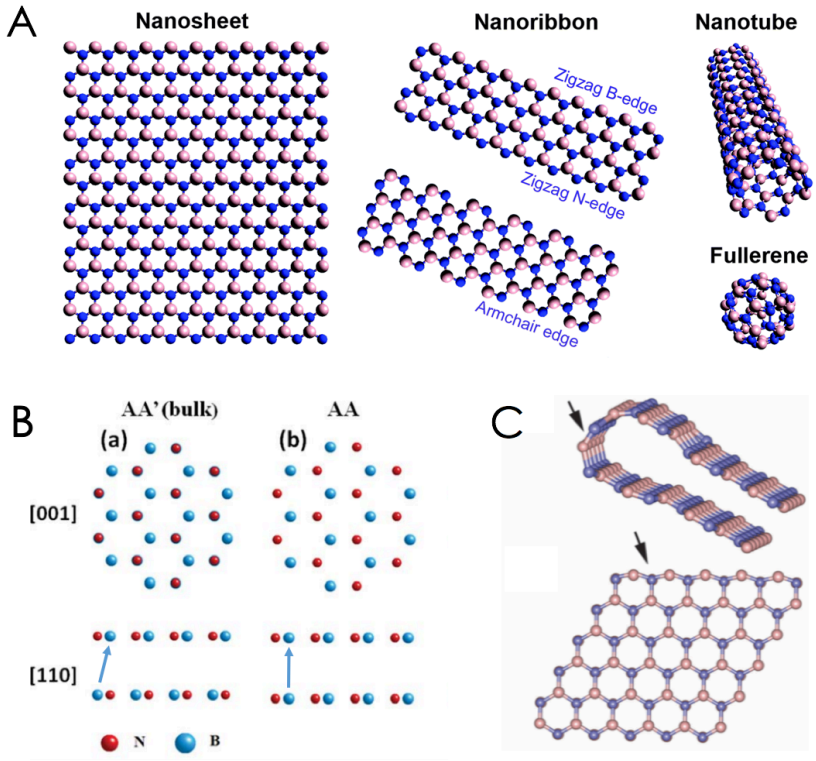

Figure 2.5: Boron nitride. A) The various structures that can be formed from a boron nitride nanosheet. Image from Ref. (33). B) The stacking arrangements that can lead to the variation in observed bandgap. C) The formation of an interlayer bond, or lip-lip interaction. Image from Ref. (33).

governed by the ionic landscape of their basal planes. As one layer is translated across another—at the fixed distance—the bandgap can vary by up to 0.6 eV.[39]

Another effect of the ionic bond is the formation of interlayer chemical bonds, something relatively infrequent with the C-C bonds in graphene. It has been shown that zigzag edges of two h-BN monolayers can bond (a "lip-lip" interaction) resulting in a structure akin to a folded-over monolayer (Figure 2.5C). By decreasing the number of edge sites, the conjoined bilayer reaches an energy minimum and greater structural stability.[40] It has also been suggested this has the effect of reducing the number of frustrated bonds (B-B

or N-N, instead of a lower energy B-N) which leads to more pristine basal planes.[38] The anchoring of monolayers through these lip-lip interactions may also contribute to the frustratingly low abundance of monolayer h-BN generated from top-down synthesis.

h-BN has seen its greatest value when used in conjunction with other 2D materials as an atomically-flat dielectric interface has been vital in setting benchmarks. The absence of dangling bonds and surface charge traps has meant a graphene device shows a roughness decrease of ~ two orders of magnitude leading to enormous improvements in charge transport compared to similar devices on SiO_2.[41] This has allowed heterostructures of h-BN/graphene/h-BN to exhibit mobilities of ~ 500,000 $cm^2\ V^{-1}\ s^{-1}$.[42]

2.2 Synthesis

Since 2004, the renewed interest in layered crystals has brought with it a commensurate explosion of research into monolayer production. The superlative properties demonstrated with 2D crystals relied on high quality, pristine samples that were peeled from a bulk crystal using adhesive tape. While mechanical exfoliation creates extremely high quality monolayers, it suffers from low yields and production rates. This may be suitable for proof of concept but an abundance of synthesis strategies have been developed in the intervening years as 2D materials grow from infancy to industry. These strategies can be broadly split into either bottom-up or top-down, depending on how one generates the monolayer.

A comparison between emergent 2D materials and silicon-based technologies was inevitable once the extent of the electronic properties became clear. The king's ransom invested in fabrication units by companies such as Intel and Samsung means industry has a strong preference for synthesis that is compatible with existing hardware. This is where

bottom-up strategies such as chemical vapour deposition (CVD) have shown great promise for monolayer growth. CVD uses a high temperature furnace to react (or decompose) a vapour-phase precursor with a metal powder or bare substrate. MoS_2, for example, can be grown by sulphurisation of evaporated metal films, although this lacks the finesse of modern CVD.[43] While early iterations of CVD-grown materials were heavily polycrystalline, wafer-scale single-crystal growth has now been demonstrated for monolayer graphene,[44] MoS_2,[45] and WS_2.[46] It is clear that CVD approaches show potential for many high-end electronic applications, however its scalability may be limited by furnace sizes, substrate area, and substrate material.[47] Other bottom-up methods such as epitaxial growth and ALD suffer from similar drawbacks. Furthermore, bottom-up synthesis is simply not an optimal approach for generating a sufficient amount of material for use in applications such as polymer[48] or glass[49] composites or energy storage applications whose properties scale with surface area.

The top-down approach to monolayer synthesis is generally referred to as exfoliation where a layered crystal is processed into discrete nanosheets. The early TMD work in the 1960s was often performed on nanosheets that were peeled from the parent crystal using adhesive tape.[50] While mono- or few-layer nanosheets may have then been exfoliated, the resolution of the available instrumentation was unable to definitively identify them until the efforts of Geim *et al.* in 2004. The difficulty in processing monolayers created by mechanical exfoliation is a major bottleneck in the production rate and, like the early days of carbon nanotube (CNT) research, generating a large quantity of material posed a significant challenge. This issue is present in both bottom-up and top-down synthesis but can be addressed by drawing upon knowledge developed for CNT synthesis.

2.2.1 Solution Processing of 2D Materials

The large amount of processing and analysis possible on liquid-dispersed media has made solution processing particularly attractive for the 2D platform. Techniques such as optical spectroscopy can probe samples containing billions of nanosheets to extract statistical information about the ensemble[51], liquid-dispersed nanosheets can be easily sorted by size and thickness,[52] and, in particular, liquid samples can be deposited using well-established techniques such as inkjet printing,[53] spin coating,[54] or spray coating.[55] The delamination of layered crystals in liquids can be broadly parsed into two classes; intercalation and exfoliation.

Layered crystals have been processed in liquids since 1859 when, in the reckless abandon of classical science, graphite oxide was first synthesised by intercalating graphite with heavily concentrated acids and then exfoliating with aggressive oxidisers.[56] A century later, Hummers and Offeman developed a less fatal method using potassium permanganate and sulphuric acid to add carboxyl (-COOH), hydroxyl (-OH), and epoxide (C-O-H) groups to the basal planes.[57] Such chemical modification polarises the crystal rendering it hydrophilic. This allows water molecules to be drawn between the layers to facilitate exfoliation upon ultrasonication and stability is then provided by the basal plane functionalisation. Using more modern and less hazardous methods, graphene oxide dispersions with high monolayer content can now be produced with lateral basal plane lengths of up to 50 μm.[58] While it is possible to remove the functional groups using wet chemical reduction to yield reduced graphene oxide, the basal plane contains many vacancies and defects which disrupt the lattice periodicity and such scattering centres are anathema to charge transport. There are a variety of post-processing efforts to recover pristine graphene but undoing crystallographic

defects and reseeding vacancies pose a significant challenge. This is a fundamental problem for device physics but the high degree of tunability bestowed by functionalisation has been embraced by chemists[59] and the number of papers published on graphene oxide is now rapidly increasing year on year.

A parent crystal can also be dilated by intercalating other molecules between the layers and the class of intercalation compounds is now well reported.[60] The interlayer widening is a function of intercalant diameter where a wider spacing imparts a lower net cost of exfoliation. The use of intercalants such n-butyllithium can also transfer charge to the layer which further reduces the interlayer binding energy.[61] The dilated crystal can then be exfoliated by ultrasonication or thermal shock and discrete nanosheets are stabilised against reaggregation by surfactants or the transferred charge from the intercalants. As one can imagine, charge transfer to the nanosheets renders their properties distinct from their pristine counterparts and, in general, the nanosheets tend to be negatively charged.[15] This drives a reaction with water, leading again to basal plane functionalisation in the case of graphene but TMDs are not reported to react in a similar manner. Instead, negatively-charged Group VI TMDs now have their *d*-states filled causing a semiconducting-to-metallic transition.[15] This places a substantial constraint on this technique but, as with graphene oxide, much work continues on restoring the properties of pristine nanosheets despite limited success. It is these limitations that created a space for a scalable, non-covalent, liquid exfoliation method that yields pristine nanosheets.

2.2.2 Liquid-Phase Exfoliation

In a testament to the speed of progress, it was just four years after the mechanical exfoliation of graphene that liquid-phase exfoliation (LPE) was developed for exfoliating layered crystals.[62] LPE is a simple method for overcoming the interlayer forces using ultrasonic or shear energy in a stabilising environment. The process proceeds as shown in Figure 2.6 where a bulk powder (Figure 2.6A) is sonicated and the resultant dispersion is stabilised using solvent-particulate interactions or a stabiliser such as surfactant (Figure 2.6B). In the case of a solvent with a surface energy dissimilar to the material, reaggregation will occur (Figure 2.6C). Scalability is achieved through shear force mixing, a similar exfoliation mechanism, where industrial-scale quantities of 2D materials can be generated.[63]

LPE builds on decades of chemical exfoliation research but, crucially, mono- and few-layer nanosheets are created rather than simply nanoscale particles with bulk properties. These nanosheets are typically defect-free and do not have molecules covalently linked to the basal plane which makes this process especially attractive for electronic applications.[62,63,64] The technique itself is also extremely versatile; it appears the entire family of layered crystals is exfoliable using LPE (Figure 2.6D) and a layered material has yet to be found that cannot be exfoliated in this manner.[31] Furthermore, 2D dispersions can be easily processed into inks,[65] pastes,[66] or multicomponent composites.[12] Post-sonication, the dispersions are highly polydisperse with an extremely broad distribution of lateral sheet size and thickness. This could be a fundamental issue as the bandgap is strongly layer-dependent but centrifugal processing allows sorting by mass and therefore nanosheet dimensions.

The stability of the dispersion derives from careful choice of the solvent environment that the bulk crystal is exfoliated in; solvents with surface energies close to that of the crystal

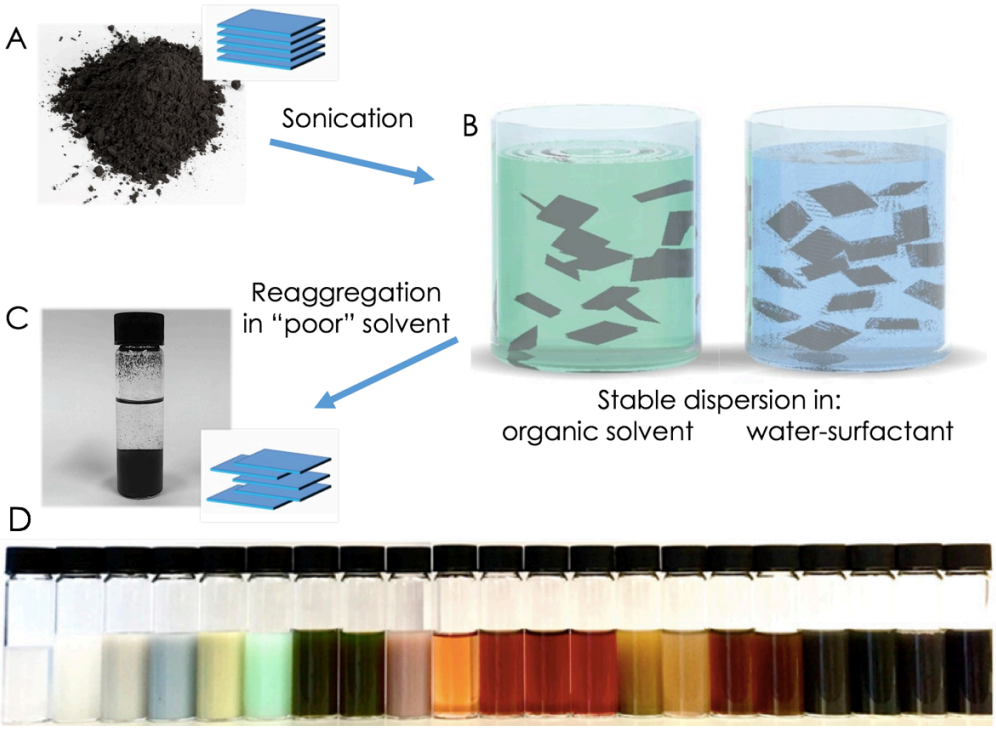

Figure 2.6: Liquid-phase exfoliation. A) An as-bought bulk powder. B) A dispersion stabilised though solvent or surfactant interactions. Image from Ref. (66). C) A poorly stabilised dispersion, resulting in considerable reaggregation. D) Various dispersed materials. Image from Ref. (67).

minimise the energetic difference between exfoliated and unexfoliated material which slows reaggregation.[67] The dispersion can also be stabilised through addition of surfactants or polymers to the bulk powder prior to sonication. The use of such stabilisers allows exfoliation to proceed in non-toxic solvents such as water which are clearly preferable to solvents with a ten-page MSDS. Common ionic surfactants, such as sodium dodecylbenzenesulfonate or sodium cholate, work by non-covalently adsorbing onto the nanosheet surface and electrostatically repelling other dispersed nanosheets thus preventing reaggregation. This allows high concentration dispersions to be stable for potentially hundreds of years as the nanosheets are prevented from interacting with each other.[68]

Polymer stabilisation works in a similar manner where the polymer chain non-covalently adsorbs onto the nanosheet surface but rather than electrically repelling other nanosheets, reaggregation is prevented by steric repulsion. This process is very well understood and the modelling has shown good success in predicting stable combinations of nanosheets, polymers, and solvents.[69] The obvious drawback to using surfactants or polymers is their removal. The non-covalent adsorption means these additives can be removed without compromising the nanosheet crystallinity but the removal methods themselves tend to be incomplete and deleterious. A film composed of a nanosheet-polymer composite may show good mechanical properties but the polymer chains strongly affect the electrical characteristics necessitating their removal. For example, polymers from the cellulose family can be removed by annealing at temperatures > 300 °C[70] although this restricts the type of substrate one can use and processing above ~ 50 °C has been shown to degrade monolayer photoluminescence.* Similarly, films containing surfactant need to be washed causing material loss and it is unclear how much may reside in the film's free volume. For the electronic applications contained within this work, we thus chose to stabilise our dispersions using solvent interactions with the goal of minimising nanosheet contamination.

Dispersion by Ultrasonication

Ultrasonic cleaning was first commercialised in the 1950s but the underlying mechanisms were initially not understood. It was over a decade later that ultrasonication received wide interest in the biological community when early SONAR technology was developed for

*Unpublished at time of writing

submarine warfare. Researchers noticed that testing was killing local marine life and, shortly after, biologists began to concentrate their efforts on understanding the effect of acoustic waves on microscale systems.[71] Nowadays, ultrasonication is a particularly useful method for exfoliating layered crystals as the necessary equipment is common to most labs. It can be achieved using a sonic bath or ultrasonic probe and, during operation, requires little attention.

Ultrasonication is the generation of high intensity acoustic waves from a mechanical source with wave propagation proceeding through a range of phenomena such as cavitation, radiation pressure, and acoustic streaming.[72] Exfoliation driven by ultrasound can be primarily attributed to the implosion of cavitation bubbles producing high tensile and shear stresses along with liquid jets which cause both exfoliation and fragmentation of the crystal.[68] Bath sonication involves low intensity ultrasonic waves which set up standing waves in a small tank. This means there are regions of constructive and destructive interference throughout the tank and, along with damping caused by the sample container, means reproducibility is poor. Probe (or tip) sonication is a much higher intensity process where a region of intense ultrasonication is established directly under the probe. The ultrasonic intensity is a strong function of probe distance[73] which makes reproducibility challenging but, as nanosheets can be characterised in aggregate, individual variation can be statistically subsumed.

Ultrasonication is a mechanically aggressive technique but does not appear to cause basal plane damage as reporting indicates that the exfoliated nanosheets are quite pristine.[63,64,74] During early work on graphene, a D-band appeared in the Raman spectra but its intensity relative to truly defective graphene-like materials fostered speculation that this was caused by

the nanosheet edges.[64] This was confirmed by demonstrating that the ratio of Raman D- to G-bands scaled with the nanosheet edge-to-area ratio.[75] There has been much further Raman analysis performed on LPE nanosheets and, while damage may occur for longer sonication times, the crystals appear defect free.[53,76,77] However, Backes *et al.*[68] note "one complication is that, as the structural quality of the product will depend on the actual quality of the starting crystal, some researchers observe basal plane defects while others do not."

Solvent Stabilisation

It is not enough to merely overcome the van der Waals interaction to successfully exfoliate a crystal as the nanosheets will reaggregate unless stably dispersed. An effective solvent will not only stabilise the exfoliated nanosheets but will also reduce the net energy required to exfoliate the crystal.[78] This was first demonstrated for CNTs in 2008 by Bergin *et al.* where their early modelling showed that a successful solvent is one with a surface energy close to that of the nanotubes and this was experimentally confirmed for N-methyl-2-pyrrolidone (NMP) and dimethylformanide (DMF).[79] These data suggested that graphite, and indeed graphene, may be stable in such solvents as its surface energy is close to that of CNTs and this was conclusively shown to be the case for NMP later in 2008.[62] A more expansive solvent study found that those with surface energies close to 70 mJ m^{-2} produced relatively high concentrations of dispersed material, shown in Figure 2.7, but tended to be have high boiling points concurrent with high toxicity.[80] Here we can also see that common non-toxic solvents such as water and isopropanol were found to lie outside the range although IPA still showed some dispersibility indicating the understanding was incomplete.

The use of surface energy as an umbrella descriptor works well for initially approximating

a useful solvent but some were found to be weakly dispersive despite a closely matched surface energy.[80] This was interpreted through deeper modelling with the Hildebrand and Hansen solubility parameters from solubility theory. In solvent-solute systems, intermolecular interactions can be divided into dispersive (D), polar (P), and hydrogen-bonding (H) components. The Hildebrand parameter, δ_T, is the commonly used form of the cohesive energy density, $E_{C,T}/V$, where $E_{C,T}$ is the total molar cohesive energy and V is the molar volume of the solvent. It is this cohesive energy density that can be divided into the D, P, and H components:

$$\frac{E_{C,T}}{V} = \frac{E_{C,D}}{V} + \frac{E_{C,P}}{V} + \frac{E_{C,H}}{V} \tag{2.1}$$

The square root of each of these components is called a Hansen solubility parameter δ_i (i = D, P, or H):

$$\delta_T^2 = \delta_D^2 + \delta_P^2 + \delta_H^2 \tag{2.2}$$

For non-polar solutes, it is sufficient for the Hildebrand parameter of the solvent and solute to be closely matched to identify an effective solvent but all three Hansen parameters must be closely matched if the solute is polar. This parameterisation has been very successful in predicting stable dispersions, although Hernandez *et al.*[62] note it is surprising "that good solvents have nonzero values of δ_P^2 and δ_H^2 at all. The non-polar nature of graphene would suggest that the Hildebrand parameter or the dispersive Hansen parameter alone would determine dispersibility."

A contributory factor here may be the long known, but recently characterised,

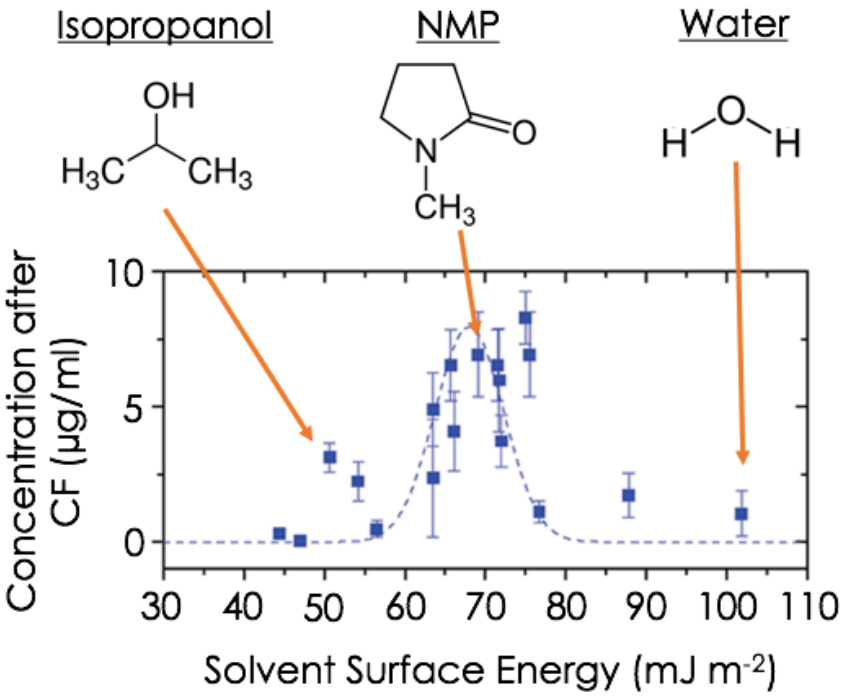

Figure 2.7: Dispersibility curve. A variety of solvents and their efficacy at exfoliating graphene. 3 common solvents are highlighted. Image adapted from Ref. (80).

sonochemical degradation of NMP.[81] NMP has been shown to create polymer by-products during sonication which may be desirable for a stable dispersion but indicates that solvent stabilisation may be complemented by adsorbed polymer.[81,82] There is also evidence that NMP is a difficult molecule to remove as residual traces remain *in situ* after annealing at 400 °C—well above the 202 °C boiling point.[62] Further, when an NMP-exfoliated material is redispersed in another solvent with mismatched surface energy (such as IPA), it shows remarkably higher stability than if the material was exfoliated in that solvent alone.[83] This could imply that the success of NMP as a prototypical solvent can be partially attributed to non-covalent adhesion of its polymerised by-products, although this effect is merely complimentary as evidenced by stable dispersions created through shear force mixing.[63]

The use of solvent interactions over surfactants to stabilise the nanomaterials also grants advantages further down the processing line. After an ink has been deposited, residual solvent should be minimised so the properties of the material itself can be probed without contamination. This is achievable using low boiling point solvents which evaporate quickly but residual surfactant or polymer are much more difficult, if not impossible, to completely remove. Volatile solvents are highly desirable for formulating inks but are fundamentally limited by their (generally) poor exfoliability.[80] This can be overcome by solvent exchange where exfoliation is performed in a well-matched solvent and the exfoliated material is then transferred to a different solvent for further processing.

Size Selection

Top-down exfoliation methods delaminate layers from the bulk crystal but the bulk powders are not neatly ordered as previously shown in Figure 2.2C. While the individual monolayers that constitute a layered crystal will have a broad distribution of lengths, sonication can also fragment the nanosheets across the basal plane adding to the polydispersity.[68] Sonication also does not yield complete exfoliation of the crystal so the nanosheets will also have a broad range of thicknesses. The issue of polydispersity has consequences across applications; it is not ideal for electronics as the bandgap scales with layer number, and large nanosheets are desirable for mechanical applications whereas small nanosheets are much more efficient for catalysis.[52] Addressing this was the first major challenge for LPE and the most successful strategies sort the nanosheets through centrifugation.

There are two techniques in popular use where nanomaterials can be sorted by density or sedimentation rate. Density gradient ultracentrifugation uses a medium of graded density

(DGM) wherein the nanomaterial moves along the centrifuge tube until it reaches the point where its buoyant density matches that of the surrounding medium. The greatest success here has been in sorting CNTs owing to density differences across nanotubes with different diameters but the technique has also been used to sort nanosheets by thickness.[52,84] DGU is generally limited by procedural complexity and low yields but monolayers and bulk layered crystals also have the same density which makes their separation quite challenging. Furthermore, residual DGM is undesirable for further processing and for applications that require pristinity.

Sedimentation-based separation (SBS) isolates dispersed materials by catalysing their sedimentation rate through a centrifugal force. The rate is described by the Svedberg equation

$$s = \frac{m(1 - \varrho V)}{f} \tag{2.3}$$

where s is the sedimentation coefficient, m is the mass, ϱ is the solvent density, V is the volume a gram of material occupies in the solvent, and f is the frictional coefficient. The sedimentation is thus dependent on the mass of the nanosheet and the drag force that it generates. Under centrifugation, large and thick nanosheets sediment fastest owing to a high mass leaving small and thin nanosheets retained in the dispersion. This process has since been refined to increase the efficiency and efficacy of the yields borrowing inspiration from gas-separation centrifugation cascades.

Liquid cascade centrifugation (LCC) was developed to sort nanosheets sizes from a polydispersion and to also controllably enrich the monolayer content.[52] The cascade proceeds as shown in Figure 2.8. A polydispersion of sonicated nanosheets is centrifuged at

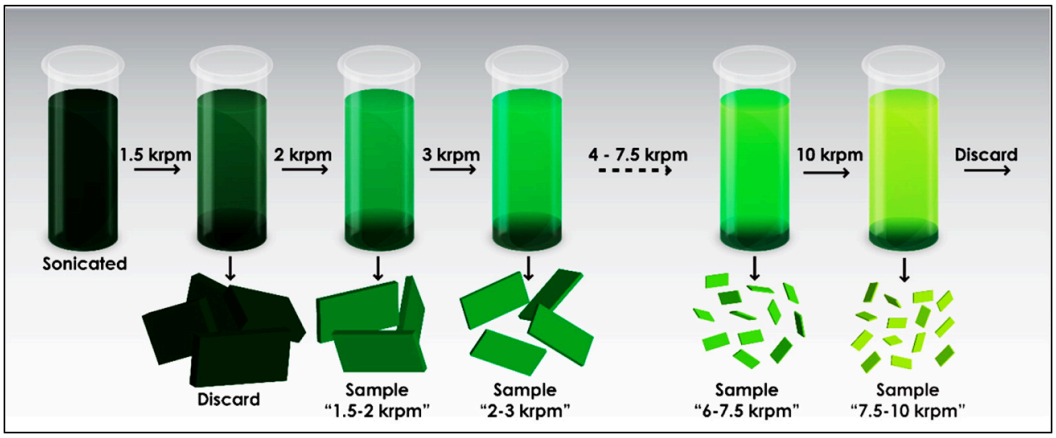

Figure 2.8: Liquid cascade centrifugation. The sediment discarded after the first centrifugation contains large unexfoliated particles while the supernatant discarded after the last centrifugation step contains extremely small nanosheets. Image from Ref. (52).

a low speed, 1.5 krpm, to sediment the large unexfoliated particles which can be either discarded or retained for future resonication. The supernatant now contains nanosheets with a broad distribution of lengths and thicknesses, including monolayers. This supernatant is then centrifuged at a higher speed, 2 krpm, and the sediment is collected. This sediment, sample "1.5–2 krpm" in Figure 2.8, will contain large, thick nanosheets that, crucially, can be redispersed by mild sonication in any desired solvent at a desired concentration. The supernatant produced after centrifuging at 2 krpm can again be centrifuged at a higher speed, 3 krpm, to isolate a sediment containing slightly smaller nanosheets. The supernatant from the 3 krpm step can again be centrifuged continuing the cascade for a many steps as are desired with each step iterating the centrifugation speed upwards. After each step, the sediment contains progressively smaller nanosheets and the supernatant becomes more monolayer enriched. Since the material is collected after each iteration, this results in low wastage and relatively high masses of nanosheets of a given aspect ratio. Importantly, if a specific size is desired, then one can simply trap the desired

nanosheets between two fixed rpm. As TMD bandgaps are strongly layer dependent, this is particularly useful for creating dispersions with a tight distribution of bandgap.

This is a powerful technique whose strength lies in its accessibility and simplicity but challenges remain. The primary disadvantage of LCC lies in generating monolayer-enriched dispersions as the monolayers tend to be very small (L < 50 nm) and, depending on the trapping speeds used, the dimensional distribution of a given sample can be quite broad. Further, it is not currently possible to generate large area monolayers using the combination of LPE and LCC but serious efforts continue to be directed at addressing these issues.

I never trust anyone who's more interested in success than doing the thing they want to be successful at.

Randall Monroe

3

Deposition and Applications

The practice of ink deposition is at least as old as behaviourally modern humans. Prehistoric cave art was created using pigment-based inks composed of ochre, charcoal, and ground bone with animal fat used as a binder to adhere the ink to a surface.[85] While most human cultures developed ink and writing, the foundation of modern printing technology began in 1436 with the invention of the printing press. Despite

the upheaval this caused, technical progress was incremental until the invention of the transistor and the beginning of the Age of Silicon when digital technology vastly improved the throughput, accuracy, and resolution of deposition. With the invention of the thermoplastic 3D printer during the 1980s, printing bifurcated into graphical and functional deposition and the myriad ways to print functional materials now fall under the umbrella of *additive manufacturing*. This field has been incredibly attractive to industry for its promise of rapid prototyping, broad freedom of design, and the near-zero material wastage.

The past fifteen years in particular have seen the emergence of the subfield of printed electronics (PE) as the printer costs came down and the resolution went up. The field was pioneered using conductive organic polymers which are routinely used in commercial OLED televisions where their performance now rivals that of amorphous silicon. The solution processability of layered crystals combined with their distinct electrical characteristics means the carrier-transport limitations that organics appear to be reaching could be surpassed with these new materials. As groups master exfoliation, the research has pivoted towards digital fabrication and publications regularly feature printed photodetectors, capacitors, transistors, and chemical sensors on many different substrates.[86] With this in mind, this chapter will summarise the fundamentals of the relevant printing techniques, the characteristics of printed films, the relevant printed devices, and end with a review of the literature on printed devices.

3.1 Printing Technologies

A key objective of 2D ink investigations has been to create printed networks with reasonable performance at low cost and low complexity. Many techniques exist for depositing inks in a relatively cheap manner such as inkjet, gravure, and flexographic printing, each with their own resolution and throughput. The choice of deposition therefore depends on the desired outcome; inkjet printing can create high resolution features at low manufacturing speeds whereas flexographic printing has much higher throughput albeit with increased feature size. The various deposition methods also require bespoke inks as rheology plays a central role in consistent deposition, ink stability, and film uniformity.[68] Low viscosity and low concentration inks are required for inkjet printing and spray coating, and are easily generated using LPE techniques. This, combined with the ready availability of R&D inkjet printers or the simplicity of the airbrush, has meant that inkjet and spray coating have been particularly relevant for lab-scale prototyping of printed devices composed of 2D networks.

3.1.1 Inkjet Printing

The first inkjet printer used a continuous inkjet process where the ink is deposited constantly until the stream of droplets is electrostatically deflected into a waste reservoir.[87] This is especially well suited for devices like chart recorders, the first consumer tool in the 1950s, but it was another two decades before the much more accurate drop-on-demand (DoD) printing was developed. DoD printing can be subcategorised into thermal inkjet printing and piezoelectric inkjet printing and both have been industrially attractive as the process is digital, there is near-unity material use, it is non-contact, highly scalable, and a wide range of materials and solvents can be printed.

The late 1960s saw a wealth of patents on a wide variety of printing technologies under the inkjet umbrella but each was a commercial failure due to a high level of complexity coupled with unreliable performance.[87] The need for fast, low-cost printing evolved alongside the development of office computing and culminated in the 1970s with the concurrent invention of the thermal inkjet process by teams at Canon and HP.[88] Figure 3.1A shows how droplet formation proceeds in thermal DoD. The chamber inside the printhead contains a thin-film resistor in good contact with the ink which fills the chamber. The resistor heats at an extremely rapid rate ($\sim 600\ \mathrm{K}\ \mu\mathrm{s}^{-1}$) which causes superheating and vaporisation of the thin layer of ink in contact with the resistor.[89] This creates a rapidly expanding vapour bubble which produces the fluid displacement necessary to eject a droplet from the nozzle. The use of a vapour bubble is where Canon's trademark Bubble Jet originates, for those of us old enough to remember. Once the droplet has been ejected from the nozzle, the resistor is deactivated and the bubble collapses. The drop in pressure draws fresh ink in from the reservoir to fill the chamber and once the acoustic waves generated by the ink flow have subsided, the cycle is ready to begin again.

The thermal DoD process has become ubiquitous across modern consumer printers as the resistive element can be produced using common fabrication methods such as photolithography.[90] To further simplify high volume manufacturing, the printhead is contained with the ink cartridge and separate to the printer body itself. This is important as when the printhead becomes clogged, only the cartridge needs to be replaced rather than the entire tool. This has, perhaps cynically, allowed the printer body to be sold at a loss and is the reason printer ink is one of the most expensive fluids in the world. The heating and vaporisation process presents an inherent limitation to this technique; the ink itself needs to

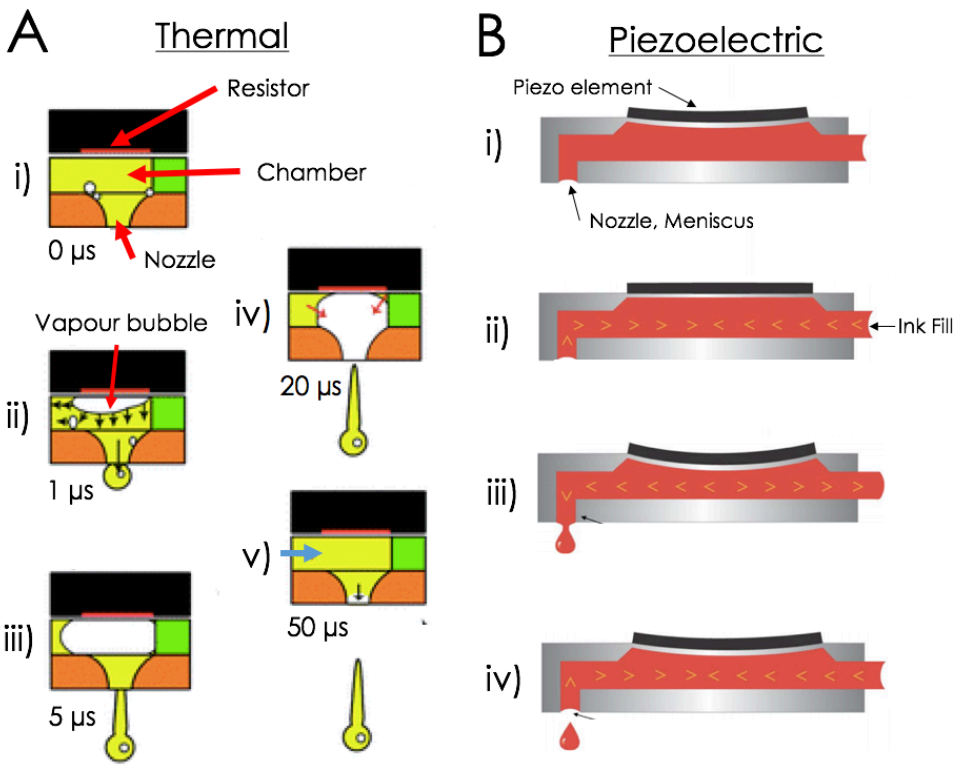

Figure 3.1: Inkjet printhead schematics. A) Thermal droplet formation. The system is at equilibrium at 0 s (i). The resistor is then rapidly heated which vaporises the ink creating a bubble (ii). This bubble quickly expands forcing a droplet out of the nozzle (iii) and (iv). The bubble then collapses and ink fills the chamber from the reservoir (v). B) Piezoelectric droplet formation. The PZT is at equilibrium at 0 s (i). A voltage is placed across the PZT crystal which draws more ink from the reservoir (ii). An opposite voltage then drives the PZT in the opposite direction extruding a droplet from the nozzle (iii). The PZT returns to equilibrium and the chamber refills. Adapted from Ref (84).

be robust against degradation during vaporisation which limits the types of solvent and particle which can be used.[89] This has meant that piezoelectric DoD has been favoured for digital fabrication over thermal DoD.

The first patent on a piezoelectric printhead in the 1970s fully anticipated the coming design space as it discusses the need for the electrode to be resilient against corrosion across different solvents.[91] This is key to the practicality of piezoelectric DoD because the thermal design necessitated parallel development of the ink as the vaporisation process is not

equivalent across the variety of surface energies and viscosities of different solvents. As the name suggests, the droplet formation in piezoelectric DoD is driven by a piezoelectric element. This element is usually lead zirconate titanate (PZT), a ceramic perovskite, and during its manufacture is exposed to heat and a strong electric field which aligns the electric dipoles within the material. The dipole alignment is then fixed by removing the heat source and this anisotropic dipole alignment means that mechanical deformation of the crystal will create a difference in surface charge density between the crystal faces. This manifests as a change in the electric field between the faces but, importantly, the converse of this can also be achieved where the application of an electric field can generate a mechanical deformation.[87] This is the cornerstone of piezoelectric DoD deposition as the droplets are generated by driving physical changes in the geometry of the chamber leaving the ink unadulterated. A schematic of piezoelectric printhead operation is shown in Figure 3.1B. Subfigure B(i) shows the printhead at equilibrium with a filled chamber and an unbiased PZT crystal in a neutral position. An electric field is applied to the PZT, B(ii), and the crystal contracts which draws more ink in from the reservoir to further fill the chamber. An opposite bias is then applied, B(iii), and the PZT expands into the chamber forcing the ink out of the nozzle but also back into the reservoir. The backflow into the reservoir is attenuated through acoustic baffles—a series of pillars—to break up the waves generated by the motion of the ink. As the PZT returns to a neutral position, B(iv), the ink refills the chamber from the reservoir. The bias across the PZT is strongly correlated to the energy needed to form and break off a droplet of ink at the nozzle and varies across solvents. This means the signal waveform that drives the PZT oscillation is a central variable in piezoelectric printing.

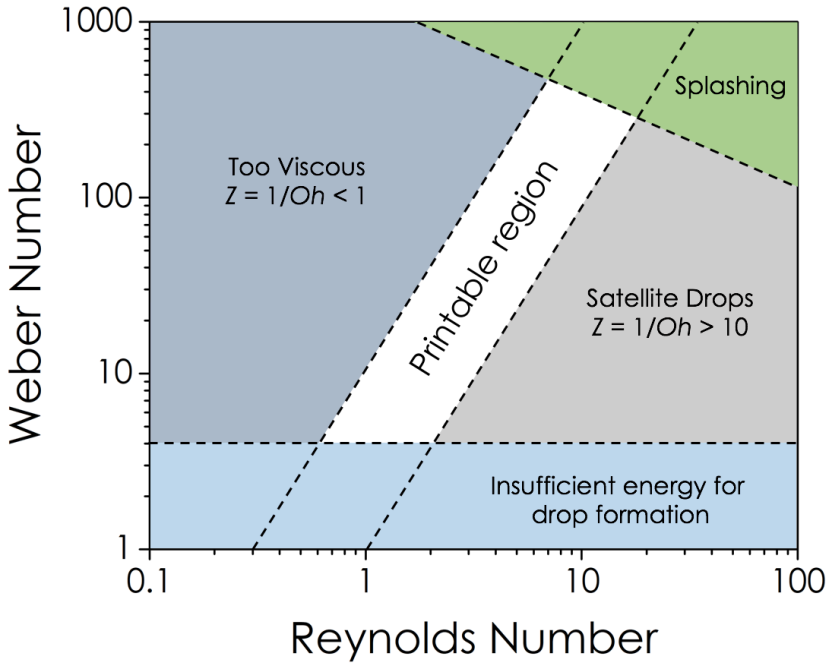

Figure 3.2: Range of printable fluid. The parameter space defined by the Reynolds and Weber numbers. This illustrates the narrow window that reliable printing occurs within. Image adapted from Ref. (92).

The quality of an inkjet printed film is determined by a wide variety of factors specific to the ink and the method of deposition. Surface tension, viscosity, and inertia determine the printability of an ink and are characterised by the dimensionless Reynolds and Weber numbers. The Reynolds number is the ratio of inertial to viscous forces

$$Re = \frac{\varrho a v}{\eta} \tag{3.1}$$

where ϱ is the density, a is the droplet diameter, v is the droplet velocity, and η is the

viscosity. The Weber number describes the ratio of inertia to surface tension

$$We = \frac{\varrho a v^2}{\gamma} \tag{3.2}$$

where γ is the surface tension. To remove the velocity dependence, Eq. 3.1 and Eq. 3.2 are combined into the inverse Ohnesorge number (Oh)

$$Z = (Oh)^{-1} = \frac{\sqrt{\gamma \varrho a}}{\eta} \tag{3.3}$$

This number is used to gauge the printability of a liquid; if Z is too low, $< \sim 4$, then the viscous forces will prevent the separation of a droplet at the nozzle and if Z is too high, $> \sim 14$, a large number of satellite droplets can form behind the droplet.[92] This defines the parameter space shown in Figure 3.2. Further boundaries affecting droplet formation are denoted by the top and bottom regions; the ink at the nozzle must contain enough kinetic energy to snap off a droplet but not so much kinetic energy that the droplet splashes upon contact with the substrate.[87] Many solvents cannot be printed directly and thus require additives to alter the rheology. Polymers such as acrylics, cellulose, or rubber resins are often used to modify the viscosity and bind the particles together whereas surfactants and defoamers can be added to improve wetting properties, lower the surface tension, and reduce bubbling.[93]

The quality of a printed feature is largely determined by the application. Large scale graphical printing can easily accommodate a nozzle misfire or misalignment but such artefacts are anathema to printed devices. During the course of printing, a nozzle can become clogged through accumulation of particles in the printhead but this can be mitigated by using the rule of thumb where the average particle size should be no more than

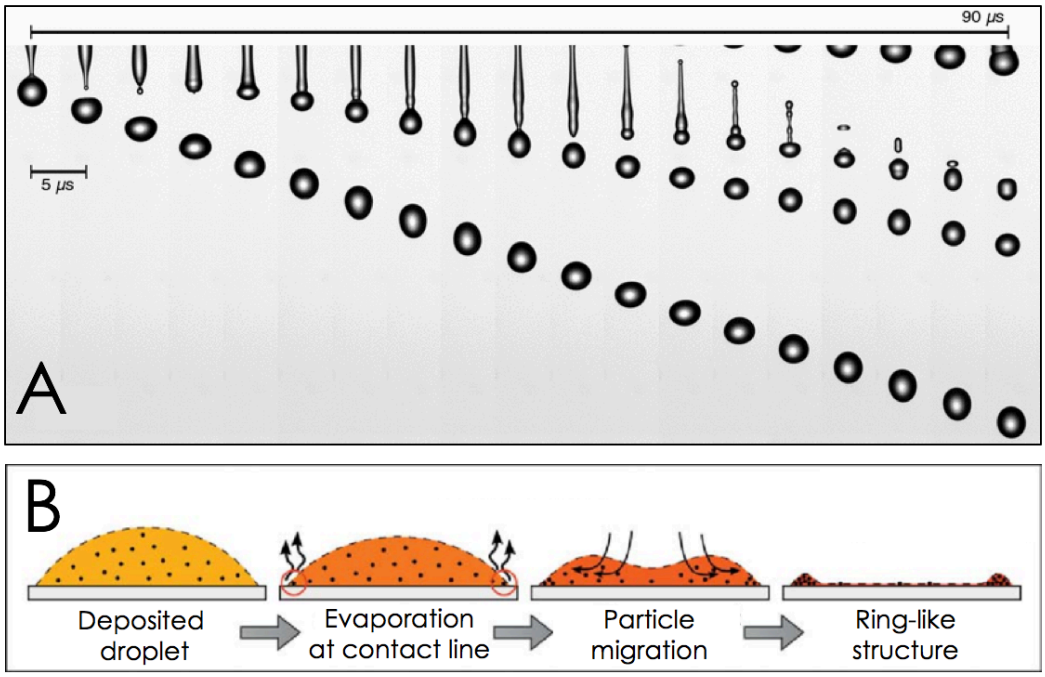

Figure 3.3: Inkjet printing artefacts. A) For single droplet formation, the pressure waves created by the piezoelectric actuator must extrude the ink with enough force to snap off a droplet and the surface tension and viscosity must be balanced so the liquid column then joins the main droplet. If the boundaries determined by Z are not met, satellite droplets can form as seen behind the primary droplet. B) The evaporation of solvent draws the suspended particles to the contact line leaving a ring-like structure once the solvent has fully evaporated. Image from Ref. (98).

$1/50^{th}$ of the nozzle diameter.[53] The viscosity of the ink is also strongly dependent on the particle volume fraction and aspect ratio so these should be tailored to the specific printhead.[68] However, a primary issue during functional printing is the formation of satellite droplets. These are smaller additional droplets produced as the main droplet extrudes from the nozzle as shown in Figure 3.3A.[87] Each pressure pulse will drive a jet of ink with a droplet at its head followed by a columnar tail. Inertia will then act to snap off the primary droplet and, through surface tension, the tail then merges with the head. Should the rheology of the ink lie outside the Z boundaries however, the tail can collapse chaotically rather than consolidating with the head and additional droplets will then follow

the primary droplet. Satellite drops pose a problem for high resolution deposition as they can lead to poor definition along the trailing edge of a printed feature. This can cause crosstalk between conductive components and even result in internal shorting.[94] These satellites can also get caught in airflows and contaminate the prints and the equipment but, again, this can be mitigated through optimisation of the rheology and the driving waveform of the PZT crystal.

A further source of consternation during solution deposition is the coffee-ring, or coffee-stain, effect shown in Figure 3.3B.[95] When the solvent in a particle-laden droplet is evaporating, it tends to evaporate faster at the edge—or contact line—due to a higher surface-to-volume ratio.[87] The position of the contact line is mediated by the interplay between solvent and substrate surface energies, and is discussed further in the next section. As the solvent loss at the contact line is replenished by solvent from the drop centre, the outward radial flow is strong enough to overcome the gravitational force that acts on the dispersed particles. The transported particles thus accumulate at the droplet edge leaving a hollow ring instead of a uniform spot once the solvent has fully evaporated. This is detrimental to the deposition of uniform features but there are several strategies to create counter flows within the droplet. The recirculatory flow within a drop is known as the Marangoni effect and is driven by a surface tension gradient as a high surface tension will cause a fluid to flow away from regions of low surface tension. A surface tension gradient can be thermally induced,[96] concentration induced,[87] induced through binary solvent mixtures[97] or with a surfactant,[48] and each have been used to deposit uniform droplets. The choice of strategy again depends on the final film; if surfactants are deleterious to the performance of the device, then a binary solvent may be a more appropriate. An alternative

strategy for overcoming this effect is through the use of a porous substrate.[98,99] This can counteract the coffee-stain effect as the rate of substrate penetration tends to be much faster than both the evaporation rate and the particle transport (milliseconds *vs* seconds).[100] This suppresses the particle migration but is strongly dependent on the pore size; a larger pore size means the droplet spreads less and penetrates deeper.[100] Such substrates are of particular benefit for single-solvent inks that have surface energies that are heavily mismatched with common substrates such as SiO_2.

3.1.2 Spray Coating

The various rheological constraints of inkjet printing can be avoided if an aerosol-based deposition method can be used. Spray coating is a simple, cost effective, and scalable method for depositing inks if fine resolution is not required. This method is at least 150 years old when the airbrush was initially developed to coat photographic plates but was later adapted by an art school to cultivate the airbrush technique.[101] The maturity of airbrushing over the last century has made the technique attractive for printed electronics as large area, highly uniform films are easy to deposit and much fundamental work has been done in creating transparent, conductive CNT networks.[102,103] The technique itself also has a surprisingly rich parameter space allowing tunability over variables such as scan speed, flow rate, stand-off distance, backpressure, nozzle diameter, and substrate temperature to suit material and solvent demands.[104]

An example schematic of an airbrush during deposition is shown in Figure 3.4A. There are two types of airbrush defined by the action of the trigger; single-action airbrushes where the trigger only actuates the nitrogen flow, and dual action where both the nitrogen and the

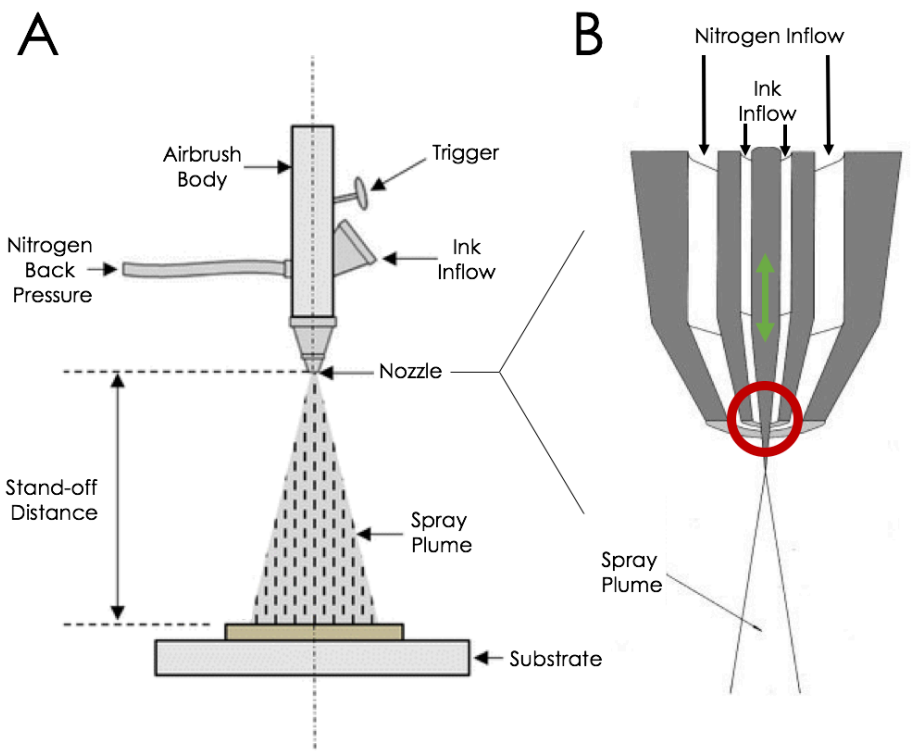

Figure 3.4: Spray coating schematics. A) A schematic showing the airbrush during deposition. This shows the rich parameter space the tool operates in. Image adapted from Ref. (105). B) Magnification of the nozzle. The needle retraction is actuated by the trigger (green arrow) allowing ink to mix with the nitrogen gas (red circle) to form the aerosol.

ink flows are trigger actuated. The latter gives much greater control over deposition and is thus better suited for lab-based prototyping.[101] Figure 3.4B shows a close-up of the nozzle with the aperture shown ringed in red and the needle motion shown in green. As the needle retracts from the nozzle, the ink mixes with the nitrogen to form the aerosol. The spray plume itself is strongly dependent on the type of nozzle and a wide variety of nozzles are available. Common nozzles are the full cone and hollow cone where, intuitively, the spray plume is either a solid or hollow cone of mist and are chosen according to the desired end film.[101] The substrate temperature is also extremely important in influencing the droplet drying rate once

the droplets reach the substrate.[104] An elevated temperature will cause the droplets to dry rather than coalescing into larger droplets which leads to films with low uniformity.

Of the fundamental variables such as backpressure, stand-off distance, and flow rate, backpressure was demonstrated to be the most important consideration for uniform and reproducible films.[104,105] The actuation of the trigger causes the high velocity nitrogen to atomise the paint into droplets, meaning droplet size is strongly correlated to the pressure of the nitrogen. A low backpressure, ~ 15 psi, will generate large droplets compared to the much smaller droplets generated at high backpressures, ~ 40 psi. This correlation is important for reducing non-uniformities; a reduced droplet size minimises the coffee stain effect as the solvent evaporates quicker from a smaller drop mass. This was demonstrated by Shen *et al.*[106] with water-based inks and by Scardaci *et al.*[104] with an isopropanol-based ink where they note that a low boiling point solvent is preferred to further maximise the evaporation rate.

The versatility across solvents is one of the key selling points of the spray coating technique. Inks must be heavily tailored in viscosity and surface energy to be inkjet printable but since spray coating atomises the ink, the formulation of any single droplet is much less important than the formation of the mist ensemble. This means that inks using isopropanol,[104] NMP,[74] and THF[73] can be sprayed without additives. This is extremely useful for creating electrical networks as the amount of additives incorporated into the ink typically have a deleterious effect on carrier transport, and should be therefore be minimised. The additives can be eliminated altogether if solvent interactions are used to stabilise a 2D crystal-based ink making it especially attractive for nanosheet electronics.

3.2 The Nature of Printed Networks

One of the first printed 2D applications was demonstrated in 2012 when Torrisi *et al.* inkjet printed a field-effect transistor with LPE graphene.[53] In the intervening years, the field of printed 2D devices has rapidly grown and expanded to include a wide variety of deposition techniques. As each technique requires a bespoke ink and has a distinct deposition, the morphology of a printed film will vary with the deposition method. This is important as characteristics such as surface roughness can strongly influence the performance of vertical heterostructures.[9] There is a lack of comparative studies in the literature on the variation across morphologies which is likely due to the youth of the field; the figures of merit are unestablished and the daunting task of investigating the many permutations of various binders, additives, pigments, and solvents has yet to be undertaken. However, some general comments about the films can be made.

A printed film composed of a 2D material will contain a certain amount of free volume, or porosity, regardless of deposition method. This is due to the irregular shape of the nanosheets and the current inability to generate a fully monodisperse ink. While no information is available quantifying the variation of porosity across printing techniques, a qualitative statement can be made through SEM examination. Figures 3.5A and B show a film of BN deposited using an airbrush and an inkjet printer, respectively. It is clear that the spray coated film has a much higher surface roughness than the inkjet printed film which is due to the inkjet printer precisely depositing droplets whereas the airbrush blanket deposits the ink. The difference in nanosheet alignment in the two films will result in a difference in porosity so, depending on the application requirements, one deposition method may be

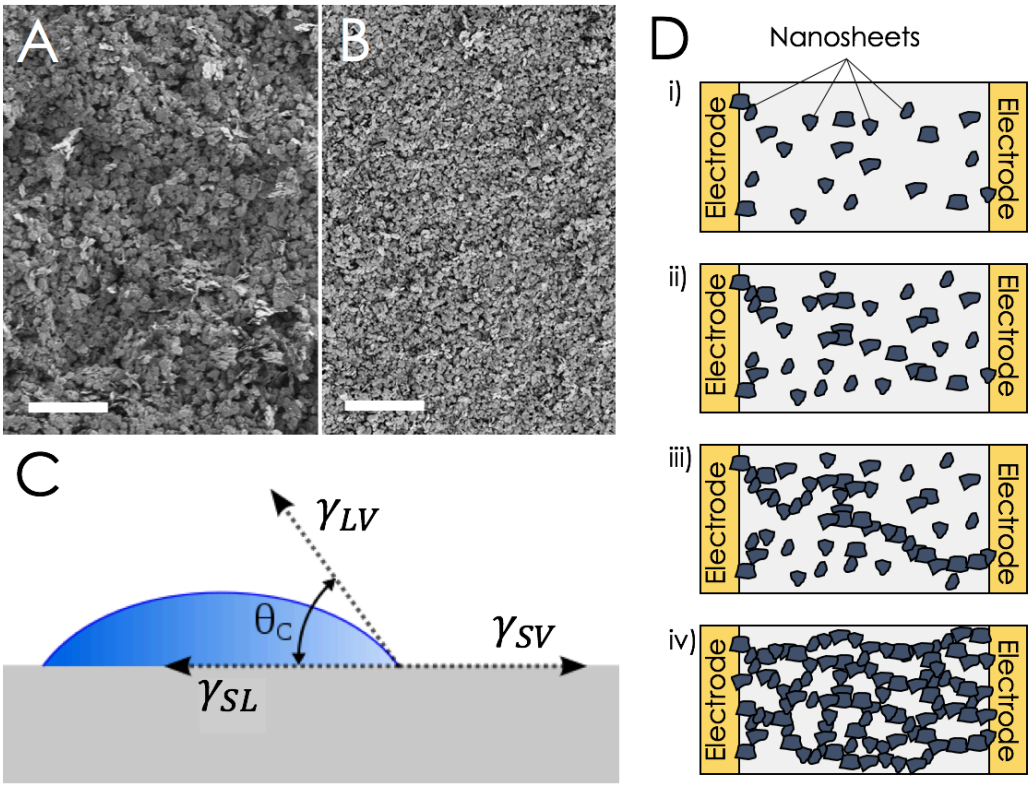

Figure 3.5: The nature of printed films. Topology of A) a spray coated BN film and B) and inkjet printed BN film. The morphology is noticeably rougher in the spray coated film. Both images are adapted from personal work and both scale bars are 5 µm. C) The relationship between the droplet surface energies when it is deposited on a substrate. Image adapted from Wikipedia. D) The percolation of a network through successive layers.

favoured over the other. The mobility of a network is also strongly coupled to the surface roughness of the layer beneath[107] which may rule out spray coating for certain elements of a device. There is also little known about the effects of nanosheet alignment on electrical or mechanical characteristics but inferring from what is known about CNT networks,[108] it is likely that a well-aligned film will have better carrier transport due to the larger interfacial overlap of the nanosheets.

While morphology may be poorly investigated, the role of the substrate is well understood.

Once a droplet is deposited on a substrate, the equilibrium shape is defined by the various interfacial energies contained in the Young equation

$$\cos\vartheta = \frac{\gamma_{SV} - \gamma_{SL}}{\gamma_{LV}} \tag{3.4}$$

where γ_{SV}, γ_{SL}, and γ_{LV} are the substrate-vapour, substrate-liquid, and liquid-vapour surface energies, and ϑ is the contact angle of the droplet with the substrate.[87] This is graphically represented in Figure 3.5C. The contact angle varies dramatically across solvents and substrates depending on the balance of cohesive and adhesive forces, known as wetting. For contact angles $0° < \vartheta < 90°$, wetting is favourable (high wettability) and the droplet will easily spread across the substrate, but for contact angles $90° < \vartheta < 180°$, wetting is unfavourable (low wettability) and the droplet will minimise its surface contact.[109] As the flexibility across substrates is a key strength of the non-contact printing methods, care must be taken to understand the variation of the droplet contact angles to ensure that sequential droplets coalesce into a solid line. During inkjet printing, a series of overlapping droplets will form a single body of liquid provided the droplets do not dry before the next is deposited.[87] The diameter of each droplet is fixed by the solvent-substrate interaction, known as contact-line pinning, and so limits the minimum width of a line of sequential droplets to the diameter of a single droplet. A solid rectangular line is thus deposited by adequately overlapping the droplets with typical centre-to-centre distances in the range of 0.5–0.8 of a droplet diameter.[87] The blanket deposition during spray coating means a film is formed by the coalescence of a multitude of small droplets but the homogeneity of the line is still mediated by the solvent-substrate interaction.

It is also important to note the change in network characteristics as the network is built

up through successive layers. Inkjet deposition requires dilute inks as high concentrations of nanosheets can cause nozzle blockages. This means that a single print of a pattern may not create a complete network. This is understood through percolation theory and has been used to comprehensively describe the evolution of electrical characteristics of CNT networks since the 1990s.[110,111,112] Figure 3.5D shows how a network can be built over successive prints. After a single pass, the network is discontinuous between the electrodes but as each pass deposits increasing amounts of material, a path is eventually formed through which current can flow. As more and more paths are created, the conductivity of the network will increase until it saturates at a bulk value. The scaling law has the form $Q \propto |t - t_c|^n$ where Q is the electrical property being investigated, n is the (often universal) exponent describing the system, t is the thickness of the network, and t_c thickness at which the first conductive path is formed, known as the percolation threshold.[113] The scaling law also applies to composites where a conductive component is increasingly added to a non-conductive component. In this case, the law has the form $Q \propto |\varphi - \varphi_c|^n$ where φ is the conductive filler volume fraction and φ_c is again the percolation threshold where the first conductive path is formed through the insulating matrix. The percolation threshold is central to percolation theory and the pre- and post-percolation regimes are of considerable interest. Below the percolation threshold, where $\varphi < \varphi_c$, particles are either discrete or aggregated in small islands with no continuous paths. However, above the threshold, where $\varphi > \varphi_c$, Q increases rapidly with additional conductive material.[114] In context of printed electronics, it is critical to establish the percolation threshold for a printed network to ensure that the device is operating in the bulk-regime, thus resulting in device characteristics that are much more easily reproduced.

3.3 Electronic Devices

In the wake of the discovery of graphene, the majority of electronic devices were built from mono- to few-layer nanosheets to showcase the new properties. Comprehensive studies with devices composed of nanosheet networks have only recently become more prevalent as the deposition experience accumulates. Simple, planar devices like photodetectors were ubiquitous but as the number of exfoliable materials grows, the assortment of properties are finding use in printed sensors,[115] electrodes,[116] lasers,[117] batteries,[118] supercapacitors,[119] and thermoelectrics.[120] The following are the device types relevant to this work.

3.3.1 Capacitors

A basic component of any circuit is the capacitor. The device design is simple, two electrodes separated by a dielectric, making this geometry a suitable test-bed for stacked heterostructure formation. While water was used as the dielectric in the first capacitor,[121] most modern dielectrics are now solids composed of materials such as Mylar or barium titanate, the choice of which depends on the desired electrical and mechanical properties.[121] Biasing the device polarises the dielectric and this was the prevailing mechanism until the recent development of supercapacitors. Here, a liquid electrolyte is contained between the electrodes and, under a bias, a layer of ions forms on each electrode creating, in effect, two nanoscale capacitors. This mechanism will be discussed further in Subsection 3.3.3. The majority of layered crystals have wide bandgaps leaving no shortage of candidates for capacitor dielectrics, or to act as the insulating regions critical to vertical heterostructures.

If a voltage is placed across a capacitor, a charge $\pm Q$ will build up on either electrode as shown in Figure 3.6A.[122] Under ideal conditions, the surface charge density will be uniform

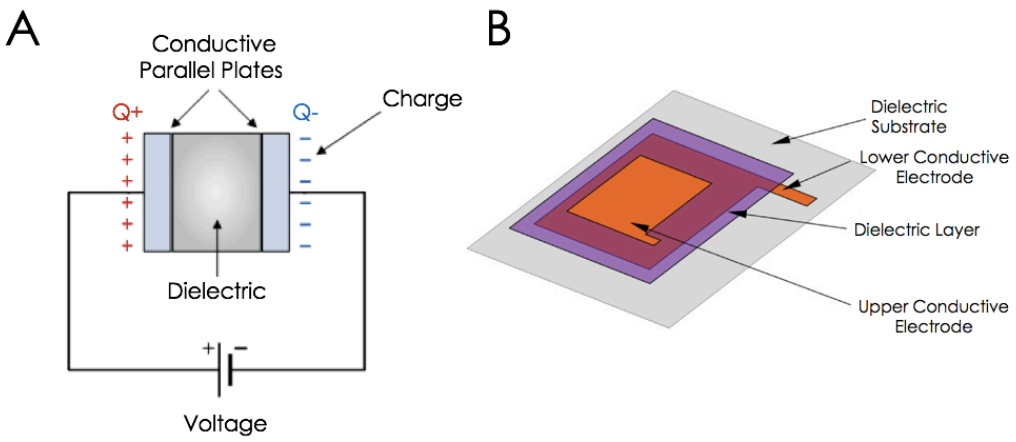

Figure 3.6: Capacitors. A) A parallel plate capacitor. Image from Ref. (122). B) A schematic of a vertically layered capacitor.

across both electrodes, leading to the charge-to-voltage ratio

$$C = \frac{Q}{V} \tag{3.5}$$

where Q is the amount of charge present on either electrode, V is the voltage across the electrodes, and C is the capacitance, a measure of the amount of charge the capacitor can hold. The capacitance is a strong function of the geometry of the device with the property

$$C = \frac{\varepsilon_0 \varepsilon_r \mathcal{A}}{d} \tag{3.6}$$

where ε_0 and ε_r are the vacuum and dielectric permittivities, $\mathcal{A}$ is the overlap area of the electrodes, and d is their separation. For a greater capacitance, one therefore needs a high permittivity dielectric, greater overlap area and a closer spacing meaning capacitor designs are commonly just a thin insulating material with a conductor coated on either side and

then rolled into a cylinder. Unlike a resistor, the current that flows in a capacitor is not proportional to the voltage, but rather the rate of change of voltage.[121] This is shown through time derivative of Eq. 3.5

$$\frac{dV}{dt} = \frac{I(t)}{C} \tag{3.7}$$

where $I(t)$ is the time-dependent current. This is a critical relationship that demonstrates a primary function of capacitors in a circuit; they are often placed in parallel with a power supply or rectifier to smooth the transient fluctuations in a signal as a high capacitance results in a much smaller change in voltage. Another major difference between a capacitor and a resistor is that the power associated with the capacitive current is stored in the electric field between the electrodes rather than dissipated as heat. This means that the energy can be fully retrieved as the capacitor is discharged (ignoring internal resistance).[121] While batteries can store much more energy, a capacitor can charge and discharge current at a much faster rate. This can be shown for a resistor-capacitor circuit through a restatement of Eq. 3.7 using Ohm's Law:

$$\frac{dV}{dt} = -\frac{1}{RC}V(t) \tag{3.8}$$

where $V(t)$ is the time-dependent voltage across the capacitor. The solution to this differential equation contains the term RC, an important quantity for capacitors, such that

$$V(t) = V_0 e^{-t/RC} \tag{3.9}$$

where V_0 is the initial voltage and the product RC is the time constant of the circuit. Time

constants are abundant in physical relations and measure how quickly a system can respond to a stimulus. For a charged capacitor at $t = 0$ s, it will take RC seconds to discharge to e^{-1} ($\sim 37\%$) of the initial voltage and, using the $5RC$ rule of thumb, will decay to 1% in 5 time constants.

These relations pertain to DC circuits and the resistance is extended to AC circuits through impedance. The impedance of a series RC combination is:

$$Z = Z_{Re} + iZ_{Im} = R_{Ser} - \frac{i}{\omega C} \tag{3.10}$$

where R_{Ser} is the series resistance, and ω is the frequency of the signal. The inverse relationship between the impedance and the frequency means the circuit impedance will be simply the series resistance at high frequencies but will act like an open circuit to low frequency or DC currents. Capacitors are thus often used in circuits where an AC output is desired but DC signals are needed to provide power to certain circuit elements.

The few published examples of printed 2D capacitors use them to verify that vertically printed layers are indeed insulated from each other[55,107] and an example schematic of a vertical capacitor is shown in Figure 3.6B. This step is a necessary precursor to more complex devices such as transistors and will be discussed in Chapter 4. Printed capacitors have yet to be integrated into a fully 2D circuit as each specific device has yet to be fully optimised.

3.3.2 Photodetectors

The wide range of bandgaps across the layered crystals means many of the materials show useful optoelectronic characteristics with a broad spectral range. Much work has been done where high quality monolayers form the basis for high performance photodetectors[123,124]

and solar cells.[125,126] TMDs such as WS_2 and MoS_2 are especially well suited for this as they are cheap, abundant, photostable, have high absorption coefficients, and are free of dangling bonds.[127] As the crystal is thinned to a monolayer and the bandgap transitions from indirect to direct, TMDs have been shown to absorb 5 - 10% of incoming sunlight[128] which is remarkable given the 0.65 nm body thickness.[129] c-Si is currently the material of choice for photovoltaics and requires a 50 nm thick film for an equivalent absorption.

Photodetectors are optical transducers that electrically detect optical signals. The simplest type of photodetector consists of semiconductor with ohmic contacts and is shown in Figure 3.7A. When light is incident on the semiconductor, the nature of photocarrier generation depends on whether the material is doped; for intrinsic photoconductivity, an electron-hole pair—or exciton—is created through a band-to-band transition whereas extrinsic photoconductivity occurs by band-to-impurity level transitions (or vice versa) and only one type of carrier is created.[130] For an intrinsic photoconductor, the conductivity, σ, is given by

$$\sigma = q(\mu_n n + \mu_p p) \tag{3.11}$$

where q is the elementary charge, μ_n and μ_p are the electron and hole mobilities, and n and p are the amount of electrons and holes present. The increase in conductivity under illumination thus arises from an increase in the carrier concentration. It bears noting however that in disordered systems such as films of organic molecules, the mobility shows a dependence on carrier concentration.[131,132] This is likely to be the case for disordered networks of nanosheets but has yet to be properly investigated as decoupling a valid mobility value from the conductivity of such networks has proven to be non-trivial.

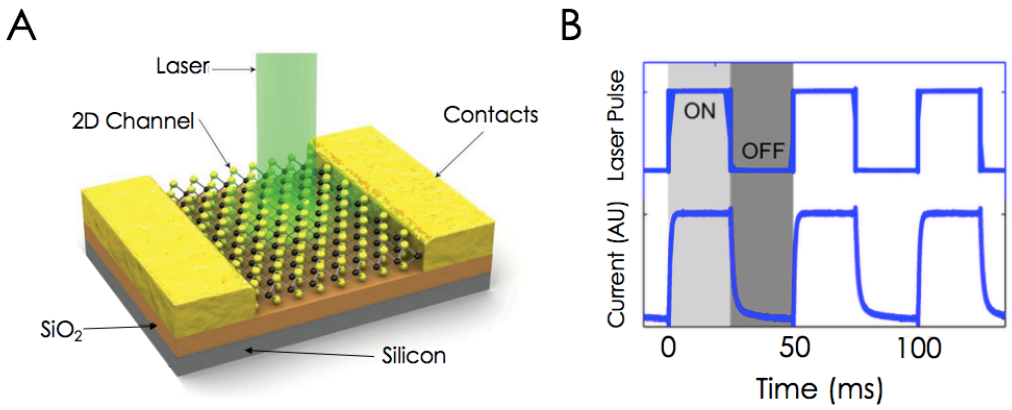

Figure 3.7: Photodetectors. A) A schematic of a basic TMD-based photodetector. Image from Ref. (129). B) Output characteristics for light incident on a photodetector.

A key parameter in a photoconductor is the gain. This is the ratio of the additional current that flows between the electrodes as a result of illumination, I_p, to the photogenerated current, I_{ph} such that Gain $\equiv I_p/I_{ph}$. The photogenerated current is the number of dissociated excitons created per second and is not strictly a true current as the excitons may recombine rather than be transferred to the external circuit. The gain can also be stated as the ratio of carrier lifetime, τ, to the carrier transit time, t_r, such that $t_r \equiv L/v_d = L/\mu E$ where L is the channel length, v_d is the drift velocity, and E is the electric field. For a material with a long carrier lifetime and a short channel length, the gain can be as high as 10^5.[130] A large gain is necessary as a dark current will flow through the semiconductor due to impurities and thermal excitations meaning the photocurrent must be easily detectable above this baseline.

Like all devices, photodetectors do not operate with 100% efficiency. The quantum efficiency, η, of a photodetector is the number of excitons generated for each incident

photon:

$$\eta = \frac{I_p}{q}\frac{hf}{P_{opt}} \tag{3.12}$$

where hf is the photon energy and P_{opt} is the incident optical power at a given wavelength. A key consideration for maximising the quantum efficiency is the absorption coefficient, α, which is a strong function of photon wavelength and thus imposes upper and lower bounds on usable part of the electromagnetic spectrum. For wavelengths longer than the optical bandgap, the values of α are too small for band-to-band excitations and for wavelengths much shorter than the bandgap, α can be too large which means the radiation is mostly absorbed on the surface where recombination times can be short.[130] The semiconductor must therefore be chosen with the wavelength of incident light in mind.

Figure 3.7B shows an example current response to a pulsed laser incident on a photodetector. The response of the device will lag behind the pulse train of the laser and is dependent on material purity and resultant transport characteristics of the device. The rise and fall of the current is double-exponential; the fast component is associated with the equilibration of carrier generation and recombination rates, and the slow component is associated with trap filling.[133] This means networks with a high density of trap states can expect a slow photoresponse and, interestingly, it is suggested that trap density in TMD networks may depend on the chalcogen.[127] The magnitude of trap-limited transport is also a function of the light intensity. As the intensity is increased, electronic trap states become recombination centres and retard the majority carrier lifetime.[127] This is pertinent to LPE materials as the exfoliation process can leave solvent or surfactant residues which are currently unquantified and an effective means for their removal is still unclear.

3.3.3 Transistors

As wartime contracts and assignments wound down after World War II, the abundance of scientists and high technologists took their knowledge and experience to industry where most of the major semiconductor devices were developed. Despite its relative youth as a discipline, the electronics industry is now the largest in the world and contains, at its heart, the transistor. This device has gone from fist-sized at the time of its invention in 1947 to today's microprocessors with a transistor density of 2.5×10^7 mm^{-2}.[134] This astonishing scaling was predicted in 1965 by Gordon Moore when he described a doubling in the number of components on a circuit every 2 years.[135] This observation has been a roadmap for manufacturers and chips with 7 nm feature sizes are now in production. The fabrication of such small feature sizes requires significant financial, political, and human capital and is thus limited to large corporations. However, the growth of the electronics industry has branched many fields where high performance and high-cost fabrication are unnecessary. The comparative ease of manufacture and deposition has made 2D materials attractive for integration into transparent, flexible devices and even enabling new functionalities.

There are many types of transistor available but the metal/oxide/semiconductor field-effect transistor (MOSFET) has been the most important device for digital electronics due to key attributes such as low power consumption, an enormous manufacturing yield, and it can be constructed entirely out of silicon and its oxides. The following section will describe the operation of a typical MOSFET as the fundamentals are applicable to the variant transistors described later.

A cross-sectional view of a MOSFET is shown in Figure 3.8A.[136] The device consists of an n-type semiconductor substrate with two p-regions that constitute the the source and drain

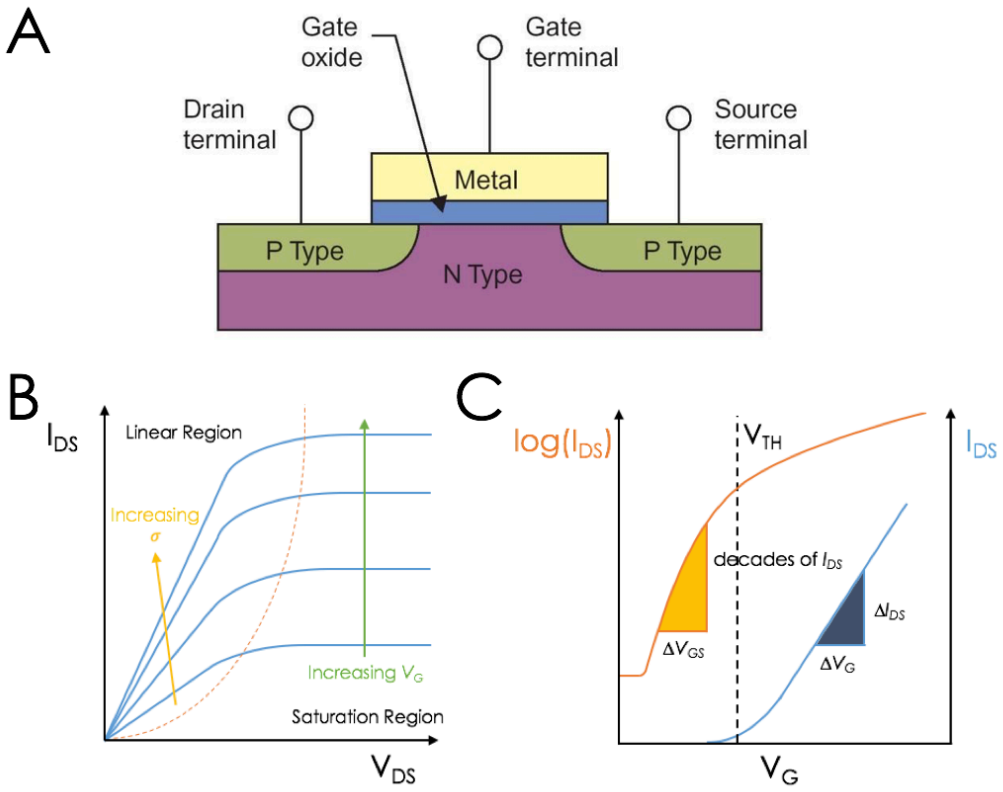

Figure 3.8: Transistors. A) A cross-section of a basic FET structure. Image from Ref. (136). B) Output curves for a range of gate voltages. C) Transfer curves; the orange curve shows current behaviour logarithmically and the blue shows the current linearly.

electrodes. A degenerately-doped, or metallic, gate electrode is then electrically insulated from the substrate by a thermally grown oxide layer. The basic device parameters are; L, the channel length; w, the width of an electrode; t, the oxide thickness; and the substrate doping.[130] During operation, the source contact is used as a voltage reference for both the gate and the drain and, with zero gate bias, only very low currents should flow through the channel when the drain is biased against the source.[130] When a sufficient gate bias is applied, carriers are drawn from the semiconductor body to the oxide interface where they

accumulate into a thin layer ($\sim$ 5 nm) between the electrodes known as the inversion layer. The conductivity of the inversion layer is many orders of magnitude higher than the surrounding semiconductor due to the enormous increase in carrier density meaning large currents flow between the contacts.

The key relationships are between the current and the drain-source voltage, V_{DS}, and the gate voltage, V_G. These voltages are the independent variables on the output (V_{DS}) and transfer (V_G) curves. Figure 3.8B shows an output curve for a range of gate voltages. There are two regions of current response that arise from the carrier dynamics in the inversion layer. If a small V_{DS} is applied, carriers flow between the drain and the source and the channel behaves like a resistor whose conductivity is modulated by V_G. The behaviour of the current is derived in Appendix B.1 (page 157) and stated here as

$$I_{DS} = \frac{w}{L}\mu C(V_G - V_T)V_{DS} \tag{B.10}$$

where μ is the mobility, C is the device capacitance, and V_T is the threshold voltage, the voltage beyond which the device is considered switched on. As V_{DS} is increased, the current eventually saturates as the thickness of the inversion layer is reduced to zero at the contact interface due to the growth of the depletion region around the drain. This is known as the pinch-off point and the number of mobile electrons at the drain is drastically reduced. The dashed line in Figure 3.8B represents a locus of saturated I_{DS} vs saturated V_{DS}. The current behaviour in the saturation region is also derived in Appendix B.1 and stated here as:

$$I_{DS} = \frac{w}{2L}\mu C(V_G - V_T)^2 \tag{B.14}$$

This equation predicts an eventual decline in the current as the charge density at the pinch-off point goes to zero and changes sign as holes accumulate at the interface. However, these holes do not contribute to the current flow as the drain contact is reverse-biased with respect to the channel so hole injection into the drain is blocked. Therefore, the current saturates at a maximum value and stays constant for higher V_{DS}. Transistors for signal processing and switching are operated in this region.

Figure 3.8C shows the transfer curves that describe the relationship between I_{DS} and V_G. The linear axis reveals a useful parameter for transistor analysis where the derivative of the current in Eq. B.10 with respect to the gate voltage (for a constant V_{DS}) is known as the transconductance, g_m:

$$g_m \equiv \left.\frac{\partial I_{DS}}{\partial V_G}\right|_{V_{DS}} = \frac{w}{L}\mu C V_{DS} \tag{B.16}$$

This is a measure of the efficiency of transducing a small gate bias into a large current and is an important figure of merit for transistors; steep transfer curves mean only small voltages are needed to output a large current. Modern silicon FETs operate at values of tens to hundreds of milliSiemens but similar values can be reached with variant transistors, discussed further below. When the device is operating a zero gate bias, a leakage current can still flow through the semiconductor known as the off-current. This value needs to be minimised so that the ratio of the on-current, the operating current, to the off-current is as large as possible. This is known as the on:off ratio and is another important figure of merit.

The logarithmic axis shows information about low current behaviour. When the gate voltage is below the threshold voltage, the semiconductor/oxide interface is only weakly inverted and the resultant current is called the subthreshold current. The subthreshold

region is important for low-voltage, low-power operations as it describes how the device switches on and off. The important parameter here is the subthreshold swing, the yellow highlighted area in Figure 3.8C. This is the change in gate voltage required to change the current by one order of magnitude (or decade) and measures how quickly the transistor can be turned on and off. The continuous advancement of FET-based processing requires high on:off ratios at low supply voltages but progress is diffusion-limited to 60 mV/decade at 300 K.[137] In reality however, scaled MOSFETs have values closer to 70 mV/decade due to short channel effects.[138] This floor in subthreshold swing can be breached with 2D materials as FETs with an MoS_2 channel have shown subthreshold swings as low as 6 mV/decade by incorporating layers of ferroelectrics and high-$\varkappa$ dielectrics.[139]

The first nanosheet-network transistor was a printed graphene film that was electrostatically gated using a silicon wafer.[53] In the intervening years, the development of a fully printed transistor stalled as a number of issues had to be addressed, particularly in relation to printed vertical heterostructures. A major electronic issue however is the shunting of the gate voltage as the gate field decays into the film which severely limits performance in thicker films. This was noted by the authors in Ref (53) as they noticed field-effect modulation was retarded in films thicker than 40 nm. This particular issue can be addressed using an alternative gating method developed for organic electronics.

Electrolytically-gated Transistors

The use of an electrolyte to reversibly dope a film was first developed in the 1980s for semiconducting polymers[140] and, through subsequent investigations, organic electrolytically-gated transistors (EGTs) now have two basic operation mechanisms

depending on the permeability of the film. If the film is impermeable, such as that shown in Figure 3.9A, a gate bias will cause an accumulation of the electrolyte ions at the gate-electrolyte interface and at the electrolyte-channel interface. This ionic build-up will screen the gate charge but the accumulation at the semiconductor creates a large electric field which draws an equal accumulation of charge carriers to the electrolyte-semiconductor interface. The accumulation of ions and counter charges at an interface is known as an electric double layer (EDL) and is a long-studied phenomenon.[141] The EDL can be modelled as plane dielectric capacitor with the dielectric thickness on the order of nanometres. Such a small thickness means that an electrolyte can create an areal capacitance above 10 μF cm^{-2}, almost two orders of magnitude higher than common electrostatic values.[141] The two EDLs can be modelled as two capacitors in series meaning the device capacitance is $C_{Total} = (C_G^{-1} + C_{Ch}^{-1})^{-1}$ where C_G and C_{Ch} are the capacitances at the gate and channel, respectively. This relationship means that the device capacitance is dominated by the smaller capacitor and, to ensure dominance of the channel, the rule of thumb is to keep the gate capacitance at least a factor of ten higher.[142]

If the semiconductor film is permeable, as shown in Figure 3.9B, the ions can penetrate into the bulk which modulates the conductivity through reversible doping. This process is also purely capacitive as no charge is exchanged with the semiconductor but rather carriers are drawn from the external circuit to compensate for the additional charge. This bulk penetration is a key difference in operation as it means that the entire film can be gated so thick films can be switched as easily as thin ones. Since the gating effect is now volumetric instead of areal, Eq. B.10 needs to be amended to reflect this. The C refers to the interfacial capacitance and is in units F cm^{-2} so substituting $C = C_V \times t$, where C_V is the volumetric

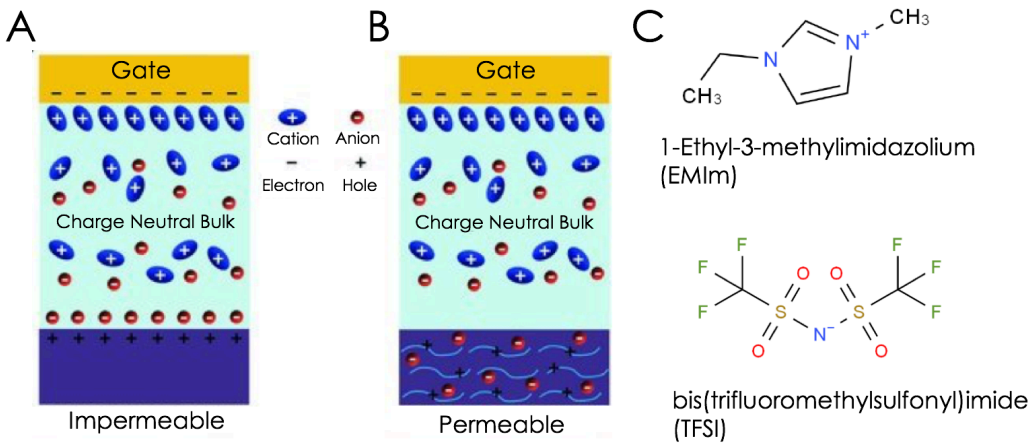

Figure 3.9: EDLs and ionic liquids. A) An impermeable semiconductor. The ions from the electrolyte accumulate on the surface of the semiconductor which draws carriers to the interface to create an electric double layer. B) A permeable semiconductor. The ions can penetrate the material causing a doping effect which draws counter-charges in from the external circuit. Images A) and B) from Ref. (141). C) The molecular structure of EMIm TFSI.

capacitance in F cm^{-3} and t is the film thickness, Eq. B.10 becomes

$$I_{DS} = \frac{wt}{L}\mu C_V(V_G - V_T)V_{DS} \tag{3.13}$$

Contrary to classical FETs where the thickness of the channel does not affect the current, it is yet another tuneable parameter in an EGT.

The benefits of permeable and impermeable gating are consolidated in nanosheet networks. The porosity of a printed nanosheet network means that an electrolyte can penetrate the internal free volume but also means that EDLs form on the basal planes of the nanosheets under a gate bias. The 'long-channel' effects normally associated with EDL-based FETs are also addressed with this style of device as a current that flows along the semiconductor-electrolyte interface over a long distance is often quite small.[141] This is a

challenge for printed devices as channels are generally quite long (> 50 μm) but is overcome in nanosheet networks as EDLs form throughout the volume of the film meaning two-dimensional currents can flow through a three-dimensional channel. This means large currents can be driven without the uncertainties of doping and dedoping associated with ion penetration of a permeable network.[141]

EDLs have traditionally been investigated using salts dissolved in a large amount of solvent (typically water) but recent discoveries have unearthed a class of compounds with extremely useful characteristics. Room temperature ionic liquids (RTILs) possess a chemically unique combination of properties such as a high charge density, electrochemical stability, negligible volatility, tunable polarity, and, importantly, are composed *solely* from anions and cations that melt below 100–150 °C.[143,144,145] The exclusion of water means that the −1.23 V standard potential can be surpassed with a cation that reduces at a larger value and, through pairing with a suitable anion, RTILs with a stable electrochemical window over 6 V have been reported.[146] There is enormous scope to create bespoke RTILs as the cations and anions can be easily mixed and matched to create desired characteristics (wider liquid-phase temperature range, specific electrochemical windows, etc).[143] Shown in Figure 3.9C is a benchmark RTIL developed for electrolytic gating, EMIm TFSI. This is the RTIL of choice for switching applications as its properties include a suitably large electrochemical window (~ 5.5 V) and a high ionic conductivity (~ 10^{-3} S m^{-1}).[143]

3.4 The Field of Printed Electronics

The current interest in printable 2D-based electronics is due to the simplicity of generating large quantities of material and the enormous variety of properties covered by the material class. However, as has been alluded to already, the concept of printable electronics is not new and existing technologies have already matured to the point where they are competitive with amorphous and polycrystalline silicon. This section will briefly review the field through assessment of the strengths and weaknesses of each subfield.

Organic Electronics

The development of organic semiconductors began in the 1980s making it one of the earliest materials to promise printable electronics.[147] In the subsequent time, the number of organic semiconductor materials has grown exponentially to the point where a review takes an entire book.[148] Several important advances in molecular structure have taken place such as the synthesis of p-type, n-type, and ambipolar materials, and the development of solution-processable polymeric semiconductors.[149] Of these, a number of high performance materials have emerged such as P3HT,[150] TIPS-pentacene,[151,152] and BTBT.[153,154] The high performance of these materials has been accomplished through clever engineering of film crystallinity, contact schemes and dielectric environment.[155,156,157]

It appears unintuitive but the large material diversity across organic semiconductors can be a disadvantage. The dynamics of inter- and intra-molecular transport means there are a variety of defect and trapping mechanisms that are still not fully understood. Molecular and crystalline defects often lead to strong device-to-device variation in mobility which leads to issues for large scale interaction and logic applications.[158] Although on:off ratios are

frequently > 10^6, many of the organics still struggle to compete with amorphous silicon due to low mobility. Further, the small number of n-type semiconductors and overall low conductivity has limited the pursuit of organic CMOS applications.[159]

A major challenge with organic semiconducting materials is their environmental instability.[157] Oxygen and water exposure have been shown to be an important source of degradation for high-performance polymer semiconductors.[160,161] The polymeric semiconducting materials have shown great promise in inkjet printing applications[162] and flexible electronics,[163] however devices with multiple components still face significant manufacturing disadvantages as each subsequent solvent must not dissolve the previously deposited layers.

Carbon-Nanotube Networks

Since the early 2000s, carbon nanotubes (CNTs) have been of huge interest as a scalable semiconducting material. Much of this has come from the fact that single-walled CNTs (SWCNTs) show almost ideal semiconductor behaviour with a bandgap of 0.7–1 eV and near-ballistic transport.[164] Significant efforts have gone towards developing CNTs for high performance logic circuits with individual CNTs[165] and medium performance printable transistors with random and aligned CNT networks.[166]

A significant hurdle to both of these efforts has been the lack of selectivity. CNT synthesis produces a mixture of metallic and semiconducting nanotubes which is detrimental to the performance of network transistors. However, electrophoresis,[167] density gradient ultracentrifugation,[168,169] gel chromatography,[170] and selective solubilisation[171] techniques have each been able to purify the SWNTs to usable levels. Recent scaling efforts

have combined polymeric selectivity with shear-force mixing which has shown good success in creating litre quantities of material.[172] Despite some considerable challenges, the CNT benchmarks have been impressive; CNT FETs now outperform silicon, the channel lengths can be sub-10 nm with device footprints of 40 nm, and ballistic transport means the devices have progressed beyond the use of mobility as a suitable metric.[173]

While the push for large-scale production of SWCNTs is underway, general scalability of the purification techniques for SWCNT is still lagging, providing only gram quantities with significant chemical waste and questionable toxicity.[174] This means that even if selective solubilisation through shear-force mixing can be scaled to the level of global demand, the path to commercialisation is still unclear as both selecting polymers and scaled centrifugation are costly. In addition to the scaling demands, performance issues with the networks themselves remain. Due to the residual metallic SWNTs and the junction resistance at the intertube contacts, CNT network transistors suffer from a scaling limitation where channels with a high CNT density or long tube length show high mobility but poor on:off ratio and vice-versa.[171]

Colloidal-Nanocrystal Networks

Another approach to solution-processable thin films is through semiconducting colloidal nanocrystals (CNCs). These CNCs are usually synthesised using liquid- or gas-phase techniques[175,176] which confers a very high level of control over the nanoparticle composition and size[176] and the NCs can easily be dispersed by solvation with additional ligand chemistry.[177]

CNC films show highly attractive properties for low temperature, printable, flexible

electronics and CNC FETs have been demonstrated with Si, Ge, CdX and PbX (X=S, Se, Te) nanoparticles.[178] Si and Ge films generally show a disordered hopping transport analogous to organic films that similarly limits performance.[179,180] However, recent developments in core-shell nanoparticle structures and ligand conversion have led to band-like transport in PbX CNC films.[181,182] This grants a higher network mobility than that achievable with organics as the state-of-the-art appears to be 22 $cm^2\ V^{-1}\ s^{-1}$.[183]

The synthesis and handling of CNC films is quite restrictive; an inert atmosphere is required for many processing steps[184] and there remains a high level of environmental susceptibility for final devices.[185] The electrical performance for CNC films has generally been quite poor compared to polymer TFTs[184] but this may be due to the comparative lack of tunability during processing. The behaviour of CNC FETS has suffered from strong percolation effects where a thick channel is required to drive adequate currents[186] but the commensurate off-current increases degrade the on:off ratio thus limiting low-power performance. Similar to the first printed graphene transistor, thicker films lead to less effective gate modulation.

Layered-Crystal Networks

Before the solution processing techniques were refined for layered crystals, many of the exciting benchmarks were set with samples that were either mechanically exfoliated or CVD-grown. As the challenges associated with a new field were addressed (low yields, ink refinement, compatible deposition, etc.), the printed electronics began to emerge. Printed nanosheet networks of MoS_2,[187] black phosphorous,[188] and WS_2[48] have been used as photodetectors with the latter being implemented into a fully printed electronic circuit. A

range of printed sensors have also been demonstrated such as an MoS_2 ammonia sensor,[189] a black phosphorous NO_2 sensor,[190] and a graphene strain gauge on a paper substrate.[191]

The first printed graphene network transistor in 2012 exhibited a mobility of 95 $cm^2\ V^{-1}\ s^{-1}$, far higher than current state-of-the-art organics. However, due to the semimetallicity of graphene, the on:off was limited to < 10. This was built upon in 2017 when Carey *et al.* reported a fully inkjet printed graphene transistor (silver contacts, a graphene channel, with a BN dielectric) and, while mobility improved to ~ 150 $cm^2\ V^{-1}\ s^{-1}$, the on:off dropped to 1.2.[107] There are a number of challenges in printing transistors fully composed of nanosheet networks (some of which are addressed in this work) which has meant that there is currently a paucity of reports, but this is simply indicative of a nascent field. Further to this, there is currently no understanding of the charge transport dynamics in nanosheet networks which limits the usefulness of a cross-field comparison. However, some comments can be made.

The clearest relationship among each of these material technologies is that any printed film is composed of discrete particles. This is the fundamental issue restraining the mobility in each case as the carriers must either hop or tunnel at each interparticle junction. For TMD networks, a clear route to optimisation is available as reporting grows on TMD ligand and chemical functionalisation.[192,193,194] This has the potential to reduce the junction resistance to allow the network mobility advance towards the basal plane mobility of the various TMDs. However, there may be a more facile method to improve the network mobility; building upon the polymer-CNT composite work, the addition of a conductive filler to a semiconductive network may improve the charge transport between the electrodes. This idea forms the basis for Chapter 6 and will be discussed in greater detail.

Printable organic electronics benefit from a huge number of different materials and the

ability to mix materials for additional functionality. However, the co-solubility of these materials requires that subsequent processing steps use non-interacting solvents. In addition, polymer materials still suffer from intrinsic polaronic scattering mechanisms and are strongly dependent upon appropriate crystallinity which may prove challenging for sophisticated multi-part devices. In contrast, liquid-exfoliated materials have the same large range of properties but are less sensitive to disorder and orthogonal solvents are often not required. The inclusion of binders has also been shown to reduce interlayer redispersion as successive layers are deposited which is critical for creating robust devices.[65]

Looking to the future of printed electronics, printed nanosheet networks appear to combine many of the desirable qualities of the other printable technologies. The youth of the field is also an advantage as there is enormous scope for improvements in the performance and reliability of many of the reported applications. The combination of material scalability, simplicity, and variety, coupled with the growing field of additive manufacturing has led to increasingly competitive research and an explosion in patents with no sign of slowdown.

We live in a society exquisitely dependent on science and technology, in which hardly anyone knows anything about science and technology.

Carl Sagan

4

Insulating the Vertical Layers

The entry of nanosheet networks into the field of printed electronics had—at the time of publication in 2016—generally relied on planar devices to demonstrate material and device viability. As the devices become more complex, it is necessary to have the ability to pattern structures both laterally and vertically to reduce geometric footprints and enable new device functionalities. The move to vertical patterning

brings a host of challenges at each step along the design chain, from choice of bulk powder to choice of solvent vehicle, but it is critically important to be able to electrically isolate components from one another within the vertical architecture.

This is a key limitation when using nanosheet networks in conjunction with deposition methods that rely on low concentration inks, such as inkjet printing. As each pass of the printhead deposits a sparse amount of material, the resultant network will be filled with discontinuities until a continuous limit is reached, determined by percolation. The network discontinuities act as pinholes, a phenomenon long encountered in printed organic networks,[195,196] and can cause device failure through unwanted interlayer contact. This problem can be investigated by developing vertical capacitors composed of conductor-insulator-conductor nanosheet networks as interfacial charge can only accumulate when the insulating region is pinhole free. While ultrathin clay dielectric layers (such as montmorillonite) have been reported,[197] the required layer-by-layer approach is time consuming and incompatible with printed strategies.

This chapter presents a methodology for printing continuous dielectric networks of BN using a combination of inkjet printing and spray coating. This work began with the intention of consolidating the fabrication under a single deposition process however, regardless of solvent, a continuous BN layer could not be formed in this manner. This could be attributed to the low density of BN powder (the MSDS describes it as a 'nuisance powder') which makes successive layering difficult as the BN network redisperses easily in most solvents. A polymeric binder was deliberately omitted from the BN ink to preserve the purely-2D nature of the devices as its inclusion would beg the question, "if a much thinner polymer layer can be used, why bother with BN at all?" The devices are thus

fabricated from inkjet-printed graphene networks as top and bottom electrodes and a spray-coated BN network as the dielectric. For continuous dielectric layers, the DC current through the capacitor will be zero which allows the device characteristics to be evaluated through impedance spectroscopy. The geometric scaling of the capacitance can then be explored through variation of the device dimensions where the expected linear evolution of the capacitance will again confirm that the dielectric layer is continuous. As will be shown, this work is a necessary precursor to the more complex electronics presented in Chapter 5.

4.1 Experimental Procedure

The bulk powders used in this study were purchased from commercial sources; graphite from Imerys (TIMREX, >99.5%), and the BN from Sigma Aldrich (>98.5%) and used as supplied. The solvents used were HPLC grade and also purchased from Sigma, unless otherwise specified.

The graphene ink was prepared through the LPE techniques outlined in Section 2.2.1. 4 g of graphite was immersed in 80 ml of N-methyl-2-pyrrolidone (NMP) for an initial concentration of 50 g L^{-1}. This precursor dispersion was then tip-sonicated using a Sonics Vibra-cell VCX-750 ultrasonic processor for 7 h at 60% amplitude and cooled using an ice bath. The resulting polydispersion was then subjected to a two-step centrifuge cascade to give a final size distribution compatible with the inkjet printer. The centrifuge regime was 546 g for 90 mins after which the sediment was discarded and the supernatant was then centrifuged at 1257 g for 90 mins. The sediment was then collected and redispersed in 10 ml of fresh NMP.

The BN ink was prepared in the same manner but using isopropanol (IPA) as the solvent.

This precursor dispersion was also sonicated for 7 h but 5 ml of solvent was added every 1.5 h to offset the evaporation of the IPA. The sonicated polydispersion was then centrifuged at 120 g for 90 mins and the supernatant retained and centrifuged at 426 g for 90 mins. The sediment was then redispersed in 10 ml of fresh IPA. Optical extinction was measured on a Varian Cary 500 in quartz cuvettes with a path length of 0.4 cm in 1 nm increments.

The graphene electrodes were inkjet printed with a Dimatix DMP 2831. The platen temperature was set to 60 °C to aid evaporation of the NMP (*cf.* boiling point ~ 202 °C), with the cartridge set to 40 °C. An interlayer delay was also set to 5 mins to allow as much solvent to evaporate as possible. The substrate was alumina-coated polyethylene teraphtalate (PET) from Mitsubishi Paper Mills. This substrate is specifically designed to prevent droplet wetting and thus provide more tightly controlled line edges. Following deposition, the samples were annealed in a vacuum for 24 h at 100 °C to remove as much residual NMP as possible.

The spray coating of the BN layer was performed with a Harder and Steenbeck Infinity Airbrush attached to a Janome JR2300N mobile gantry. The smallest nozzle (150 μm) was used to give fine control over the deposition volume to aid the homogeneity of the BN films. The thickness of the BN films was subsequently measured using a mechanical profilometer. The AC impedance was measured using a Gamry 3000 potentiostat within the frequency range of 10–10^6 Hz.

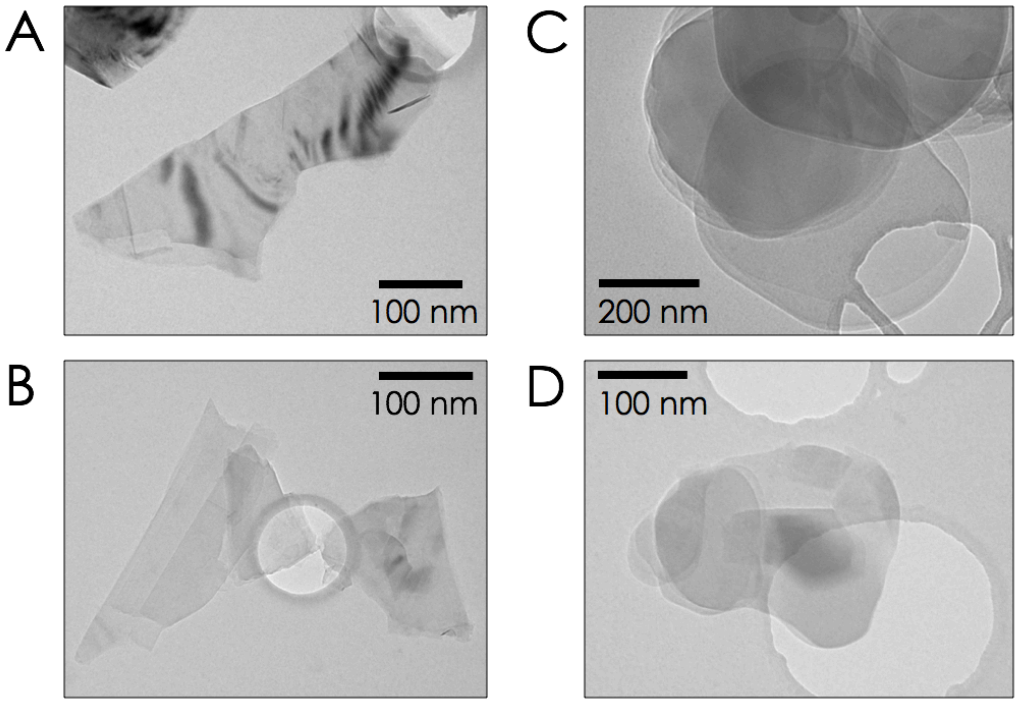

Figure 4.1: TEM images. A, B) Graphene nanosheets. C, D) Boron nitride nanosheets.

4.2 Results and Discussion

4.2.1 Material Analysis

A TEM survey was initially performed on each ink to assess the characteristics of the nanosheets. Figures 4.1A and B show representative images of graphene nanosheets and, as can be seen by comparison, there are a variety of nanosheet thicknesses present in the ink. Figures 4.1C and D show representative images of the BN nanosheets and, by inspection, these sheets appear larger and thicker than their graphene counterparts. The disparity in nanosheet dimensions is necessary as each deposition method has a specific dimensional tolerance. As the graphene ink was inkjet printed, the nanosheet dimensions are limited to

$\sim$ 2% of the nozzle diameter to prevent clogging in the printhead.[53] The BN ink was deposited using an airbrush whose nozzle aperture was several hundred microns meaning no such dimensional limitation constrained the size of the BN nanosheets. This allowed the average lateral length of the BN to be chosen to give an appreciable amount of material as the yield of larger nanosheets is much higher than than that of smaller ones. This was especially useful for finding the lowest thickness before the onset of shorting through trial and error. However, this also highlights one of the drawbacks of LPE where one can create long and thick or small and thin nanosheets, but (currently) not vice-versa.

A photograph of the graphene and BN ink is shown in Figure 4.2A. It is possible to extract information about the nanosheet dimensionality though the optical spectra of such inks, and this is now a well-established practice.[198,199,200] The inks fabricated for this work are thus characterised following the study of Backes *et al.*[199] The optical spectra are taken and interpreted through the Lambert-Beer law, $Ext = \varepsilon Cl$, where Ext is the extinction (often erroneously called the absorbance), ε is the extinction coefficient, C is the dispersion concentration, and l is the path length. The size-independent extinction coefficient at 750 nm was reported to be $\varepsilon_{750} = 5450$ L g^{-1} m^{-1}, which provides a concentration of ~ 3.3 g L^{-1} for the graphene spectrum shown in Figure 4.2B. The broad and featureless optical spectrum of graphene generally precludes a size-dependent metric however, some subtle changes allow a layer thickness to be determined through

$$\langle N \rangle = 38.7 \times \frac{\varepsilon_{550}}{\varepsilon_{325}} - 14.8 \tag{4.1}$$

where ε_{325} and ε_{550} are the extinction coefficients at 325 nm and 550 nm, respectively. Applying this to the graphene spectrum in Figure 4.2B gives a mean layer number, $\langle N \rangle$, of

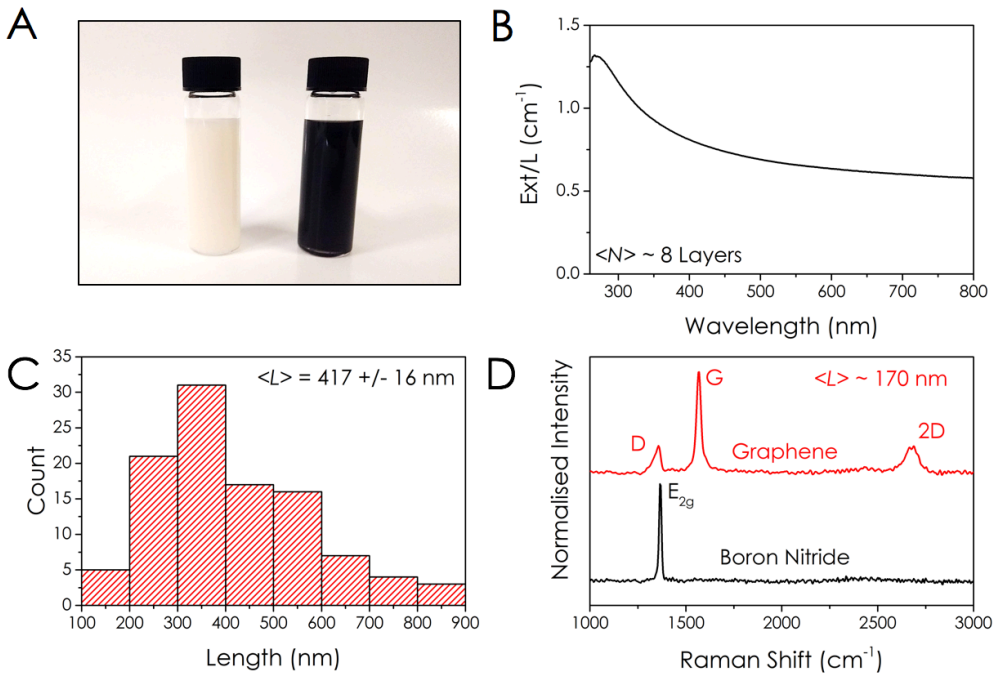

Figure 4.2: Nanosheet analysis. A) Photograph of the graphene and BN inks. B) UV-Vis spectroscopy of the graphene ink. C) 103 counts of BN nanosheets. The <*L*> of the basal planes was extracted as 417 nm. D) Raman spectra collected from the graphene and BN portions of a capacitor.

~ 8 monolayers.

As the graphene ink was NMP-based ($Z = 17$),[53] no additives were necessary to tune the rheology to fall within the printable range defined by the inverse Ohnesorge number (Figure 3.2, page 40). The graphene ink was then diluted down to 1.6 g L^{-1} to align the concentration with that reported by Finn *et al.* to prevent nozzle clogging.[187] Inks deposited with an airbrush have no such rheological constraints due to the atomisation of the ink and the much larger nozzle size. This allows low boiling point solvents such as IPA to be used which are preferable as the solvent will evaporate much faster, leaving fewer inhomogeneities in the film.[87] The use of a solvent different to that of the graphene ink

serves a second function; when depositing the second layer of a heterostack using the same solvent as the first layer, the interface between the films is prone to redispersion on contact with the solvent.[65] This is particularly true for high boiling point solvents such as NMP where films retain residual solvent even after an annealing step.[74]

At the time of publication, no such optical metrics existed for BN (although UV-Vis and Raman metrics are now available[201]) so the average nanosheet length was extracted through statistical TEM imagery. Figure 4.2C shows a histogram of the nanosheet lengths for 103 nanosheets giving an average of $\langle L \rangle \sim 420$ nm. The concentration of the BN ink was obtained by weighing and diluted to 0.5 g L^{-1}. This concentration was chosen as reaggregation was observed at higher loadings. Figure 4.2D shows Raman spectra for the graphene and BN films and the expected peaks confirm the fidelity of the material after deposition. Backes *et al.* also provide a Raman metric for extracting $\langle L \rangle$ for graphene from the FWHM of the G-band which, from Figure 4.2D, gives an average graphene length of ~ 170 nm.

4.2.2 Capacitor Overview

The capacitors presented here are vertical heterostructures composed solely of nanosheet networks which were sequentially deposited according to the schematic in Figure 4.3A. The bottom electrodes were fabricated with 20 passes of the inkjet printer to yield a film ~ 400 nm thick.[187] The dielectric layer was then spray coated using a polymeric mask to shield the substrate from contamination. The top electrode was inkjet printed in a manner identical to the bottom electrode and the overlap area was thus controllable by varying the width of the top electrode.

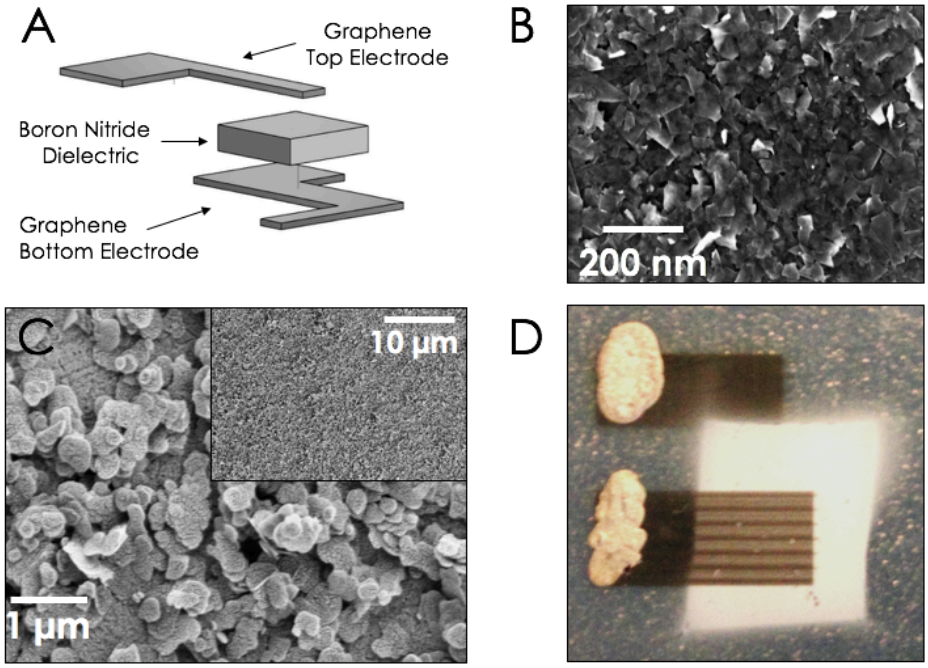

Figure 4.3: Capacitors. A) Schematic of the capacitors. B) SEM image of the graphene electrodes. C) SEM image of the BN dielectric layer. Inset: A lower magnification image showing long-range homogeneity. D) Photo of a representative device.

SEM inspection of the films shows homogeneity over large areas. Figure 4.3B shows the graphene network, representative of both the top and bottom electrodes. Figure 4.3C shows the BN network which showed good long range continuity (inset), albeit with noticeable surface roughness. The degree to which surface roughness is influenced by the deposition method is currently unclear but, looking at CNT work, it is likely that better nanosheet alignment could be achieved through techniques such as spin coating. Figure 4.3D shows a finished device with overlap dimensions of 2.5×1 mm^2 and painted silver contact pads to facilitate good contact with the measurement probes.

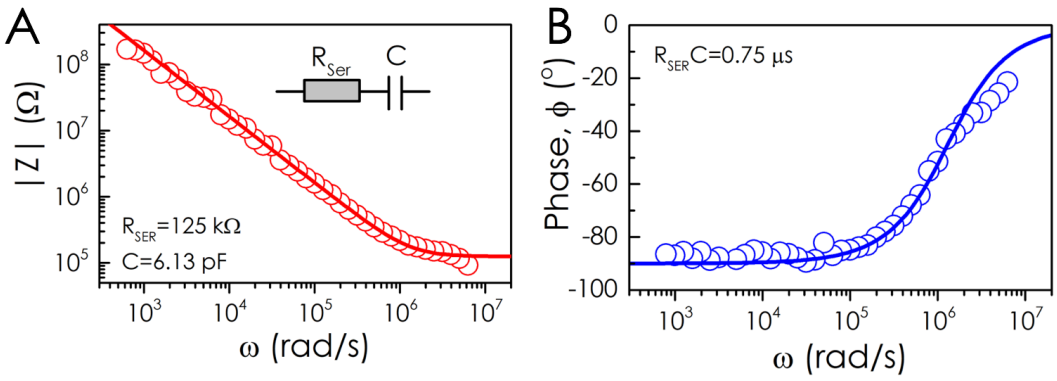

Figure 4.4: Bode plots. A) A Bode magnitude plot with impedance amplitude, $|Z|$, and (B), phase angle, φ, as a function of angular frequency, ω. The lines represent fits to an equivalent series *R*-*C* series circuit, shown inset in (A). Fit constants are given in the panels.

4.2.3 Impedance Spectra

The capacitive properties of the devices were determined through impedance spectroscopy. Figures 4.4A and B show representative Bode magnitude and phase plots for a device with with a 4.15 µm thick dielectric layer and a 2.5 mm² overlap area. These data are equivalent with a series *R*-*C* circuit and are described by

$$Z = Z_{Re} + iZ_{Im} = R_{Ser} - \frac{i}{\omega C} \tag{4.2}$$

where Z_{Re} and Z_{Im} are the real and imaginary components of the impedance, R_{Ser} is the series resistance, and ω is the frequency of the signal. At low frequencies, the fully capacitive interface dominates the impedance and the phase shift approaches -90°, whereas at high frequencies, the diminished contribution from the capacitor means the resistive component dominates the circuit and the phase approaches 0°.

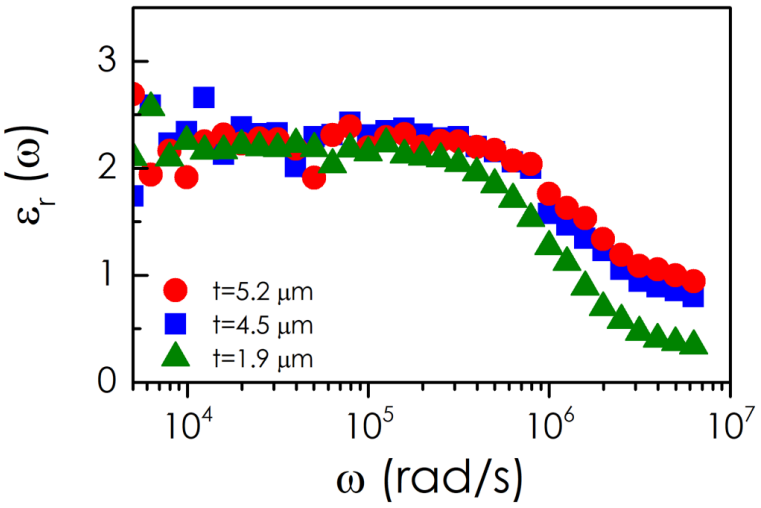

Figure 4.5: Frequency-dependent permittivity. The permittivity is constant at the frequencies where the BN can respond to the AC current.

Through Eq. 4.2, the impedance magnitude is given by

$$Z = \sqrt{R_{Ser}^2 + (\omega C)^{-2}} \tag{4.3}$$

and the phase is given by

$$\varphi = \tan^{-1}\left(\frac{1}{\omega R_{Ser} C}\right) \tag{4.4}$$

These equations give good fits to the data in Figures 4.4A and B (solid lines), where the fit constants provide a series resistance of 125 kΩ, an absolute capacitance of 6.13 pF (0.245 nF cm^{-2}), and an RC time constant of 0.74 μs for this device geometry. The series resistance is significantly higher than the ~ 2 kΩ than expected for the electrodes considering the in-plane conductivity of ~ 10^4 S m^{-1} for graphene networks.[202] It is possible to attribute this to a large out-of-plane flow of charge in these devices as there is approximately a thousand-fold charge

transport anisotropy in single-crystal graphite[203] and MoS_2 networks have also shown a one thousand-fold difference between in-plane and out-of-plane conductivity.[204]

The impedance spectra can also be used to directly calculate the frequency dependence of the relative permittivity, ε_r. The potentiostat outputs both the real and imaginary components of the impedance and, through Z_{Im}, the capacitance can be calculated through $C(\omega) = [i\omega Z(\omega)]^{-1}$. These values can then be transformed into the frequency-dependent relative permittivity using the standard dimensional expression for capacitance such that

$$C = \varepsilon_r \varepsilon_0 \frac{A}{t} \tag{4.5}$$

where the symbols have their usual meaning. In Figure 4.5, $\varepsilon_r(\omega)$ is plotted against the frequency for three capacitors of different thicknesses. For $\omega < 10^5$ rad s^{-1}, the relative permittivity was invariant with both thickness and frequency at ~ 2–2.5, in agreement with previous reports.[205] For higher frequencies, the polarisation mechanisms cannot respond to the signal and $\varepsilon_r(\omega)$ declines as is common for dielectrics.

4.2.4 Dimensional Analysis

An array of capacitors was printed to confirm the dimensional scaling of the capacitance according to Eq. 4.5. This was achieved by printing a uniform array of bottom electrodes upon which dielectric layers of various thickness were sprayed with a constant electrode overlap area, and dielectric layers of constant thickness with various electrode overlap areas. As spray coating is a blanket deposition technique, this required the use of a polymer mask whose apertures could be successively closed off to create the thickness variation in the dielectric layers. The capacitance was then extracted by fitting the impedance spectra

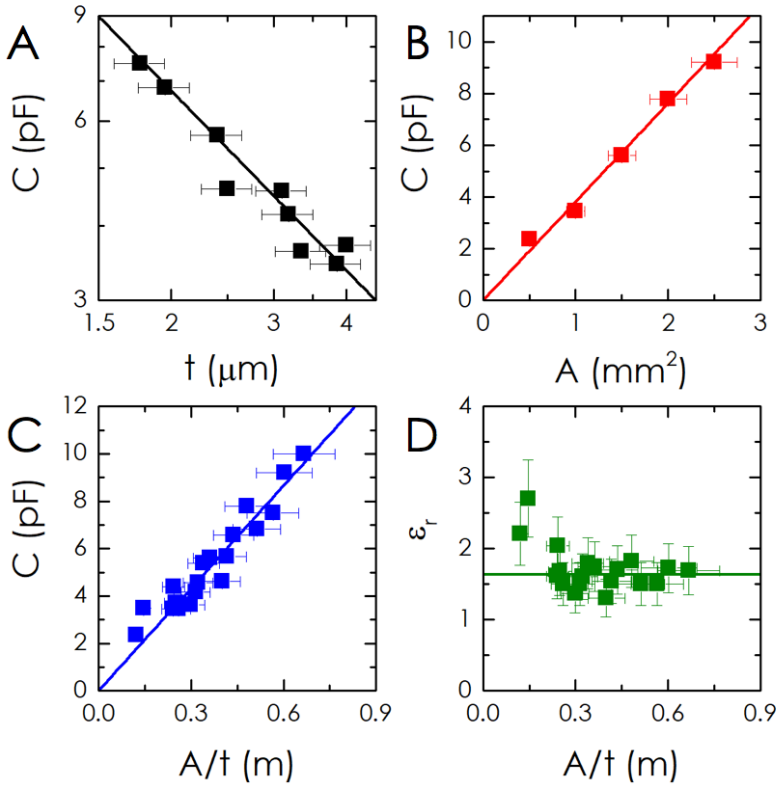

Figure 4.6: Capacitance values extracted from impedance fits for all data sets. A) Absolute capacitance plotted as a function of the boron nitride thickness, t, with area held constant at $\mathcal{A}$ = 1 mm². B) Absolute capacitance plotted as a function of area, $\mathcal{A}$, with thickness held constant at t = 4.15 μm. C) Absolute capacitance plotted as a function of the area-to-thickness ratio, $\mathcal{A}/t$. D) Relative permittivity of individual capacitors plotted versus $\mathcal{A}/t$.

according to Eq. 4.3 and Eq. 4.4.

Figures 4.6A–C show the expected capacitive scaling expected for pinhole-free dielectric layers. Figure 4.6A shows data with the overlap area fixed at 1 mm² and the dielectric thickness varied from 1.6–4.15 μm. The critical thickness below which a DC current flows through the circuit was experimentally found to be 1.65 μm. This is quite thick considering the percolation threshold for nanosheet networks is typically less than 100 nm and some reasons for this will be discussed below in light of recent publications. Figure 4.6B shows the absolute capacitance

for device with a constant dielectric thickness of 4.15 μm and the overlap area varied from 0.5–2.5 mm^2. The linear relationship here shows excellent agreement with Eq. 4.5. Figure 4.6C shows the capacitance of each of the devices plotted against their area-to-thickness ratio, again consistent with Eq 4.5. From the slope of these data, an average dielectric constant of 1.63 is extracted, in reasonable agreement with the low frequency data presented in Figure 4.6C. The value of 1.63 here does not account for the porosity of the network; through subsequent work covered in Chapter 5, a sprayed BN network has a porosity of 60% which implies a BN dielectric constant of 2.6. This value is consistent with the reported value of 3 ± 1 for the out-of-plane permittivity of h-BN.[205] The relative permittivity for each capacitor is plotted against A/t in Figure 4.6D and the low scatter here suggests the method is reproducible.

4.3 Conclusions

In conclusion, this work demonstrates that graphene/boron nitride capacitive heterostructures with a pinhole-free dielectric layer can be created using a combination of inkjet printing and spray coating techniques. The capacitor functionality means that pinhole-free BN networks were created for thicknesses above 1.65 μm, where the devices show an areal capacitance ranging from 0.24 to 1.1 nF cm^{-2}. This work represents an important step towards realising all-printed heterostructures from solution-processed 2D materials and, in particular, towards a transistor composed solely of nanosheet networks.

4.4 Coda

While it would have been procedurally beneficial to deposit both conductive and dielectric layers through inkjet printing, the use of two deposition techniques provided an excellent opportunity to build experience on both tools. This was complimented by the trial-and-error aspect of this study as the limits of printable inks had to be discovered. Device prototyping is a laborious task as one goes from bulk powder to printed device, however, this study served as a useful stepping stone for the work in the next chapter as the learning curve for these tools was addressed here.

Regarding the printed devices, it may have been prudent to include a polymeric binder to create a more robust dielectric layer as this should, in principle, prevent nanosheet redispersion, thereby creating thinner pinhole-free films. The ink additives would also have allowed the entire device to be inkjet printed however, in light of some recent publications, the inclusion of a binder may not have brought the desired thickness benefits. In Oct 2017, Carey *et al.* published a study on fully inkjet-printed graphene transistors.[107] As these devices are electrostatically gated, it was critical to use the thinnest possible dielectric layer. They fabricated the BN ink with a polymeric additive (carboxymethyl cellulose) and, through capacitor testing, could scale the dielectric layer down to 1.2 μm before the onset of shorting. They also used a colloidal silver ink as the capacitor electrodes which, post-sintering, should have a low surface roughness and near-zero interfacial redispersion with the BN ink.

This minimum thickness is quite close to the value found in this work despite their inclusion of a binder and more precise deposition which may point to an as-yet unknown

issue with BN itself. This idea can be further substantiated through the work of McManus *et al.* where, in 2017, they demonstrated fully inkjet-printed, vertical photodetectors composed of graphene and WS_2.[65] Here, they achieved pinhole-free WS_2 films on the scale of hundreds of nanometres with the aid of a xanthan gum binder. The order of magnitude discrepancy between the two materials is clearly something that requires attention as BN is frequently used as the prototypical dielectric. Any underlying issues should therefore be quickly addressed for the benefit of the community.

Is there any knowledge in the world which is so certain that no reasonable man could doubt it?

Bertrand Russell

5

Current Modulation in 2D Networks

An important milestone for 2D-crystal-based printed electronics is the demonstration of current modulation in a semiconducting network. Many of the impressive 2D transistor benchmarks have been achieved using individual monolayers and this has ignited interest in harnessing these properties for cheap, high performance electronics.[16,27,190] As devices based on discrete monolayers are beyond the

realm of printing expertise, device fabrication is currently based on networks of nanosheets. Such networks have antecedents in carbon nanotubes and inorganic nanoparticles, and transistors based on such materials have demonstrated mobilities and on:off ratios of > 10 $cm^2\ V^{-1}\ s^{-1}$ and > 10^6, respectively. However, these materials may incur the problems of integration and scalability as outlined in Section 3.4.

It is believed that fabricating transistors from printed nanosheet networks will yield several advantages over other nanomaterials. Nanosheets can be conducting (e.g., graphene or MXenes), semiconducting (e.g., transition metal chalcogenides or phosphorene), or insulating (e.g., boron nitride or silicates), and thus the nanosheet family includes all of the electronic building blocks.[68] A wide variety of nanosheet inks can be produced at high volume and low cost through liquid-phase exfoliation which can then easily be printed into networks.[65] Many of the conducting and semiconducting nanosheets have high intrinsic mobilities and although these values are curtailed when the nanosheets are formed into a network, this limitation should be addressable *via* junction engineering.[206] Nanosheet-based inks could thus be used to print both in-plane[187] and stacked[68] nanosheet heterostructures consisting of conducting, semiconducting, and insulating regions corresponding to electrodes, channel, and dielectric, respectively.

This chapter will present a fully printed nanosheet-network thin-film transistor (TFT) but there are several steps which need to be taken before this can be demonstrated. First, the electrical characteristics of such networks need to be investigated. This is conducted by using an ionic liquid to electrolytically gate networks composed of four of the most common semiconducting TMDs (MoS_2, $MoSe_2$, WS_2, and WSe_2). The behaviour of these networks is then evaluated through the output and transfer curves. Second, the use of an

ionic liquid means a method needs to be developed for integrating a liquid into a solid device. This is achieved by using another nanosheet network, dielectric BN, to act as an electrochemical separator between the gate and the channel, where the ionic liquid is contained within the pores of the film. The viability of this structure is assessed through its effect on the device switching speed and this performance is then compared to a device where the ionic liquid is bound in a polymeric matrix. Finally, a fully printed proof-of-concept transistor is demonstrated by integrating the knowledge from these preliminary steps with the techniques developed in the previous chapter.

5.1 Experimental Procedure

The inks were obtained by sonicating pristine powders (WSe_2 [Alfa Aesar], WS_2 [Sigma Aldrich], MoS_2 [Sigma Aldrich] and $MoSe_2$ [Alfa Aesar]) in NMP. An initial concentration of 50 g L^{-1} was processed for 1 hour in 80 mL of NMP using a horn tip sonicator (Sonics Vibra-cell VCX-750 ultrasonic processor) operating at 60% amplitude. The dispersion was then centrifuged at 3218 g for 1 h using a Hettich Mickro 220R, after which the supernatant was discarded to remove potential contaminants from the starting powder.[207] The sediment was then redispersed in fresh NMP and sonicated under the same conditions for 5 h. This gives a polydisperse stock dispersion from which the nanosheets can be size-selected by centrifugation.

For each material, the polydisperse stock was first centrifuged at 26 g for 2 h to remove the largest aggregates with the sediment retained for future resonication. The supernatant was then centrifuged at 106 g for 2 h to separate the smallest nanosheets into the supernatant which was then discarded and the sediment retained. This sediment was redispersed in 60

mL of isopropanol (IPA) to give a stable ink. IPA was chosen as a non-toxic, low boiling-point solvent making it more suitable for spray deposition. The greatest stability for such IPA-based dispersions was observed for concentrations < 0.8 g L^{-1}.

UV-Vis optical spectroscopy was performed using a Perkin Elmer 1050 spectrometer equipped with an integrating sphere (150 mm). The samples were diluted to a suitable optical density and measured using a quartz cuvette with an optical path length of 4 mm. Each sample's absorbance spectra were measured by placing the cuvette in the centre of the integrating sphere.

The ionic liquid was 1-ethyl-3-methylimidazolium bis(trifluoromethylsulfonyl)imide (EMIm TFSI) and was bought from Sigma Aldrich. The as-bought liquid was dried in a vacuum oven ($\sim 10^{-1}$ mbar) for 24 h at 70 °C. The dried liquid was then stored in a glovebox to minimise water uptake. A block copolymer poly(vinylidene fluoride co-hexafluoropropylene), P(VDF- HFP), was used to form the gel for use as a solid electrolyte. The ionic gel was made in a ratio of polymer:ionic liquid:acetone of 1:5:15 and spin-coated onto the samples at 2000 rpm for 30 s. The excess gel was then removed with a toothpick.

The devices for investigating the current modulation were prepared by spray coating the active materials (WS_2, WSe_2, MoS_2, and $MoSe_2$) onto Al_2O_3-coated PET [Mitsubishi Paper Mills] using a shadow mask (1×3 mm^2). The spray deposition was performed as outlined in the previous chapter. A pair of 100 nm thick gold interdigitated electrodes (IDE) were deposited onto the channel through a shadow mask using a Temescal FC2000 metal evaporation system. The IDE channel length, L, was 120 μm and width, w, was 16 mm, giving $L/w = 0.0075$. The channel thickness was measured with a mechanical

profilometer.

The density of each film was obtained using a mass balance. A film was sprayed using the inks described above onto glass substrates of known mass which were then reweighed to give the mass of each film. The thickness was measured using mechanical profilometry and the area was measured through photo analysis using ImageJ software. The mass per unit volume for the film was then compared to known bulk values to estimate porosity.

The electrical measurements were performed using a Keithley 2612A in a Janis probe station under high vacuum ($\sim 10^{-5}$ mbar). This is to prevent water uptake in the ionic liquid which would reduce the electrochemical window.[143] The samples were heated to 70 °C for 12 h under high vacuum to remove any water which may have been absorbed while placing the device into the chamber.

The electrochemical measurements were performed on a CH Instruments 600E Series Electrochemical Analyzer/Workstation. A three electrode cell with an Ag/AgCl reference electrode was used with a platinum counter electrode. The working electrode was produced by spraying the TMD material onto ITO-coated glass. Each electrode was submerged in the ionic liquid and measurements were performed in a small voltage window under ambient conditions.

Atomic force microscopy (AFM) was carried out on a Dimension ICON3 scanning probe microscope (Bruker AXS S.A.S.) in tapping mode under ambient conditions using aluminium-coated silicon cantilevers (OTESP-R3). Typical image sizes were $10 \times 10\ \mu m^2$ at scan rates of 0.5 Hz with 1024 lines per image. The apparent thickness was converted to number of layers using previously developed step-height analysis of liquid-exfoliated TMDs.[198,199]

Bright-field transmission electron microscopy (TEM) was performed using a JOEL 2100 operated at 200 kV. Samples were diluted to a low concentration and drop cast onto a continuous carbon film TEM grid purchased from Agar Scientific. The TEM grid was placed on a filter membrane to wick away excess solvent and dried overnight at 150 °C in a vacuum oven. Statistical analysis was performed on the nanosheets dimensions by measuring the longest axis and defining it as the nanosheet length.

Raman spectroscopy was performed on deposited dispersions and bulk powders using a Renishaw InVia microscope with 532 nm excitation laser in air under ambient conditions. To sample a larger area of the film, the Raman emission was collected by a 20x objective lens in streamline mode and dispersed by a 2400 l/mm grating at 1% of the laser power (~ 0.2 mW). The laser power was kept as low as possible to avoid sample decomposition and heating. Measurements on a minimum of five different spots were performed and showed the samples to be highly homogeneous under these measurement conditions. The spectra were baseline-corrected and averaged after acquisition.

5.2 Results and Discussion

5.2.1 Material Analysis

The inks used in this work are shown in Figure 5.1A and representative TEM images of each ink's constituents are shown in Figures 5.1B–E. The dark colour of each ink is indicative of the bulk-like properties of the nanosheets. The TEM imagery confirmed that each dispersion was composed of two-dimensional nanosheets and a statistical analysis was performed on these images to extract the average nanosheet length for each of the inks (100 counts per ink). This provided the following average nanosheet lengths; MoS_2, 320 nm; WS_2, 317 nm; $MoSe_2$, 376

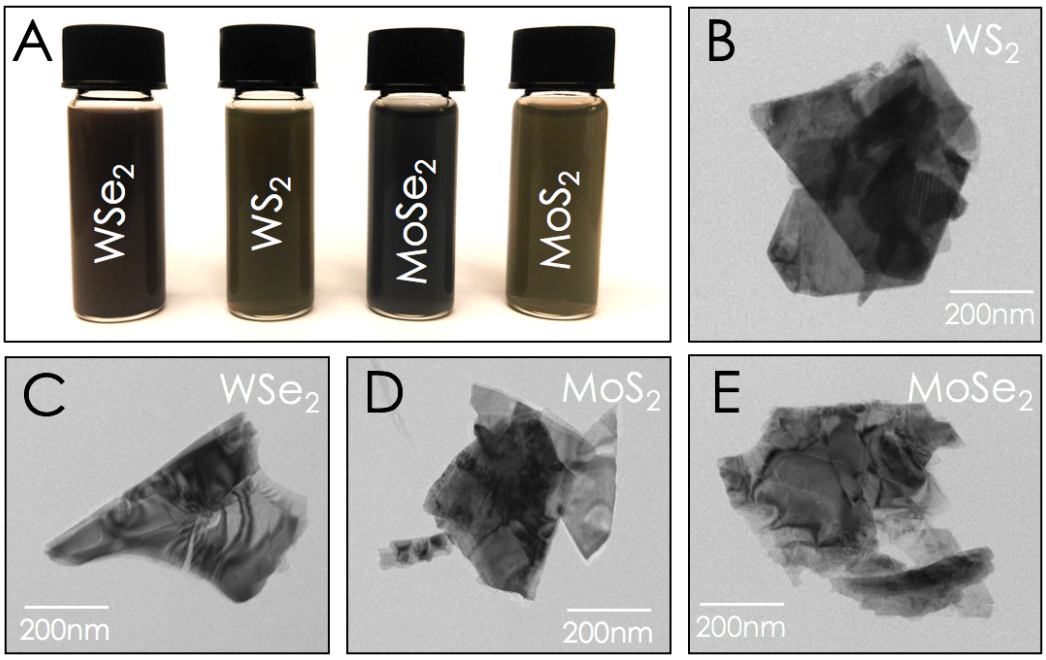

Figure 5.1: TMD inks. A) Photograph of the each of the TMD inks. Representative TEM images of B) WS_2, c) WSe_2, D) MoS_2, and E) $MoSe_2$ nanosheets.

nm; and WSe_2, 309 nm.

Each of the TMDs used in this study are semiconducting meaning their bandgaps can be confirmed through optical absorption spectra. Figure 5.2A shows such absorption spectra for each ink (measured with an integrating sphere to remove scattering) and confirmed that all materials were indeed semiconductors, with optical gaps between 1.5 and 1.9 eV. These values are consistent with reporting on the the bulk bandgaps for these materials when produced in this manner.[204] As a dispersion produced through LPE will always contain a distribution of nanosheet thicknesses, there is also a corresponding distribution in bandgap—first pointed out by Mak *et al.*[21] They showed that transition metal dichalcogenide nanosheets, such as MoS_2, have bandgaps which rise as the crystal is

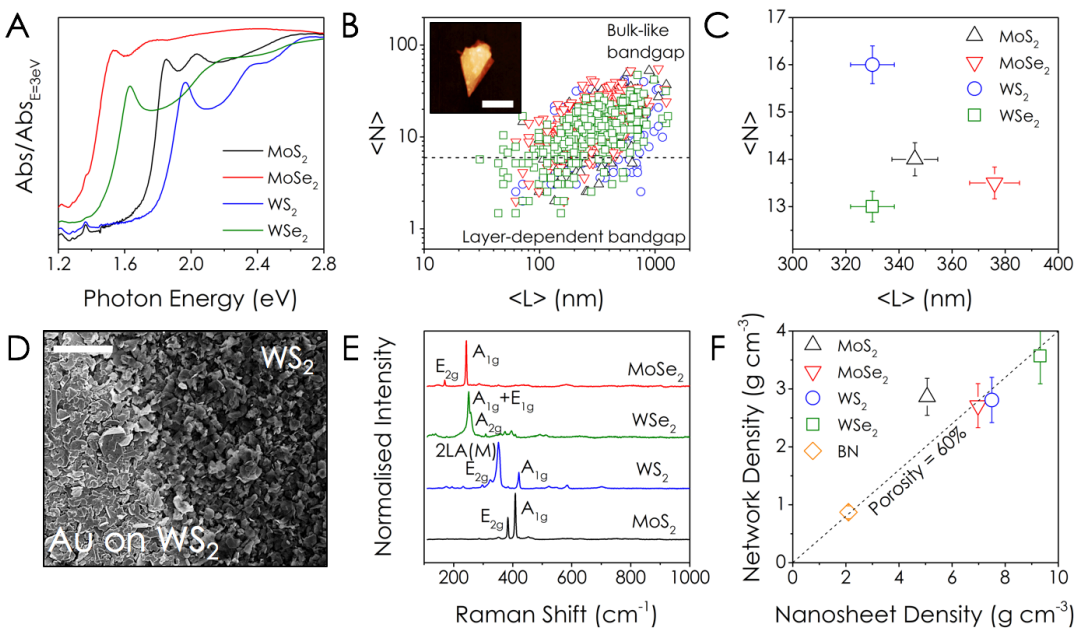

Figure 5.2: TMD material analysis. A) Optical absorption spectra for each material extracted using an integrating sphere to remove the scattering component of the extinction. B) AFM analysis of the aspect ratios the nanosheets in each ink. > 85% of the nanosheets are above 6 layers meaning the band structures are bulk-like. An example WSe_2 nanosheet is shown inset with a 200 nm scale bar. C) The average nanosheet dimensions for each material extracted from AFM analysis. Error bars are standard deviation. D) An SEM image of a WS_2 network with a gold electrode deposited on top. The scale bar is 1 µm. E) Raman spectra for each material, performed on films such as that shown in D). F) The density of the network against the density of the nanosheets, revealing ~ 60% of each film is free volume. Error bars are standard deviation.

exfoliated down to the monolayer—as discussed in Chapter 2. This is problematic as *any* as-produced ink will have such a distribution of nanosheet thicknesses, leading to a spatial distribution of local bandgaps in any resultant films. This could result in carrier trapping or other factors that result in a reduction in device performance and poor reproducibility across networks. To address this, liquid cascade centrifugation was used to screen out not just the large unexfoliated particles but also the smaller, thinner nanosheets that exhibit layer-dependent characteristics.[208] This method is a stop-gap solution that should eliminate the bandgap variance in nanosheet networks until such time as a fully monodisperse ink can

be created. This was confirmed through AFM analysis, as shown in Figure 5.2B. Here, a statistical survey showed that > 85% of the nanosheets had $N > 5$ layers and therefore have a bulk-like electronic structure.[21] For each material, the mean nanosheet lengths were in the range of 330–380 nm with thicknesses in the range of 13–17 layers, as shown in Figure 5.2C.

Figure 5.2D shows an SEM image of a typical nanosheet network (here, WS_2) with a gold top-contact. This image demonstrates the benefit of a top-contact configuration as the rough surface of the films can interface more intimately with a contact that follows the topography. This image also shows that the deposited films show considerable local disorder—despite uniformity over millimetre length scales—with a significant pore volume. The latter is a signature of spray-coated nanosheet networks and capitalising on this will be described later. Raman spectroscopy was performed on such networks for each semiconductor with the results shown in Figure 5.2E. The spectra present as expected with the peaks showing no signs of oxidation or defects in the deposited material. Figure 5.2F demonstrates the considerable porosity of the sprayed networks. As each film lies on a line of continuous porosity (with the exception of MoS_2) regardless of material constituent, the large value of 60% can be attributed to the deposition method. There are currently no reports quantifying (or even commenting on) the role of deposition in the morphology of nanosheet networks but it is likely that more precise methods such as inkjet printing would create films with better nanosheet alignment and hence a lower porosity. However, this need not be a disadvantage for sprayed networks as the high porosity can be utilised for electrolytic gating.

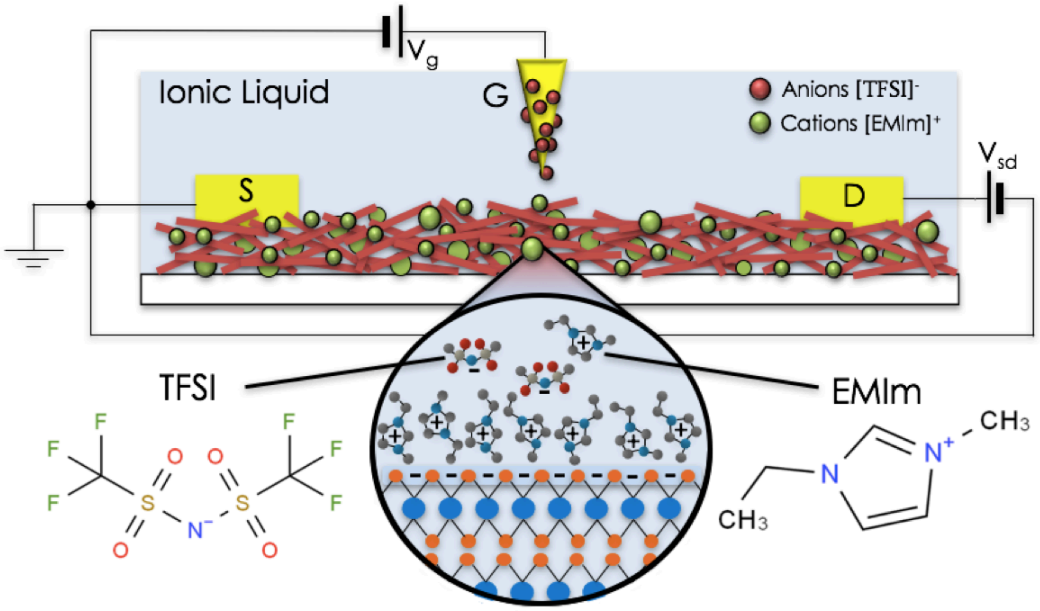

Figure 5.3: TFT schematic. The nanosheet network has gold source and drain electrodes evaporated on top of the film. The ionic liquid droplet is placed on top of the device and a probe penetrates the top of the droplet to provide the gate. Under a gate bias, the EMIm and TFSI ions in the ionic liquid form a double layer on the gate probe and on the basal plane of the nanosheet (shown enlarged). This draws carriers from the external circuit to balance the ion accumulation.

5.2.2 Electrical Characterisation

Field-effect transistors fabricated from carbon nanotube networks have been well reported since the material's discovery in the 90s but, to date, attempts to produce such transistors from semiconducting nanosheet networks have been unsuccessful. The efforts typically employ electrostatic gating which has resulted in poor switching, likely a result of electrostatic screening by the nanosheet structure. Here, the inherent porosity of the nanosheet networks can be exploited to fabricate electrolytically-gated transistors, where the porous free-volume of the network is filled with an electrolyte, as shown in Figure 5.3. In this case, an ionic liquid (IL), EMIm TFSI, is used instead of an aqueous electrolyte as ionic

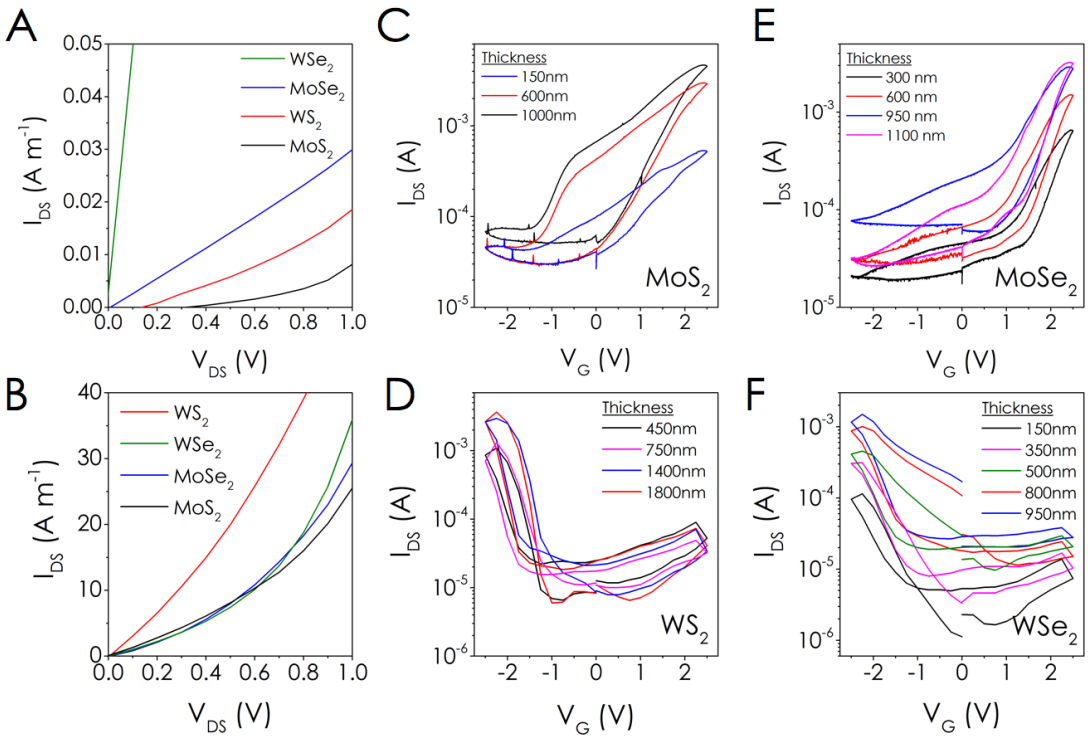

Figure 5.4: Electrical characterisation. A) Output curves for each material with films in the dry state. B) Output curves for each material with films in the wet state. The conductivity increase in attributed to a non-uniform distribution of ions at the basal plane interface. C–F) Semi-logarithmic transfer curves for each material for a range of thicknesses.

liquids have a wider electrochemical window, a high ionic conductivity, and are composed solely of anions and cations which precludes water-based reactions within the device.[143] Under a gate bias, the ions are driven to the ionic liquid/semiconductor interface where the large electric field draws charge carriers from the external circuit to create a double layer, shown expanded in Figure 5.3. The accumulated charge density at the interface can be quite large ($>10^{12}$ cm^{-2}), which results in strong current modulation.[141]

Figures 5.4A and B show output curves for (A), nanosheet networks with no ionic liquid, or "dry" films, and (B), networks with ionic liquid, or "wet" films. In each subfigure, the

current is normalised by the film thickness so the difference in slope is solely a reflection of the difference in conductivity of each material. It is noteworthy that the films free of ionic liquid show linear I-V curves while the films containing ionic liquid do not. The dry film linearity can be attributed to the long device channels (120 μm) as the channel resistance is quite high in the dry state. For devices at this channel length and with a thickness of ~ 500 nm, the resistance ranges from tens of GΩ for MoS_2 to tens of MΩ for WSe_2. This means that the rate-limiting step is charge transport through the device—known as bulk-limited transport—where one would expect the I-V curves to be linear at low voltages.[204]

There are two possible reasons for the non-linearity appearing in the output curves upon addition of the ionic liquid. First, doping by the ionic liquid would cause the wet conductivity to be significantly larger than that of the dry networks. This would reduce the resistance of the channel and may introduce some non-linearities due to an alteration in carrier injection. However, as both ions are present throughout the network at $V_G = 0$ V, the application of a drain-source bias may affect the arrangement at the nanosheet interfaces. This ionic liquid-induced doping is then a consequence of an imbalance of positive and negative ions on the nanosheet basal planes. For example, an excess of positive ions at the interface would lead to a local accumulation of electrons in the conduction band of the nanosheets. As the accumulated charge density is relatively low at $V_G = 0$ V, this implies a modest charge imbalance and could simply arise from differences in binding energy between cations and anions at the nanosheet surface.

Figures 5.4C–F show semi-logarithmic transfer curves for each material and for a range of thicknesses. These transfer curves were measured at 20 mV s^{-1} and, in each case, current modulation was observed with both n- and p-type behaviour appearing to depend on the

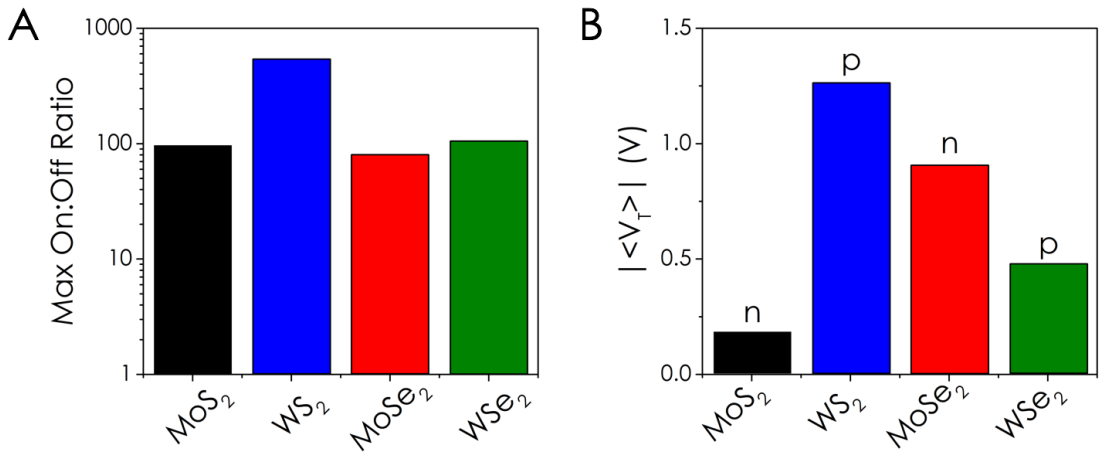

Figure 5.5: On:off ratios and threshold voltages. A) The maximum on:off ratio measured for each material. These values are limited by large off-currents which may be attributed to the ion distribution. B) The (absolute) threshold voltages for each material.

transition metal. Of particular importance here is the similarity in curve-shape across thicknesses which demonstrates that thick networks can be switched as effectively as thin ones. This means the ionic liquid can access all parts of the network for thicknesses up to 1.8 μm, for sprayed networks at least. Furthermore, the devices are capable of driving currents of several milliAmps for each material, despite the long channel length. The transfer curves show hysteresis in every device and, although this is common in electrolytically-gated nanosheet transistors,[141] the exact mechanism for this is still unknown. Some reports suggest that hysteresis is strongly dependent on the scan rate[209] but this is contradicted by a new report (in submission) suggesting it is independent of scan rate. In either case, there appears to be consensus that trap states are a significant contributor to the hysteresis[210] and, in the systems presented here, this is likely imparted by solvent residues from the LPE process.[204] Figures 5.5A and B show the values of the maximum on:off ratio and the average threshold voltage for each material, extracted from Figure 5.4. The on:off ratios were

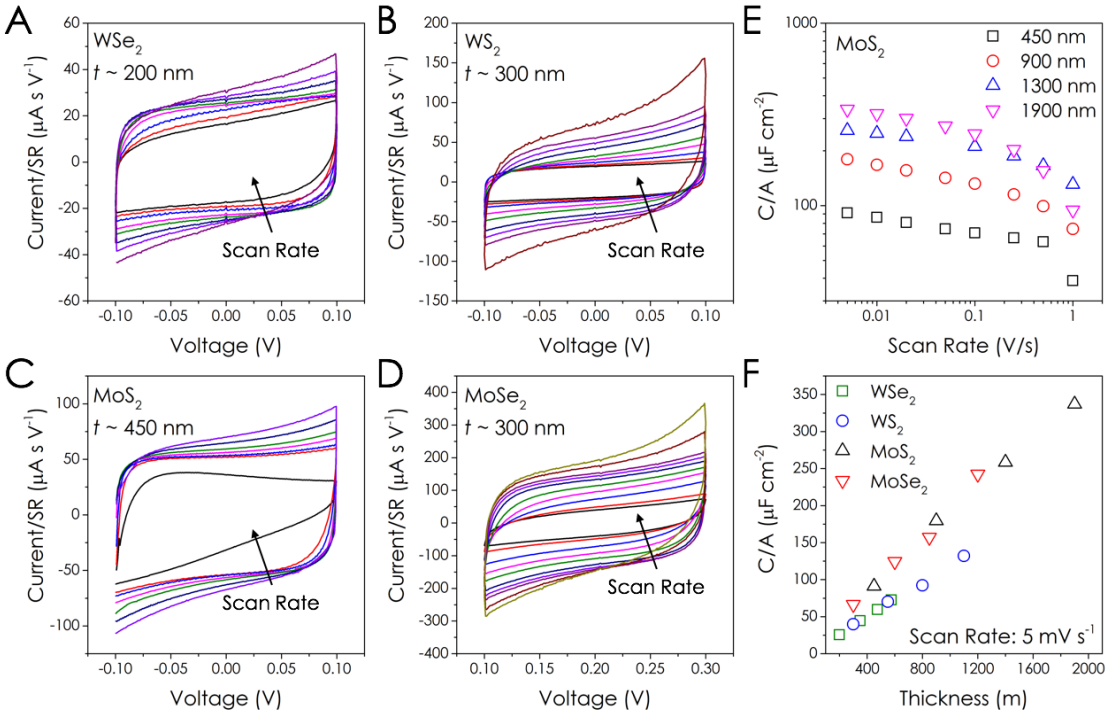

Figure 5.6: Electrochemical analysis. Representative cyclic voltammetry at a given thickness for A) WSe_2, B) WS_2, C) MoS_2, and D) $MoSe_2$. E) Areal capacitance extracted from (A)–(D) plotted against scan rate. F) Areal capacitance at a given scan rate from (E) plotted against film thickness. The slope of these data is the volumetric capacitance.

limited by high off-currents (Figure 5.4) because of the aforementioned doping associated with the ionic liquid, so it will be critical to address this in future work. The threshold voltages varied between -1.3 and +1.0 V, depending on the material.

5.2.3 Electrochemical Characterisation

Before the scaling effects and mobility can be extracted from the data in Figure 5.4, it is first necessary to determine the volumetric capacitance. While traditional transistors rely on the areal capacitance of the insulator interface, the current in these nanosheet networks flows in three dimensions. The volumetric capacitance has long been used when gating organic

electrochemical TFTs but its value is (generally) independent of the film's constituents.[141] This is where nanosheet networks have demonstrated another key strength; the electronic characteristics of a network are strongly influenced by the geometry of the nanosheets contained within.[211] This is useful for electrochemical applications that scale as the number of active edge sites but it is also important for these TFTs as the volumetric capacitance can be tuned *via* control of the nanosheet aspect ratio.[211]

The capacitance of these devices was investigated using cyclic voltammetry. Figures 5.6A–D show the representative sweeps for each material at a given thickness. These traces correspond to a range of voltage sweep rates and take place in a narrow window where the traces are reasonably box-like. This constant current flow represents the bandgap region where the occurrence of Faradaic reactions is minimised, meaning the extracted capacitance can be considered the non-Faradaic double-layer capacitance.[211] In each case, the area under the curve corresponds to the capacitance through

$$C_A = \frac{1}{\mathcal{A}(dV/dt)} \int_{-0.1}^{0.1} I dV \tag{5.1}$$

where C_A is the areal capacitance, dV/dt is the scan rate, and the integral limits are those used in Figure 5.6C. Integrating each sweep provides the areal capacitance for that scan rate, with representative MoS_2 data shown in Figure 5.6E. Here, the decreasing areal capacitance with increasing scan rate is understood through through Eq. 5.1. Figure 5.6F then shows the plot of how the areal capacitance evolves with film thickness for a fixed scan rate. The linearity for each material means the slope is equal to the volumetric capacitance, according to $C_A = C_V \times t$. This provided values in the range of 1.2–2.1 F cm^{-3}, which can be considered the maximum volumetric capacitance achievable for networks with this

nanosheet dimensionality. While the volumetric capacitance may be constant with film thickness, it can be still be tuned to an arbitrary value through scaling of the nanosheet dimensions.

5.2.4 Transport Characterisation

A deeper analysis of the data in Figure 5.4 is possible now that the network capacitance is known. The transfer curves in Figures 5.4C–F show current scaling with thickness and this can be quantified through the rate-of-change of current with gate voltage, or transconductance. A thickness dependence is not typically seen in TFTs as electrostatic gating confines the field effect to a thin layer at the insulator interface. This is reflected by the areal capacitance term in the expression for transconductance (derived in Appendix B.1) as

$$g_m \equiv \left.\frac{\partial I_{DS}}{\partial V_G}\right|_{V_{DS}} = \frac{w}{L}\mu_{Net} C_A V_{DS} \tag{B.16}$$

where μ_{Net} is the network mobility, and the other symbols have their usual meaning. The volumetric behaviour in electrolytically-gated networks is revealed by transforming Eq. B.16 using $C_A = C_V \times t$ such that

$$g_m \equiv \left.\frac{\partial I_{DS}}{\partial V_G}\right|_{V_{DS}} = (\frac{w}{L}\mu_{Net} C_V V_{DS}) \times t \tag{5.2}$$

where the transconductance now scales linearly with thickness. This is a useful degree of freedom for transistors as the performance can now be tuned without altering the device footprint. A high transconductance is essential for transistor applications such as sensors,

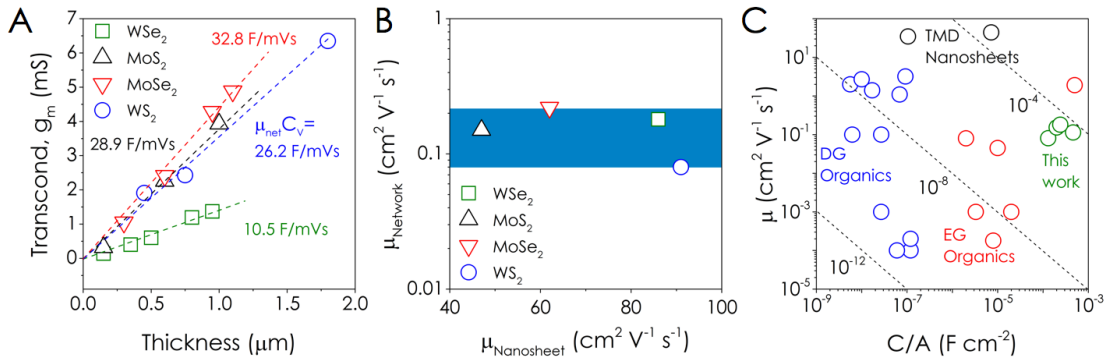

Figure 5.7: Transport analysis. A) The transconductance extracted from Figure 5.4 plotted against thickness. The product $\mu_{Net}C_V$ is a figure of merit for this type of transistor. B) The network mobility as a function of nanosheet mobility measured by terahertz spectroscopy. The blue band indicates the upper limit on mobility due to junction resistance. C) The mobility against areal capacitance for various materials and gating mechanisms (DG, dielectrically gated; EG, electrolytically gated). The contours represent constant $\mu_{Net}C_A$ where the best performing devices lie at the top right.

for example, where the efficiency of converting a small signal into a large output determines the sensitivity.[212] Achieving a high gain was a challenge for organic TFTs but recent efforts have realised well-performing devices, with transconductances on the order of several milliSiemens.[213] The relationship described by Eq. 5.2 is demonstrated for nanosheet networks in Figure 5.7A, with linearity shown for each material. The highest transconductance measured for these devices is ~ 6 mS, which is remarkable as these networks are wholly unoptimised. This means that the transconductance, and hence the drive current, is tunable over a range competitive with state-of-the-art organics through a facile variation of the network (thickness) and nanosheet (volumetric capacitance) characteristics. Additionally, Eq. 5.2 implies that the product $\mu_{Net}C_V$, which can be extracted from the g_m versus t data, is a figure of merit for such networks.

Combining the measured C_V values from Figure 5.6 with the $\mu_{Net}C_V$ data above yields network mobilities between 0.08 and 0.22 cm^2 V^{-1} s^{-1}. Despite the modest magnitude,

these values are much larger than those of early undoped conjugated polymers[214] and are competitive with many recent organic TFTs.[215] Although the network mobilities can be limited by relatively slow charge transfer from one nanosheet to another and/or charge injection to the electrodes, the mobility of charges moving within a nanosheet is much higher.[18] The intrasheet mobility for these systems was determined by collaborators who used time-resolved optical-pump terahertz-probe (OPTP) measurements through methods described previously.[216,217] This provided nanosheet mobilities in the range 47–91 $cm^2\ V^{-1}\ s^{-1}$—over three orders of magnitude higher than the network values. This strongly indicates that intersheet transport is the limiting factor for electrical transport in these devices. Figure 5.7B shows a plot of the network mobility, $\mu_{Network}$, against the nanosheet mobility, $\mu_{Nanosheet}$, and on such a plot, the highest performing networks should lie in the upper right quadrant. However, the junction resistance caps the network mobility in the range indicated by the blue band meaning that, for these systems, the overall network mobility is completely dominated by the intersheet resistance. Such behaviour is generally understood through Matthiessen's rule where

$$\frac{1}{\mu_{Network}} = \frac{1}{\mu_{Intersheet}} + \frac{1}{\mu_{Intrasheet}} \tag{5.3}$$

As the smaller mobility will govern the global behaviour, these data provide a guideline for formulating strategies to improve the characteristics of the networks. In particular, the three-order-of-magnitude difference in mobility means it is much more prudent to focus on intersheet improvements before effecting improvements to the individual nanosheets—for these printed applications at least.

These nanosheet-network TFTs can be benchmarked with other reported TFTs by

		Layered Crystal			
		MoS_2	WS_2	$MoSe_2$	WSe_2
<Length> [nm]	TEM	320	317	376	309
	AFM	346	330	376	330
<Thickness> [Layers]	AFM	14	16	13.5	13
Bandgap [eV]		1.85	1.96	1.55	1.64
Porosity [%]		44	62	61	62
Conductivity [S m^{-1}]	Dry	5.0×10^{-6}	9.4×10^{-5}	1.2×10^{-4}	3.8×10^{-3}
	Wet	0.10	0.26	0.09	0.19
Carrier Density [cm^{-3}]	Dry	2.1×10^{12}	2.6×10^{14}	2.9×10^{15}	4.2×10^{13}
	Wet	4.1×10^{16}	7.0×10^{16}	7.0×10^{16}	6.6×10^{16}
Charges per nanosheet [μm^{-2}]		1700	5800	7800	2700
Mobility [$cm^2 V^{-1} s^{-1}$]	Nanosheet	47	62	86	91
	Network	0.15	0.22	0.18	0.08
|Threshold Voltage| (V)		0.18	1.26	1.08	0.55
Max On:Off Ratio		98	615	114	88
Volumetric Capacitance ($F cm^{-3}$)		1.9	1.2	1.8	1.3
$\mu_{Net}C_V$ ($F m^{-1} V^{-1} s^{-1}$)		28.9	26.2	32.8	10.5

Figure 5.8: Summary of TMD network characteristics.

comparing the product $\mu_{Net}C_A$, as shown in Figure 5.7C. Here, the best-performing TFTs are in the upper right, with the dashed lines representing constant contours of $\mu_{Net}C_A$. By this measure, the thickest nanosheet-network TFTs are competitive with benchmark TFTs as their high values of C_A compensate for the relatively low network mobilities. In sum, the various properties extracted for these networks are tabulated in Figure 5.8.

5.2.5 Temporal Behaviour

There has been much engineering done to incorporate ionic liquids or electrolytes into solid organic devices. The integration of a liquid has typically been achieved through a gel where the ionic liquid is suspended in a polymer matrix. This naturally has a deleterious effect on the ionic mobility and the switching speeds in gel-based devices tend to be slow.[141,218] This is where the porosity of nanosheet networks holds another advantage as the liquid can be contained within the pores of an insulating nanosheet network and, for large pore volumes, the ions should be free to move relatively unhindered. This would allow solid devices to utilise the high conductivities of the ionic liquids without the reduction associated with an ionic gel.

This effect can be explored through the RC time constant corresponding to the formation of the electric double-layer. Figure 5.9A shows a schematic of a WSe_2 TFT gated with an unadulterated ionic liquid and Figure 5.9B shows its temporal response to a square-wave signal to the gate ($V_{G,On} = -2.5$V and $V_{G,Off} = 0$V). The time constant is extracted from fitting the exponential rise of the current and is given by $\tau = R_{ESR}C$, where R_{ESR} is the series combination of the network and ionic liquid resistances and C is the capacitance of the network. From Higgins *et al.*,[219] the time constant for a nanosheet

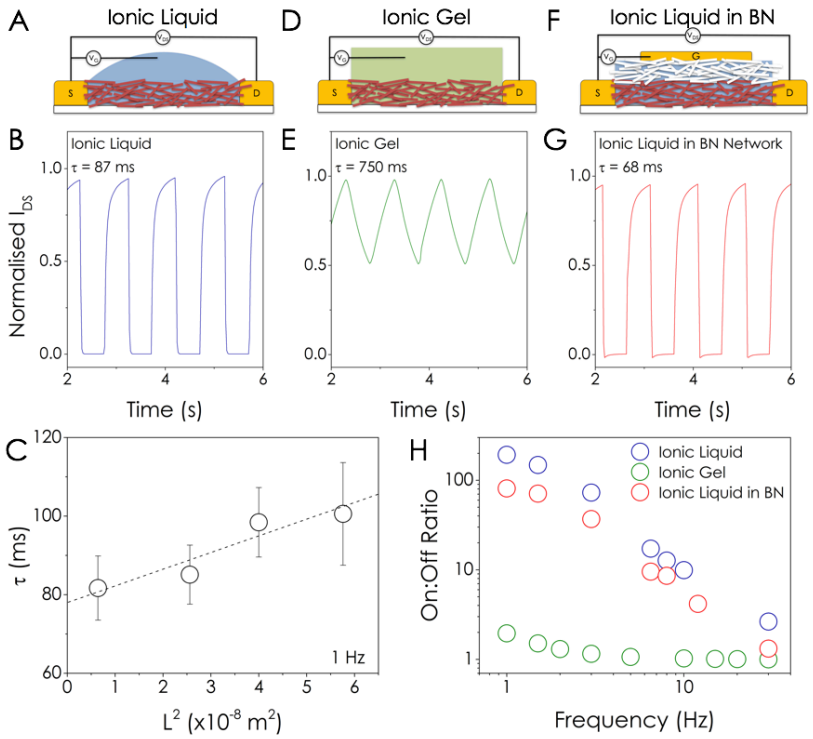

Figure 5.9: Temporal response for various configurations. A) A schematic of a TFT with a purely liquid gate. B) The current response of (A) to a square wave gate signal at 1 Hz. C) The time constant extracted from (B) plotted against L^2 according to Eq. 5.5. D) A schematic of a TFT gated with a solid polymer electrolyte. E) The current response of (D) to a square wave voltage signal at 1 Hz. The device cannot fully switch off within one period of the gate signal. F) A schematic of a TFT with a BN network used to contain the IL. G) The current response of (F) to a square wave gate signal at 1 Hz. The behaviour is almost identical to that of the purely-IL device. H) The on:off ratio as a function of gate voltage frequency.

network can be written as

$$\tau = (R_{Network} + R_{IL})C = \left(R_S \frac{L}{W} + \frac{1}{G_A LW}\right) C_A LW = C_A R_s L^2 + \frac{C_A}{G_A} \qquad (5.4)$$

where R_S is the sheet resistance, G_A is the conductance of the ionic liquid per unit area, and the other symbols have their usual meaning. By noting that $C_A = C_V t$, $R_S = (\sigma_{wet} t)^{-1}$, and $G_A = \sigma_{IL}/d$ where d is the length-scale associated with ionic transport, Eq. 5.4 can be

restated to include only intrinsic and dimensional parameters as

$$\tau = \frac{C_V}{\sigma_{wet}} L^2 + \frac{C_V d}{\sigma_{IL}} t \tag{5.5}$$

The terms in this expression are divided into both electronic and ionic transport and also into the length and thickness dependence. The validity of this model was tested by varying the channel length from 80–240 μm and, as shown in Figure 5.9C, the time constant was found to vary from 75–100 ms. These data are consistent with Eq. 5.5 implying that the switching speed of these devices is limited by ion transport. This also means that this equation can be used to develop strategies for reducing τ. It is easy to see that the switching time will be decreased through reductions in C_V, L, t and d. In addition, it is clearly necessary to maximize σ_{wet} and σ_{IL}, noting that $\sigma_{wet} \propto \mu_{Net}$ so high mobilities remain important. However, it should be noted that reducing C_V and t will reduce g_m and I_{DS} per Eq. 5.2. Thus, one strategy would be to maximize μ_{Net} as much as possible while minimizing L and d which would allow C_V or t to be reduced without sacrificing g_m or I_{DS}. The minimisation of d, the ionic transport length-scale, is commonly achieved through the use of thin solid electrolytes based on polymers or gels.

To test the effect of a polymer matrix on switching speeds, a set of test devices were prepared with an ionic gel for comparison (Figure 5.9D). Figure 5.9E shows the temporal response of such a device where, as expected, the time constant is an order of magnitude slower than that of a liquid-only device (750±70 ms *vs* 87±15 ms). This problem can be resolved by spraying a network of BN nanosheets (porosity 60%, shown in Figure 5.2F) on top of the semiconducting channel, in the manner described in the previous chapter. This structure is schematically shown in Figure 5.9F. The BN network is not deposited as a

traditional dielectric as its function is more analogous to the electrochemical separator in a supercapacitor where ions are free to migrate between the electrodes. A gold gate electrode was then evaporated onto the BN layer to complete the vertical transistor and the ionic liquid was placed on the structure to fill the porous free-volume. This gave a solid-like structure containing the highly mobile ions which allowed recovery of the periodic behaviour and time constant of the liquid-only device (87±15 ms *vs* 68±10 ms), as shown in Figure 5.9G. This is extremely useful as the conductivity of the ionic liquid is not significantly affected through containment within the porous structure of the network.

In each of the above cases, the source-drain current increases exponentially when the gate voltage is switched on before falling again once the gate voltage is switched off. The effective on:off ratio is thus limited by how much the current can change within one period of the square wave. One would expect the on:off ratio to be maximised when the period of the gate voltage signal, τ_G, is much greater than the switching time, τ_{RC}, so complete switching occurs once $\tau_{RC} \ll \tau_G$. Figure 5.9H shows a comparison between the effective on:off ratios measured at different switching frequencies for a purely-liquid TFT, an IL gel, and an IL contained within the BN network. The on:off ratio is only slightly reduced in the latter system compared to the purely-IL system but performs considerably better than the IL gel. This result again indicates that a dielectric network can be used to contain the ionic liquid with a minimal influence on the electrical and ionic characteristics.

5.2.6 All Printed Thin-Film Transistor

The work presented thus far now permits the demonstration of a fully printed, nanosheet-network, thin-film transistor. Chapter 4 showed that printed vertical layers can be insulated from one another and this chapter has demonstrated that an ionic liquid can effectively gate a nanosheet network. However, it is the BN separator that facilitates the development of the vertical heterostructure as the BN network allows fast diffusion of the ions with minimal structural screening. A schematic of the printed heterostructure is shown in Figure 5.10A. Each component of this device is composed of nanosheet networks, where graphene networks form the electrodes, a WSe_2 network forms the channel, and a BN network forms the separator between the gate and the channel.

This fabrication process is broadly outlined in Figure 5.10B. The inkjet-printed source and drain electrodes have a 200 μm channel length and, although this is quite long, it could be at least halved through further optimisation of the inks, substrate, and deposition.[107] The WSe_2 channel is printed to completely cover the graphene source and drain to provide good contact between the networks. A BN network is then sprayed on top of the channel with a thickness of ~ 8 μm. A large lateral nanosheet length was chosen for the BN ink ($<L> \sim 600$ nm) as a large nanosheet size should confer a large pore size in the network. The structure was then finished by inkjet printing a graphene gate onto the BN. The degassed ionic liquid was then deposited on the structure to fill the free volume of the film.

An SEM image of the interface between the graphene gate and the BN separator is shown in Figure 5.10C. The films appear uniform on the scale of hundreds of microns but a magnified view (Figure 5.10D) shows considerable local disorder and the high surface roughness of the sprayed BN film. Figure 5.10E shows a cross-section of the device. This was

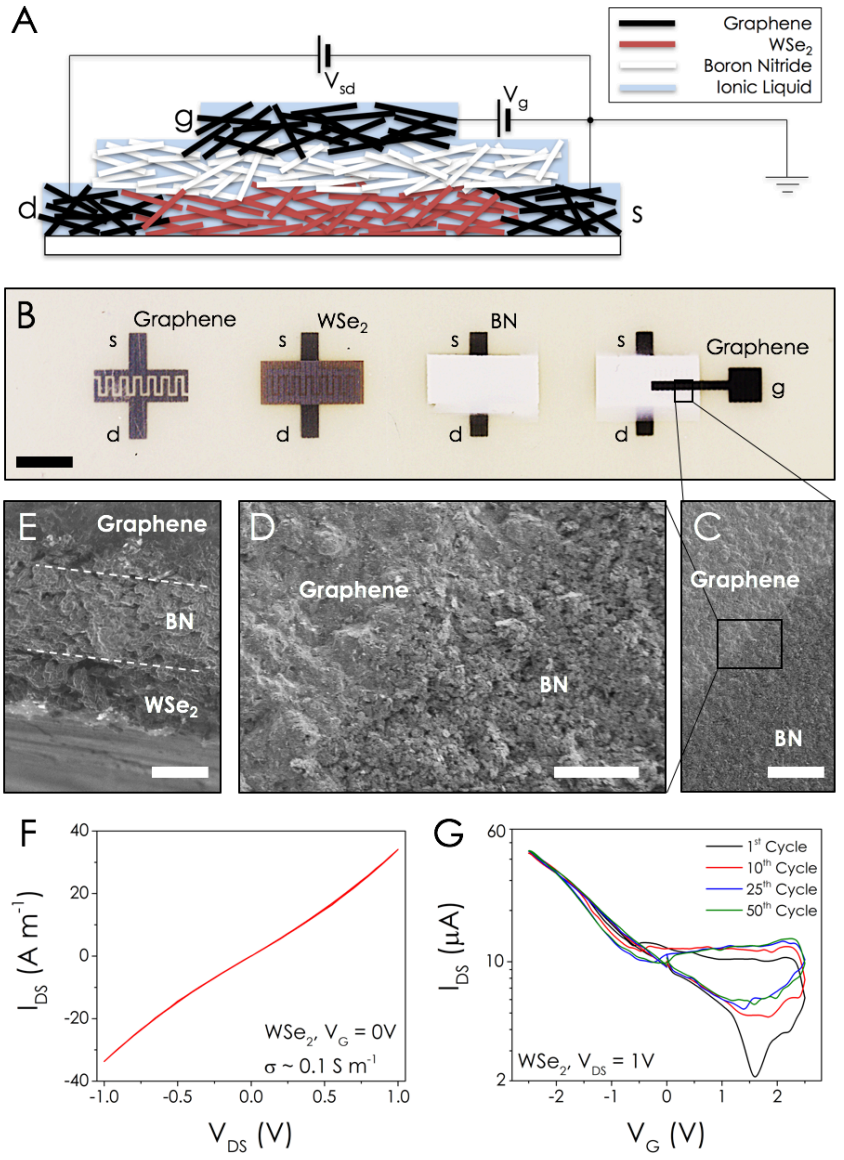

Figure 5.10: A fully printed nanosheet-network transistor A) A schematic of the fully printed TFT with graphene source, drain, and gate electrodes, a WSe_2 channel, and a BN separator. B) Optical image of the printing stages. The source and drain electrodes are inkjet printed, followed by the WSe_2 channel, the BN network is then sprayed, and the gate is finally inkjet printed. The scale bar is 3 mm. C) An SEM image of the indicated area from (B). The scale bar is 100 µm. D) A higher magnification of the transition area in (C), scale bar 10 µm. E) A cross-section of the final structure. The dashed lines roughly divide the WSe_2 channel, the BN separator, and the graphene gate electrode. The scale bar is 5 µm. H) Output curve for the printed TFT at zero gate voltage. The wet conductivity is extracted as 0.1 S m^{-1}. G) Transfer curves for a printed TFT after cycling the gate voltage 1, 10, 25, and 50 times.

prepared by freeze-fracturing a device after cooling with liquid nitrogen. Here, the individual graphene, BN, and WSe_2 nanosheet networks are visible, with the BN appearing more disordered than the graphene and WSe_2, likely a reflection of the difference in printing method.

The output and transfer characteristics are shown in Figures 5.10F and G. The wet conductivity extracted from the thickness-normalised output curve in Figure 5.9A is consistent with that previously measured in Figure 5.4B. This indicates that the doping associated with the ionic liquid (under zero gate bias) has a far greater influence than any effect caused by the workfunction difference between the gold and graphene electrodes (5.1 eV *vs* ~ 4.6 eV). Figure 5.10G shows the transfer curve for 50 cycles, where the device appears to stabilise after the tenth cycle. The hysteresis is also minimised when the device is switched on, which could possibly be attributed to the bottom contact geometry used here. The device shows p-type switching which is again consistent with the WSe_2 transfer characteristics presented in Figure 5.4F. This proof-of-concept transistor performs reasonably well, with an on:off ratio of ~ 25 and a transconductance, g_m, of 22 μS.

5.3 Conclusions

This chapter demonstrates that networks composed solely of nanosheets can be gated using an ionic liquid as an electrolyte. Networks of MoS_2, WS_2, WSe_2, and $MoSe_2$ show mobilities of ~ 0.1 $cm^2\ V^{-1}\ s^{-1}$, and the similarity in quantity indicates that transport in these networks is limited by intersheet junctions. Despite these networks being wholly unoptimised, this value is far higher than the early organic devices, leaving many roads to optimisation. Many of the solid electrochemically- or electrolytically-gated organic transistors use a polymer/electrolyte

gel to gate the channel but this results in a slow switching speed. This work also demonstrates that the ionic liquid can be contained within a dielectric BN separator without affecting the time constant meaning these solid devices can show liquid-like switching speeds. This allows a fully printed transistor to finally be demonstrated with reasonable performance.

Although nanosheet network transistors have been demonstrated, much work remains. For example, it will be extremely important to improve the control over network morphology and connectivity with the aim of substantially enhancing the network mobility. In addition, the ionic liquid could potentially be optimised to improve the on:off ratio and switching speed. With such improvements, it is possible that nanosheet network transistors could challenge their organic and nanotube-based counterparts on both performance and ease of fabrication.

5.4 Coda

At the time of writing, there has been little in the way of similar publications since this work was first reported, although this is likely due to intervening time being short. However, a colleague at the University of Heidelberg (Higgins *et al.*) has a manuscript in submission that engages in deeper characterisation of such devices whose reported $\mu_{Net}C_V$ is consistent with the values presented above. This is quite reassuring as reproducibility was extremely important since this work represents the first complex device characterisation by this group. Higgins *et al.* also report on:off ratios > 10^4, an excellent improvement on the numbers presented in this chapter, which shows that electrolytically-gated nanosheet devices are already competitive with similar organic devices.

The study reported by Carey *et al.* in late 2017 on fully printed graphene transistors[107] is

also a valuable piece of work as this demonstrates that dielectric gating is feasible, for semimetallic networks at least. It will be especially interesting to see if this methodology can be extended to channels consisting of semiconducting TMDs as the minimum thickness of a printed dielectric layer may be the limiting factor in effective current modulation.

You may not be able to change the world but can at least get some entertainment and make a living out of the epistemic arrogance of the human race.

Nassim Taleb

6

Improving the Network Mobility

It is clear that 2D nanosheet networks hold good potential for electronic applications as we have seen that transistors can show promising mobilities and on:off ratios. The relative youth of 2D materials means that successful optimisation routes for similar materials can now be turned towards layered crystals. The past three decades have seen many functionalisation and ligand exchange techniques developed to

improve colloidal nanocrystal networks and these could serve as a roadmap for chemical improvements to the mobility of layered crystal networks.[220,221,222] Indeed, this has already begun as gold-decorated WS_2 nanosheets have recently been demonstrated.[223]

Many of the optimisation strategies will require complex chemistry to address the intersheet junction resistance but a simpler approach may be possible by drawing on previous composite work. Pathipati *et al.* demonstrated a thousand-fold increase in the mobility of a perylenediimide film through the inclusion of small amounts of graphene[224] and MoS_2 networks have shown a conductivity enhancement through the addition of carbon nanotubes.[225] This is relevant to printed 2D networks as the presence of graphene islands in a sea of MoS_2 nanosheets would allow carriers to alternate between travelling through MoS_2 and graphene, with the graphene sections acting as high mobility links in the overall conductive path. The reduction in carrier transit times should yield an increase in effective network mobility so, through this simple procedure, the performance of printed nanosheet devices could be improved to magnitudes competitive with organics and colloidal nanocrystals.

The aim of this work is thus three-fold. First, the fabrication of an inkjet-printed device with graphene electrodes and MoS_2-graphene channels for use as a planar photodetector is demonstrated. Second, it is evaluated in which way the addition of graphene affects both the electrical and photoconductive properties of the channel. Finally, this data is interpreted towards developing an understanding of how the presence of graphene affects the device properties such as mobility and carrier density.

6.1 Experimental Procedure

The bulk powders used in this study were purchased from commercial sources; graphite from Imerys (TIMREX, >99.5%), and MoS_2 from Sigma Aldrich (< 2 μm, 99%). The powders were initially dispersed at 20 g L^{-1} in NMP and sonicated with a horn tip sonicator (Sonics Vibracell VCX-750) for 1 hour at 60% amplitude. The dispersion was then centrifuged for 1 hr at 3218 g. The entire supernatant was then discarded and the sediment was redispersed in fresh NMP for resonication. This step removes particle impurities in the starting powder which aids stabilisation in the final ink.[207] Each material was then sonicated for 7 hours at 60% amplitude.

The dispersions were then subjected to a centrifugation trapping cascade to narrow the flake size distribution. Using a Hettich 220K centrifuge, the MoS_2 was trapped between 106g and 426 g to give relatively small nanosheets (~ 200 nm) whereas the graphene was trapped using 27 g and 106 g to give larger nanosheets (~ 600 nm). The sediments were redispersed in fresh NMP to a concentration of ~ 1 g L^{-1}. The optical extinction spectra were measured with a Varian Cary 500 in quartz cuvettes with a path length of 1 cm in 1 nm increments. The graphene and MoS_2 inks were then blended into a range of composites, each with a total concentration of 1 g L^{-1} but with the graphene mass fraction, $M_{f,G}$, varied from 0 wt% to 16 wt%.

The photodetectors were printed with a Dimatix DMP 2831 using all 16 nozzles. The platen temperature was set to 60 °C with the cartridge set to 40 °C. The interlayer delay was set to 5 mins. The illumination was provided by a λ = 403 nm laser (Toptica, iBeam) and the incident intensity was controlled using neutral density filters. The spot diameter was 3

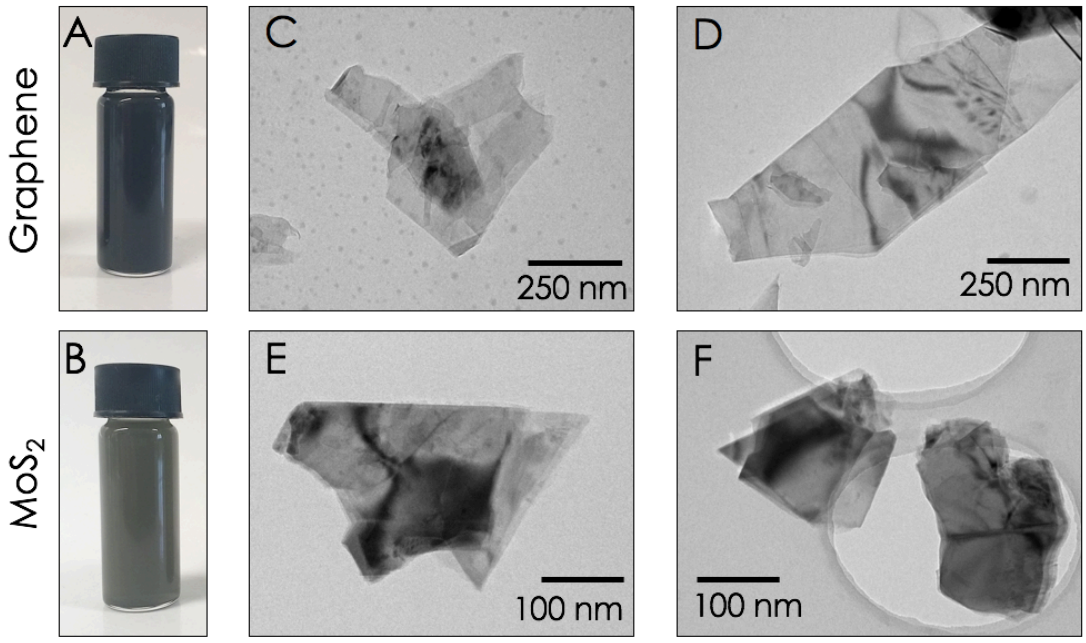

Figure 6.1: Graphene and MoS_2 inks. Photographs of A) graphene and B) MoS_2 inks. C-D) Representative TEM images of graphene nanosheets. E-F) Representative images of MoS_2 nanosheets.

mm which meant that approximately 55% of the device was illuminated.

6.2 Results and Discussion

6.2.1 Material and Device Analysis

The final 1 g L^{-1} nanosheet/NMP inks are shown in Figures 6.1A and B. The average lateral nanosheet dimensions could be extracted using optical spectroscopy through the reported extinction metrics for graphene[199] and MoS_2.[198] These provided lateral nanosheet dimensions for graphene of $\langle L \rangle \sim 650$ nm and for MoS_2 of $\langle L \rangle \sim 220$ nm. Although a precise quantification for layer number is currently not possible in NMP, $\langle N \rangle$ was ~ 10 for both materials. Figures 6.1C–F show representative TEM images of the graphene and MoS_2

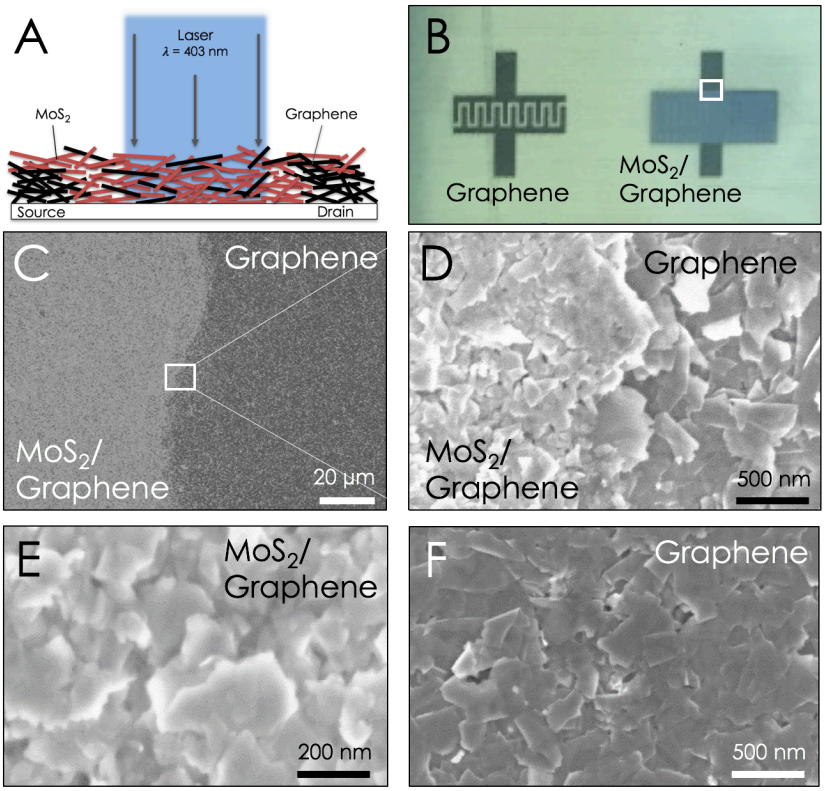

Figure 6.2: Imagery of a composite photodetector. A) A schematic of the composite photodetector. B) An optical image of the two printing steps where a graphene IDE is deposited before the composite channel covers it over. The white box indicated where SEM imaging was performed. C) SEM of the overlap area between the composite channel and the graphene electrode. D) A magnified view of (C). E) A magnified view of the composite channel and (F), a magnified view of the graphene electrode. Both visibly consist of disordered networks of nanosheets.

nanosheets and in each case, the inks are composed of nanosheets and the metric-derived dimensions are confirmed. The graphene nanosheets are somewhat larger than the soft limit of $1/50^{th}$ of the nozzle diameter[87] ($\sim$ 400 nm) but no clogging was observed during printing. This can likely be attributed to the dilute nature of the inks.

A schematic of the devices printed in this work is shown in Figure 6.2A. Figure 6.2B shows an optical image of the two printing stages. The first stage shows the interdigitated electrodes (IDEs) composed of graphene with inter-electrode channel dimensions of; length, L, = 200

μm; width, w, = 15 mm; and thickness, t, = 400 nm. The channel network was then printed on top of the IDE with a 2×5 mm^2 area and a 700 nm thickness which filled the inter-electrode spacing and provided good contact to the surrounding electrode area. The channel shown in Figure 6.2B is an MoS_2-graphene composite with $\mathcal{M}_{f,G} = 5\%$. The white box in Figure 6.2B indicates area where SEM imaging was performed. In all cases, good uniformity was shown over large areas. The interface between the graphene electrode and the the 5% composite, shown in Figure 6.2C, is relatively smooth with the transition occurring over ~ 10 μm. The higher magnification image shown in Figure 6.2D shows that the composite region can be clearly distinguished from the electrode region. The channel (Figure 6.2E) and the electrodes (Figure 6.2F) visibly consist of disordered networks of nanosheets.

The uniformity of the films can also be assessed through Raman spectroscopy. The normalised spectra for 3 graphene mass fractions are shown in Figure 6.3A. The E^1_{2g} and A_{1g} MoS_2 modes are clearly visible at 383 cm^{-1} and 409 cm^{-1} for each of the composites, with the suppressed graphene D- and G-bands scaling in proportion to $\mathcal{M}_{f,G}$. The uniformity can be indirectly assessed through the scaling of the peak intensity ratio with mass fraction. The mass fraction of graphene, $\mathcal{M}_{f,G}$, is

$$\mathcal{M}_{f,G} = \frac{\mathcal{M}_{f,G}}{\mathcal{M}_{f,G} + \mathcal{M}_{f,M}} \tag{6.1}$$

where $\mathcal{M}_{f,M}$ is the MoS_2 mass fraction. As $\mathcal{M}_{f,G} + \mathcal{M}_{f,M} = 1$, it then follows that the MoS_2 to graphene intensity ratio is given by

$$\frac{I_{MoS_2}}{I_G} \propto \frac{1}{\mathcal{M}_{f,G}} - 1 \tag{6.2}$$

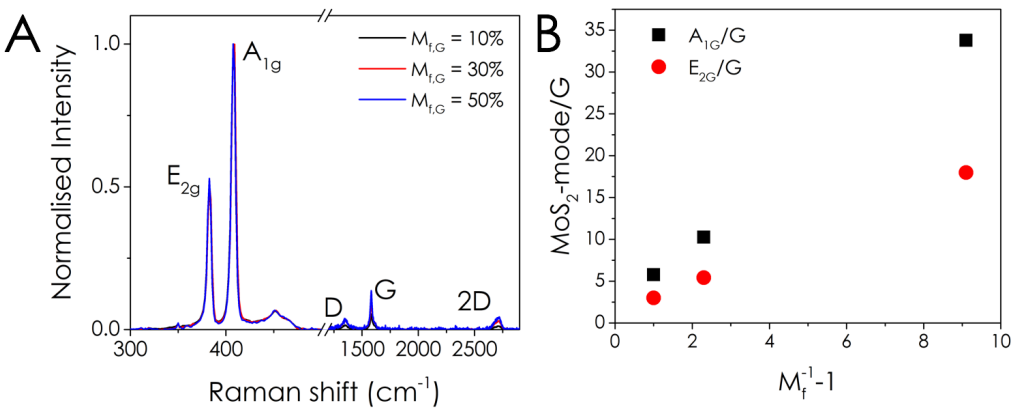

Figure 6.3: Raman spectroscopy. A) Raman spectra for 3 graphene mass fractions (10, 30, and 50%). The MoS_2 signal is relatively unchanged over the compositional range but the graphene bands show a scaling with the mass fraction. B) Ratio of MoS_2 mode to graphene G-band plotted against the graphene mass fraction.

This relationship is demonstrated in Figure 6.3B where the ratio of the peak intensities for both MoS_2 modes is shown to scale with the graphene mass fraction and linearity here implies that the composite films show good uniformity.[225]

6.2.2 Carrier Transport and Electrical Characterisation

As these networks are composed of discrete particles, a charge carrier must traverse many inter-nanosheet interfaces along a conductive path and each of these contributes a junction resistance to the overall network resistance. In this work, those interfaces between the MoS_2 and graphene nanosheets are of particular importance as significant barriers can form at metal-semiconductor junctions.[130] In such systems, the alignment of the energy levels of each component must be considered as a significant band offset would introduce potential barriers thereby increasing the network resistance. Alternatively, such barriers might foster charge separation upon illumination and increase the charge density as reported for acceptor-donor blends.[226]

Within the Mott-Schottky model, Ohmic contact at metal-semiconductor junctions can be achieved by matching the metal workfunction with the bottom of the semiconductor conduction band (for n-type materials). This is likely to be valid here, at least for basal-plane aligned nanosheets, as Fermi-level pinning is suppressed at van der Waals-bonded nanosheet-nanosheet junctions.[227] The workfunction of defect-free graphene nanosheets is ~ 4.3–4.6 eV below vacuum.[228] MoS_2 is generally an n-type semiconductor with a conduction band edge between 4.2 eV (monolayer)[227] and 4.6 eV (bulk)[229] below vacuum. Assuming the native doping level is unchanged after exfoliation and deposition, this implies relatively small Schottky barriers at the MoS_2-graphene junctions.[230] This does not preclude some MoS_2-graphene interfaces with non-trivial Schottky barriers, perhaps due to the interaction of chemically-active edge sites, but these should act as local, rather than global, barriers.

The absence of large Schottky barriers will reduce (but not remove) the MoS_2-graphene junction resistance. It is not yet clear what the magnitude of the junction resistance is or how it differs between MoS_2-graphene, MoS_2-MoS_2, or graphene-graphene junctions as, at the time of writing, very little is known about charge transport in nanosheet networks. However, the conductivity of networks composed solely of MoS_2 has been measured at 10^{-6}–10^{-5} S m^{-1},[204] while graphene-only networks display ~ 10^4 S m^{-1},[202] a difference of 9–10 orders of magnitude. This implies that the addition of graphene to an MoS_2 network should result in a significantly increased conductivity, provided the probability of MoS_2-graphene charge transfer is not prohibitively low. The observation of such increases (Figure 6.4) suggests that carriers can access the graphene nanosheets meaning the MoS_2-graphene junction resistances are not significantly higher than MoS_2-MoS_2 junction resistances.

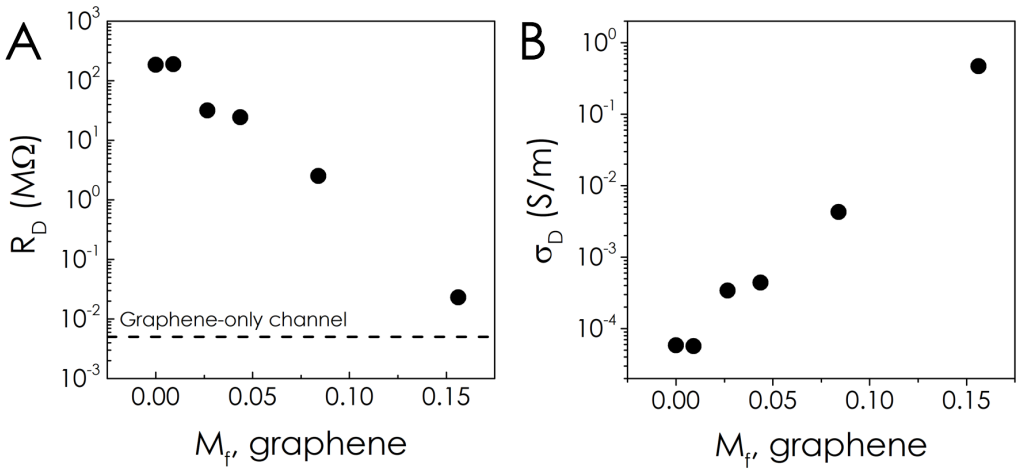

Figure 6.4: Network conduction. A) Device resistance and (B) channel conductivity as a function of the mass fraction of graphene nanosheets in the composite channel, both measured in the dark.

The dark resistance for each device is plotted against the graphene mass fraction in Figure 6.4A. The MoS_2-only device ($\mathcal{M}_{f,G}$ = 0 wt%) shows a large ~ 200 MΩ resistance but this drops significantly as the graphene content is increased. The highest graphene loading, $\mathcal{M}_{f,G}$ = 16 wt%, shows a resistance of ~ 20 kΩ, although this is still higher than a reference graphene-only channel which showed a resistance of 5 kΩ. The short channel length compared to the overall device dimensions means that this value should be close to the series resistance for the composite devices. This shows that the series resistance is negligible compared to the overall device resistance over most of the compositional range but would be expected to dominate for devices with graphene content much beyond 16 wt%.

The dark conductivity, σ_D, is plotted against the graphene mass fraction in Figure 6.4B. The conductivity of the MoS_2-only channel was ~ 5×10^{-5} S m^{-1}, reasonably close to previously measured values.[204] The channel conductivity increases exponentially with increasing $\mathcal{M}_{f,G}$, reaching ~ 1 S m^{-1} for the 16 wt% device. This behaviour is in line with

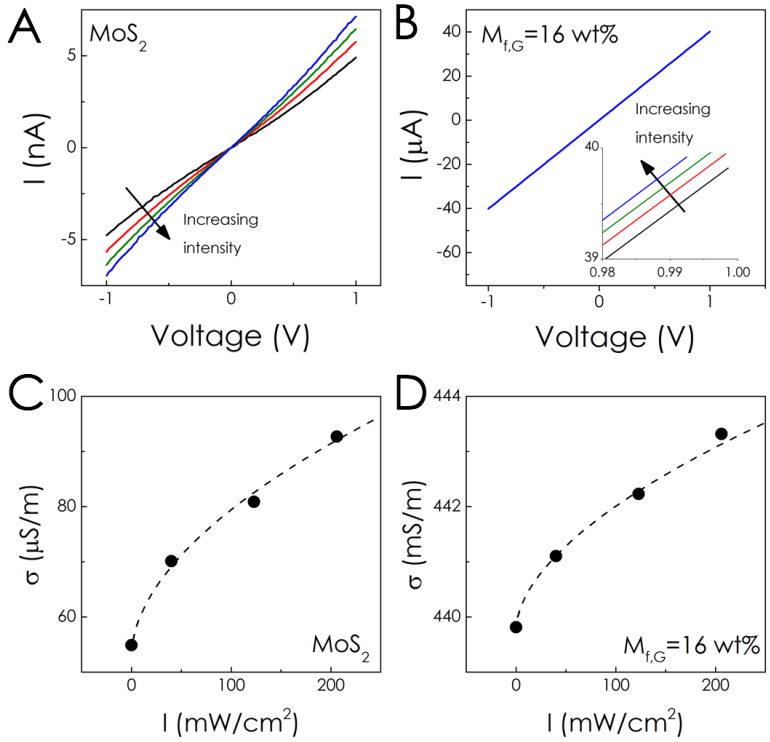

Figure 6.5: Illuminated response. Current–voltage characteristics for devices with (A) an MoS_2-only channel and (B) an MoS_2-graphene composite ($\mathcal{M}_{f,G}$ = 16 wt%) channel measured under the following intensities: 0, 40, 123, 206 mW cm^2. The inset in (B) shows a small but well-defined intensity dependence. Light intensity-dependent conductivity for devices with (C) an MoS_2-only channel and (D) an MoS_2-graphene composite ($\mathcal{M}_{f,G}$ = 16 wt%) channel.

previous work on the conductivity of vacuum-filtered MoS_2-graphene composites as a similar conductivity increase was shown to occur below the percolation threshold (i.e. the loading level where the first continuous conducting path is formed), with a steeper conductivity increase occurring just above the percolation threshold.[225] This effect will be discussed further below.

The photoresponse of these systems was analysed through current-voltage (I-V) characteristics at various incident light intensities. Representative I-V curves for a range of

laser intensities are shown in Figures 6.5A and B for an MoS_2-only channel (6.5A) and a 16 wt% channel (6.5B). The photoresponse is clearly visible for the MoS_2-only channel but the effect is much suppressed in the 16 wt% channel (see inset).

The conductivity of each sample is then plotted as a function of incident laser intensity in Figures 6.5C and D. In both cases, the conductivity under illumination, σ, increases sublinearly with intensity, a phenomenon often seen in nanosheet networks.[65,204] The conductivity increase upon illumination, or photoconductivity, shows the expected increase with intensity and scales as $\sigma - \sigma_D \propto I^{-\gamma}$, where γ is a material-dependent constant for a trap-limited system. These γ values ranged between 0.54 and 0.61 and are consistent with the reported value of 0.54 for planar MoS_2 networks.[225] This exponent is a measure of the depth of the traps below the conduction band (n-type) or above the valence band (p-type) and the lack of a trend with increasing graphene content suggests that the addition of graphene has no significant effect on the trap profile.

6.2.3 Percolation Analysis

In conductor-insulator composites, the dark conductivity as a function of conductive filler volume-fraction, φ_G, is usually described by percolation theory.[231] An important parameter in this theory is the percolation threshold, φ_C, which is the filler volume-fraction where the first continuous conductive path appears. Above the percolation threshold, the dark conductivity, σ_D, increases rapidly with filler content as $\sigma_D \propto (\varphi_G - \varphi_C)^n$, where n is usually > 2.[113,231,232] Above the percolation threshold, nominally insulating composites can have high conductivities as the current flows solely through the conducting network and is limited only by interparticle charge transfer. This regime is the topic of the vast majority of

reports on electrical percolation in composites. Conversely, the regime below the percolation threshold, where $\varphi_G < \varphi_C$, is much less studied. In this range, the filler particles are either isolated or aggregated in small clusters with no continuous conductive paths. This means there are two contributions to current flow; one solely through the insulating matrix, and one which alternates through insulating and conducting sections arranged in series. If the matrix conductivity is very low, we would expect the former to contribute very little to the conductivity. In the latter case, one can view charge carriers as travelling slowly in the insulating regions and rapidly in the conducting portions, resulting in a decrease in carrier transit time as the filler content is increased.[224] As a result, the latter contribution becomes more and more dominant as the conductive volume fraction increases, leading to a φ_G-dependent conductivity which is usually modelled using[232,233,234]

$$\sigma_D = \sigma_M \left[\frac{\varphi_C - \varphi_G}{\varphi_C} \right]^{-S} \tag{6.3}$$

where σ_D is the composite dark conductivity, σ_M is the dark conductivity of the insulating matrix, S is the percolation exponent, and $(\varphi_C - \varphi_G)/\varphi_C$ is known as the reduced volume fraction.

In such composites, the current flow should be spatially inhomogeneous and dominated by paths of least resistance. The low resistance pathways are those which minimise the portion of the journey through the matrix and maximise the number of traversed graphene nanosheet, thus lowering the overall transit time. The maximisation of traversed graphene means the network will be sensitive to the graphene loading level which will result in a highly non-linear φ_G-dependence (i.e. $S > 1$) with the actual value of S reflecting the structure of the emerging conducting network.

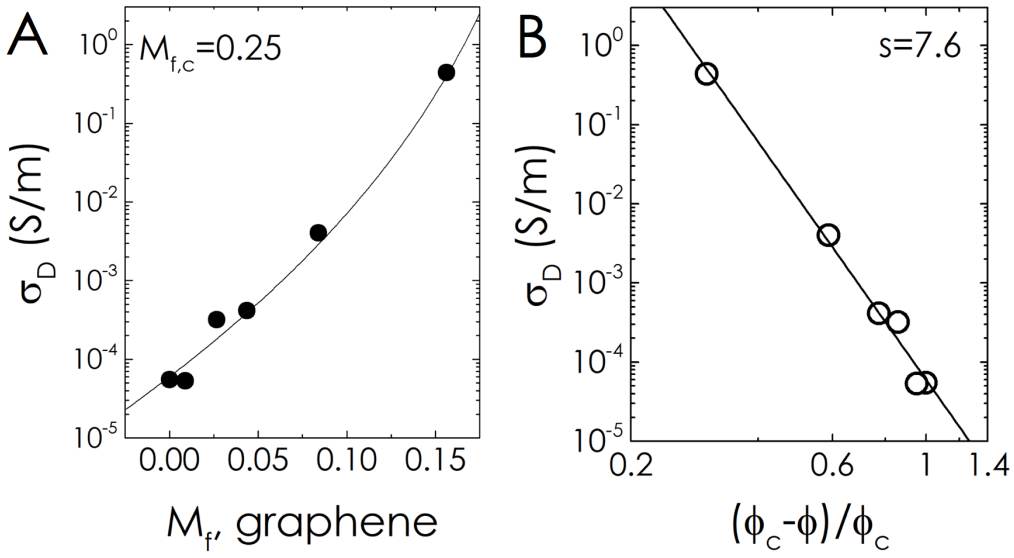

Figure 6.6: Percolation scaling of dark conductivity. Dark conductivity, σ_D, plotted versus graphene mass fraction (A) and reduced volume fraction (B). The solid line in (B) represents the prediction of percolation theory where the mass fraction equivalent of the percolation threshold was $\mathcal{M}_{f,C}$ = 25 wt%.

The dark conductivity versus graphene mass fraction data in Figure 6.6A show a smooth increase to a maximum value of ~ 1 S m^{-1} at 16 wt% graphene. The low conductivities and lack of a sharp increase indicate that each of the samples are below the percolation threshold. This implies that the percolation threshold is much higher than the values of ~ 1% which are usually observed in graphene-polymer composites.[235] However, these data are consistent with previous work on MoS_2-graphene composites and also in line with theory that suggests percolation thresholds can be high in systems of aligned discs.[225] Should each sample lie in the pre-percolation regime ($\varphi_G < \varphi_C$), no continuous graphene paths exist meaning all current flow will involve some transit *via* sections of MoS_2.

Eq. 6.3 is valid for samples below φ_C, however the mass fraction, $\mathcal{M}_{f,G}$, must be converted to volume fraction, φ_G, to accurately describe the emerging network. In polymer-matrix

composites, this conversion only requires knowledge of the matrix and filler densities but it is less straightforward in nano:nano composites due to their high porosity.[83] In relatively thick nano:nano composite films, the volume fraction can be found if the film density is known but for thin printed channels such as these, measurement of the density is not trivial. This is addressed with a simple relationship relating φ_G to $\mathcal{M}_{f,G}$ derived in Appendix B.2 (page 163) and stated here as

$$\varphi_G = \frac{(1 - \varphi_P)}{1 + (\mathcal{M}_{f,G}^{-1} - 1)\varrho_G/\varrho_M} \tag{B.23}$$

where φ_P is the volume fraction of the pores and $\varrho_M = 5060\,\mathrm{kg\,m^{-3}}$ and $\varrho_G = 2200\,\mathrm{kg\,m^{-3}}$ are the densities of MoS_2 and graphene, respectively. However, the measurement of the film porosity, φ_P, is also non-trivial meaning this equation cannot be used directly to convert $\mathcal{M}_{f,G}$ into φ_G. To resolve this, Eq. B.23 is transformed using the reduced volume fraction, again derived in Appendix B.2, and stated here as

$$\frac{\varphi_C - \varphi_G}{\varphi_C} = \frac{1 - \mathcal{M}_{f,G}/\mathcal{M}_{f,C}}{1 + \mathcal{M}_{f,G}(\varrho_M/\varrho_G - 1)} \tag{B.30}$$

where $\mathcal{M}_{f,C}$ is the mass fraction equivalent of the percolation threshold.

To test the validity of Eq. 6.3, the reduced volume fraction is calculated for different values of $\mathcal{M}_{f,C}$. In each case, the measured dark conductivity is plotted against $(\varphi_C - \varphi_G)/\varphi_C$ to find the value of $\mathcal{M}_{f,C}$ which gives the most reasonable fit. This reveals a well-defined power relationship between σ_D and $(\varphi_C - \varphi_G)/\varphi_C$ for $\mathcal{M}_{f,C} = 0.25$, as shown in Figure 6.6B. Fitting Eq. 6.3 (solid line) gives a percolation exponent of $S = 7.6$, in reasonable agreement with a previously reported value of $S = 5.2$.[225] While it is impossible to

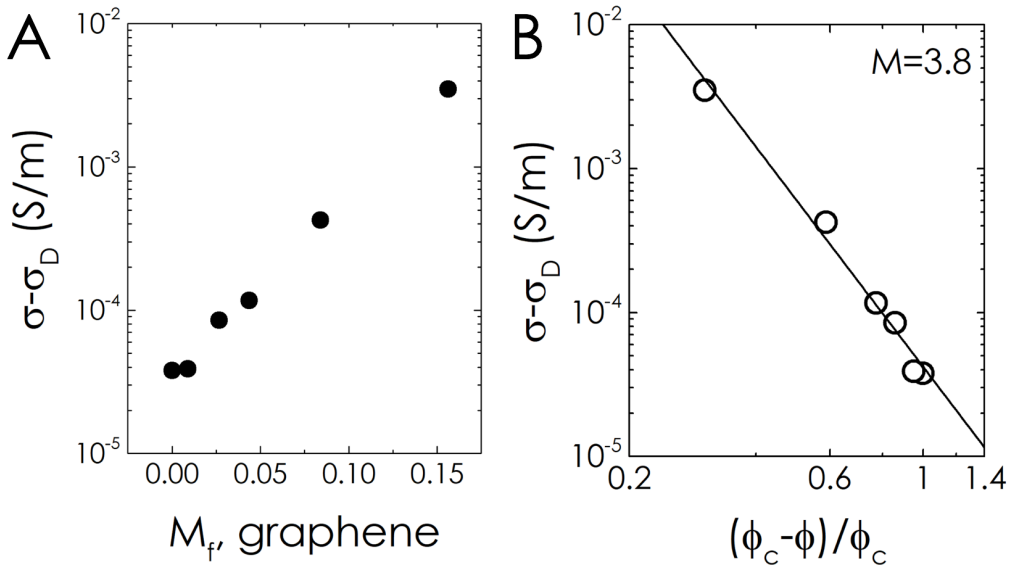

Figure 6.7: Percolation scaling of the photoconductivity. The photoconductivity, $\sigma - \sigma_D$, plotted versus graphene mass fraction (A) and reduced volume fraction (B). The conductivity under illumination, σ, was measured at an incident intensity of 206 mW cm^2 using a 403 nm laser The solid line in (B) represents the prediction of percolation theory where the mass fraction equivalent of the percolation threshold was $\mathcal{M}_{f,C}$ = 25 wt%.

convert $\mathcal{M}_{f,C}$ into a volume fraction without knowing the film porosity, the previous chapter found that nanosheet networks generally have porosity close to 60%. This allows φ_C to be estimated as ~ 22 vol%, which is in excellent agreement with the value of ~ 23 vol% previously reported for MoS_2-graphene composites.[225].

While electrical percolation in MoS_2-graphene composites has been observed previously, photoconductivity in such systems has not yet been studied. Figure 6.7A shows the photoconductivity plotted against the mass fraction of graphene. We find a two-order-of-magnitude increase in photoconductivity from ~ 4×10^{-5} S m^{-1} for the MoS_2-only channel to ~ 4×10^{-3} S m^{-1} for the 16 wt% graphene channel. It is clear that the addition of graphene below the percolation threshold results in large increases in

photoconductivity. This is likely because photo-induced charge carriers can travel rapidly to the electrodes due to the higher channel mobility conferred by the addition of graphene. This means that the photoconductivity could be tuned over a relatively wide range simply by controlling the graphene content.

Through a comparison of Figures 6.6A and 6.7A, it is clear that the photoconductivity increases significantly less than the dark conductivity as the graphene content is increased. To qualify this, both dark and illuminated composite conductivity are considered in terms of carrier density and mobility: $\sigma_D = qn_D\mu_D$ and $\sigma = qn\mu$, where q is the carrier charge, n_D and n are the dark and illuminated effective carrier densities, and μ_D and μ are the dark and illuminated mobilities. Under illumination, photocarriers are generated in the MoS_2 and the carrier density becomes $n = n_D + \Delta n$ at steady state, where Δn is the photoinduced carrier density. Assuming the mobility is invariant under illumination ($\mu_D \approx \mu$), the photoconductivity can be written as $\sigma - \sigma_D = q\mu_D\Delta n$.

In the dark, both mobility (μ_D) and carrier density (n_D) will increase with graphene content,[236] with the mobility increase caused by the reduced transit time.[224] In addition, the graphene sheets will almost certainly be doped due to their interaction with the environment (residual solvent, etc) and will have a much higher free carrier density than the MoS_2. This will lead to an increase in the network carrier density as the graphene content increases. In a percolating system, both carrier density and mobility might be expected to follow percolation-like scaling laws, but it appears that this has not yet been reported. However, there are some results published by Tan *et al.* that indicate this is approximately

true.[236] This allows the carrier density and mobility to be written as

$$n_D = n_M \left[\frac{\varphi_C - \varphi_G}{\varphi_C} \right]^{-N} \tag{6.4}$$

and

$$\mu_D = \mu_M \left[\frac{\varphi_C - \varphi_G}{\varphi_C} \right]^{-M} \tag{6.5}$$

where n_M and μ_M are the dark carrier density and mobility of the matrix (i.e. that of MoS_2, which we take to be independent of light intensity). This means that the dark conductivity can be written as

$$\sigma_D = q n_M \mu_M \left[\frac{\varphi_C - \varphi_G}{\varphi_C} \right]^{-(N+M)} \tag{6.6}$$

This shows that the φ_G-dependence of the dark conductivity has contributions from both mobility and carrier density and, by comparison with Eq. 6.3, means that $S = N + M$.

The photo-induced carrier density, Δn, would be expected to weakly depend on the graphene content below percolation as the primary effect of the graphene is to reduce the amount of MoS_2 available to generate photocarriers ($\Delta n \propto 1 - \varphi_G$). Approximating Δn as independent of φ_G allows the photoconductivity to be written as:

$$\sigma - \sigma_D \approx q \Delta n \mu_M \left[\frac{\varphi_C - \varphi_G}{\varphi_C} \right]^{-M} \tag{6.7}$$

This expression implies that, at this level of approximation, the φ_G-dependence of the photoconductivity has a contribution from the mobility, but not the carrier density. In

addition, it also implies percolation-like scaling behaviour. This is tested in Figure 6.7B where the photoconductivity is plotted against the reduced volume fraction and calculated using the same percolation threshold as was found for the dark conductivity ($\mathcal{M}_{f,C}$ = 25 wt%, φ_C = 22 vol%). We find good linearity, in agreement with Eq. 6.7, which is consistent with $\mathcal{M}$ = 3.8. This result is important as it implies that the data in Figure 6.7B reflect a mobility dependence on graphene content.

The data in Figure 6.7A show that the photoconductivity increases one hundred-fold between the MoS_2-only and 16 wt% channels. Such an increase is consistent with previous work which demonstrated that the mobility of organic devices could be increased a thousand-fold through the addition of graphene.[224] The mobility of an MoS_2 nanosheet network was measured in the previous chapter as ~ 0.1 $cm^2\ V^{-1}\ s^{-1}$, which means the network mobility of the 16 wt% composite could be as high as ~ 10 $cm^2\ V^{-1}\ s^{-1}$. Should this inferred value be correct, the mobility of these simple devices would be competitive with state-of-the-art printed organic devices.[237]

The comparison between Figures 6.6A and 6.7A also shows the photoconductivity increasing less rapidly with graphene content than the dark conductivity. This means that the fractional photoconductivity, $(\sigma - \sigma_D)/\sigma_D$, decays with mass fraction. These data are plotted in Figure 6.8A and show a rapid decline in $(\sigma - \sigma_D)/\sigma_D$ with $\mathcal{M}_{f,G}$, falling from ~ 0.7 for the MoS_2-only channel to ~ 0.01 for the 16 wt% sample. Dividing Eq. 6.7 by Eq. 6.6 shows the fractional photoconductivity scales with reduced volume fraction as

$$\frac{\sigma - \sigma_D}{\sigma_D} = \frac{\Delta n}{n_M}\left[\frac{\varphi_C - \varphi_G}{\varphi_C}\right]^N \tag{6.8}$$

Figure 6.8B plots the fractional photoconductivity versus reduced volume fraction, again

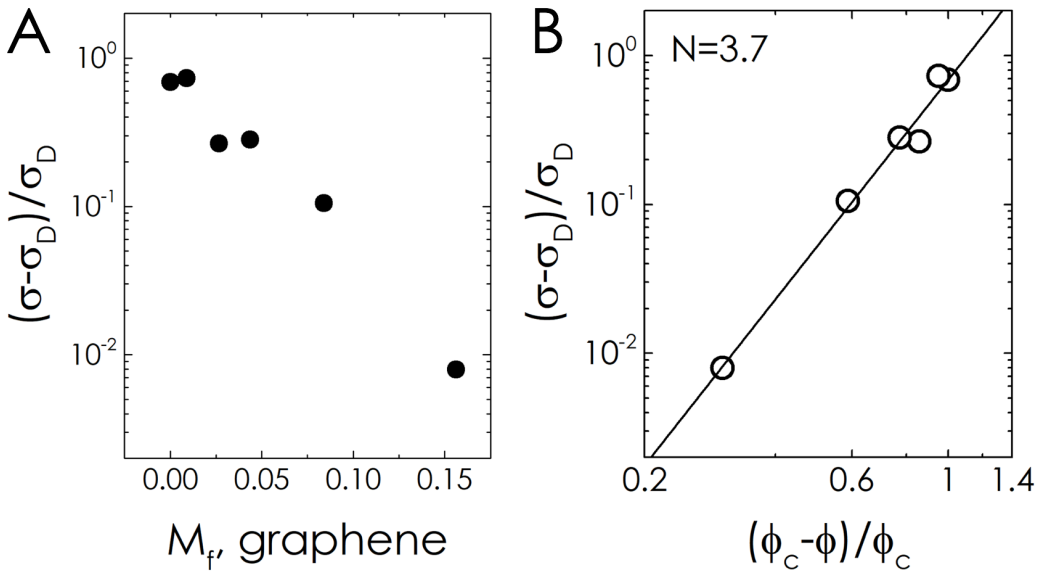

Figure 6.8: Percolation scaling of the fractional photoconductivity. The fractional photoconductivity, $(\sigma - \sigma_D)/\sigma_D$, plotted versus graphene mass fraction (A) and reduced volume fraction (B). The conductivity under illumination, σ, was measured at an incident intensity of 206 mW cm^2 using a 403 nm laser The solid line in (B) represents the prediction of percolation theory where the mass fraction equivalent of the percolation threshold was $\mathcal{M}_{f,C}$ = 25 wt%.

calculated using the same percolation threshold found for the dark conductivity ($\mathcal{M}_{f,C}$ = 25 wt%, φ_C = 22 vol%). As predicted by Eq. 6.8, percolation-like scaling is observed, consistent with N = 3.7. Again, this means the data in Figure 6.8B reflects the increase in dark carrier density with increasing graphene content. In addition, Eq. 6.8 implies that the fractional photoconductivity will approach zero as the percolation threshold is approached. This is intuitive as the amount of current flowing through the MoS_2 should be negligible compared to the current flowing through the graphene above the percolation threshold.

These data suggest that the increase in dark conductivity with graphene content below the percolation threshold is due to graphene-induced increases in both mobility and effective carrier density. The similarity of the N and $\mathcal{M}$ exponents indicates that the relative

contributions of mobility and carrier density are comparable in magnitude. However, the graphene-content dependence of the photoconductivity depends only on the graphene-induced mobility increase. Similarly, the $\mathcal{M}_{f,G}$ dependence of the fractional photoconductivity depends only on the graphene-induced carrier density increase. As a result, measuring the photoconductivity in such composites is a useful way to differentiate the effects of filler content on mobility and carrier density, parameters which are usually aggregated in the conductivity.

6.3 Conclusions

This work shows that all-printed, all-nanosheet devices can be fabricated where the active channel is a composite material and the graphene electrodes contribute negligible series resistance. Both dark- and photo-conductivity are described by percolation theory with the photoconductivity reflecting the increase in channel mobility associated with the graphene. It is possible that these results could be translated to other device types. One possibility might be to fabricate transistor channels from MoS_2-graphene composite networks where the addition of graphene would be expected to increase the mobility. However, the percolation-related increase in dark current could result in significantly increased off-currents in such composite transistors. This is obviously a potential disadvantage which must be weighed against the advantages of increased mobility.

6.4 Coda

This study represents a tentative feel of the degree to which mobility is affected through a 2D:2D composite. The strong indication that mobility is enhanced has driven a follow-up

study where the TFTs are printed with WS_2-graphene composite channels. This allows the mobility to be extracted from the transfer curves using the methodology developed in the last chapter thus facilitating a systematic characterisation of the electrical behaviour of these composites. As this chapter is predominantly a building block for the follow-up work, it is hoped that the use of photoconductivity to decouple mobility from carrier density in these composites will be of value to the field in general.

As a personal aside, this study provided an excellent opportunity to engage in modelling to a much greater degree than that afforded by the previous two chapters. This was extremely refreshing as maths skills tend to atrophy with disuse.

Orr would be crazy to fly more missions and sane if he didn't, but if he was sane he had to fly them. If he flew them he was crazy and didn't have to; but if he didn't want to he was sane and had to. Yossarian was moved very deeply by the absolute simplicity of this clause of Catch-22 and let out a respectful whistle.

7

Conclusions and Future Work

The excitement riding the wake of the graphene gold-rush has driven investigative momentum for the last decade. A definitive indicator that the hype has been vindicated will occur when the yearly rate of patent applications begins to outpace the number of submissions to academic journals. This places device applications at the fore and of these, electronics printed using inks laden with nanosheets are a promising

short-term showcase. The aim of this work was to address some of the challenges faced by the current generation of printed 2D electronics by broadening the understanding of the electrical properties of nanosheet networks.

As most of the applications to date have been planar, the move to vertical heterostructures required a new protocol for creating pinhole-free layers. This was developed through a study on printed capacitors with the devices constructed by inkjet printing a graphene electrode, then spray coating a dielectric boron nitride layer onto the graphene network, and inkjet printing another graphene electrode on top to complete the device. The DC current through the device was found, through trial and error, to be zero for thicknesses over 1.65 μm. This is quite thick and can, in part, be attributed to the lack of a binder in the BN ink. This was omitted to preserve the purely-nanosheet aspect of the devices but may be incorporated into future devices. The capacitance was then extracted by fitting the Bode plots obtained from impedance spectroscopy and the areal capacitance ranged from 0.24 to 1.1 nF cm^{-2}. The Bode plots also provided an *RC* time constant of 0.74 μs for these devices. The dielectric constant could be determined using the imaginary impedance and, for $\omega < 10^5$ rad s^{-1}, the relative permittivity was invariant with thickness and frequency at ~ 2–2.5, which is consistent with previous reports.

Once a methodology was in place for printing vertical heterostructures, it was possible to move on to developing printed transistors. The current modulation is generally quite poor in nanosheet networks that are electrostatically gated and this is likely caused by structural screening within the network. This can be overcome by using an ionic liquid to completely penetrate the film which allows the entire network to be switched. This was demonstrated for networks composed of MoS_2, $MoSe_2$, WS_2, and WSe_2, with the extracted mobilities

ranging from 0.08 to 0.2 $cm^2\ V^{-1}\ s^{-1}$. The similarity in mobility across the materials strongly indicates that charge transport in these networks is limited by inter-sheet tunnelling, the reduction of which should provide significant improvements. The transconductance of such networks was also found the scale with the network thickness, which provides a useful new degree of freedom for these devices. The use of a liquid to gate the network typically precludes practical implementation and electrolytes are usually mixed into a polymer gel when creating solid device. The reduction in switching speed this brings was demonstrated through the comparison of the switching speeds of a planar transistor gated with an unadulterated ionic liquid (~ 90 ms) and an ionic gel (~ 750 ms). This was remedied by spray coating a BN network onto the device and filling its porous free volume with the ionic liquid. The porosity of such sprayed films is ~ 60% meaning the ions experience an unhindered mobility under a gate bias and such a structure showed identical switching speeds (within error) as the purely-liquid device (68±10 ms *vs* 87±15 ms). These results taken together allowed a fully printed nanosheet network transistor to be demonstrated. Here, a set of graphene electrodes and a WSe_2 channel were inkjet printed, a BN network was then spray coated, and a graphene electrode was inkjet printed on top. The ionic liquid was then drop-cast onto the heterostructure to create a pseudo-solid device. Although proof-of-concept, this device performed reasonably well, with a transconductance of 22 μS and an on:off ratio of ~ 25.

There are many chemical avenues available for increasing the mobility of these nanosheet networks but these are generally complex. Previous studies have shown that the conductivity (and hence mobility) of a semiconducting or insulating network can be enhanced through the addition of a conductive filler below the percolation threshold. This

was investigated through a percolation study on the effect of graphene loading in an MoS_2 ink which was subsequently printed into a photodetector. The behaviour of both dark conductivity and photoconductivity were described by percolation theory, where the scaling of the photoconductivity reflected the increase of the network mobility associated with the graphene. This could have applications in transistor channels as this study indicated the mobility may increase by a factor of one hundred. This may also represent a simple way to decouple the mobility and carrier density from the conductivity through the measurement of the photoconductivity for such composites.

The methods and results demonstrated here represent preliminary steps on the path towards creating circuitry from nanosheet networks. The numbers, in particular the network mobility, are extremely promising especially when one considers where conjugated polymers began. As people have notoriously poor predictive ability, the remaining paragraphs will be limited to describing the immediate work focused on optimising the network characteristics.

- *Towards mechanically robust nanosheet networks*

The work presented in Chapter 4 was hindered by the brittle nature of the networks and, anecdotally, some redispersion of the BN was observed in the ionic liquid during the study in Chapter 5. In general, the integrity of the networks has been improved by exfoliating the crystals in a polymer such as ethyl- or nitro-cellulose which provides stability in dispersion and mechanical strength in a printed film.[238,239,240] The mechanical strength comes at the expense of network conductivity necessitating polymer decomposition and this is typically achieved either thermally[70] or photothermally.[241] These treatments tend to require high temperatures

(> 300 °C) making them incompatible with many printing-specific substrates and, naturally, the removal of the polymer means the film loses its mechanical strength.[238]

A far better approach would be through a 1D:2D composite akin to the carbon nanotube/nanosheet composites that are frequently reported.[242,243,244] Here, CNTs are typically used to aid charge transport in the network but the recent reports have systematically demonstrated mechanical reinforcement at low volume fractions ($\varphi < 5\%$). This work could be directly built upon using an insulating 1D material such as boron nitride nanotubes (BNNTs). A study could be approached through an investigation of the effect of BNNT loading on the minimum thickness of a printed dielectric capacitor. Should redispersion be limiting factor in printing thin BN layers, the reinforcement provided by the BNNTs could permit much thinner dielectrics to be deposited. This has implications beyond dielectric networks as BNNTs could potentially be used to reinforce all manner of nanosheet networks. Thus, the second phase such a study would investigate the evolution of the conductivity in a graphene network with the BNNT loading.

- *Towards higher mobility nanosheet networks*

It has been shown that transport in semiconducting TMD networks is junction limited as ~ 0.1 cm^2 V^{-1} s^{-1} appears to be the ceiling for ostensibly unadulterated nanosheets. This area is thus ripe for development as a plethora of routes to optimisation are available. These efforts can be split into network modification and nanosheet modification, where the former concerns optimisation of the aggregate characteristics of the nanosheets, and the latter involves modification of the nanosheets themselves. Three immediate network investigations are the following:

1. A follow-up study on the results in Chapter 6 would recreate this work in the manner of Chapter 5, where TFTs would be investigated in the place of photodetectors. This would allow the decoupling of mobility from the carrier density as the mobility could be extracted from the transfer curves. It is likely that the addition of graphene will raise the mobility at the expense of the on:off ratio, as the conductivity increase will cause significantly increased off-currents but this needs to be systematically quantified.

2. A broad study on the role of nanosheet dimensions is necessary as the commentary to date has been purely qualitative. As these networks are junction-limited, the junction effect needs to be investigated through a rigidly controlled size-dependence study. Such a study is now possible as fine control over the nanosheet dimensions can be achieved through liquid cascade centrifugation coupled with optical metrics.[198,199] This information would be extremely valuable when formulating further strategies for network optimisation.

3. A study on the effect of network morphology on charge transport would also be highly useful for printed applications. The various deposition techniques create a range of both network densities and nanosheet alignments and, as has repeatedly been shown for carbon nanotubes, the internal alignment plays a large role in effective charge transport. It is unclear how the intersheet contact (edge-to-basal plane, edge-to-edge, basal plane-to-basal plane, etc.) plays a role in charge transport but an investigation here should compliment the nanosheet modifications for reducing the intersheet junction resistance. The role of porosity and penetration of ionic liquid is also unknown but likely could undergo further optimisation through a similar study.

The avenues for modifying the individual nanosheets are almost endless. There are a multitude of chemical approaches available through molecular chemistry, many of which are reviewed in Ref. (194). The majority of these methods involve the decoration of discrete, mechanically-exfoliated monolayers but there are several liquid-phase functionalisation strategies also available that may be pertinent to printed devices. Dunklin *et al.* have demonstrated that a reaction can be driven between liquid-exfoliated WS_2 and $HAuCl_4$ resulting in gold nanoparticles covalently bonded to the edge sites of the nanosheet.[223] The higher mass of the Au-decorated WS_2 also facilitates a much higher monolayer yield after centrifugation which will be useful for exploring the properties of monolayer-based nanosheet networks. This has also been demonstrated with other noble metals such as platinum,[245] palladium,[246] and silver[246] and the metal-metal intersheet contact may reduce junction resistances in a network composed of such modified nanosheets. In a similar vein, a hybrid MoS_2 nanosheet with a 2H basal plane with a 1T perimeter has been demonstrated where the 1T edge is produced though organic ligands.[247] A network of such nanosheets was reported to have a mobility of 170 $cm^2\ V^{-1}\ s^{-1}$ and, although interesting, a much deeper characterisation is needed to confirm this.

Although there may be a paralysis of choice caused by the many possible optimisation routes, this should still be considered an advantage for field of 2D materials. In answer to the question posed in the introduction, it certainly appears that 2D materials will find a place in the future of printed applications.

A

Ancillary Techniques

This appendix will outline the fundamentals of the relevant support techniques that have been used to characterise the samples and devices created in this work. This section is split into spectroscopic and microscopic techniques.

A.1 Spectroscopic Characterisation

Optical Spectroscopy

Optical spectroscopy is an extremely useful technique for characterising solution-processed materials. As light propagates through a liquid medium, the photons are affected through a number of interactions with the dispersed media. As the wavelength of the incident light is swept from ultraviolet to near-infra-red, the spectral output is called the extinction spectrum and consists of both absorption and scattering processes. Absorption occurs when the energy of the light can excite an electronic transition within the dispersed material which, for semiconductors, means appreciable absorption only occurs for energies greater than the bandgap. This, through Fermi's Golden Rule, provides a measure of the joint density of states in the conduction band.[248] The photons can also scatter from the dispersed particles which also contributes to the extinction spectrum; the process is elastic if the photon energy is unchanged but is inelastic if the energy is exchanged with the particle. Further, if the particle density is sufficiently high, they can influence each other's energy levels causing peak broadening over a number of wavelengths.[248] These processes are related to the attenuation of light through the Beer-Lambert Law. From Figure A.1, if the intensity through a reference is I_o but the intensity through the sample is I, then the photons have interacted with the sample and the extinction is given by

$$Ext = \ln \frac{I}{I_o} = -\ln T \tag{A.1}$$

where T is the transmittance. As the extinction will depend on the number of particles in the sample and the distance through which the light must pass, Ext goes linearly with

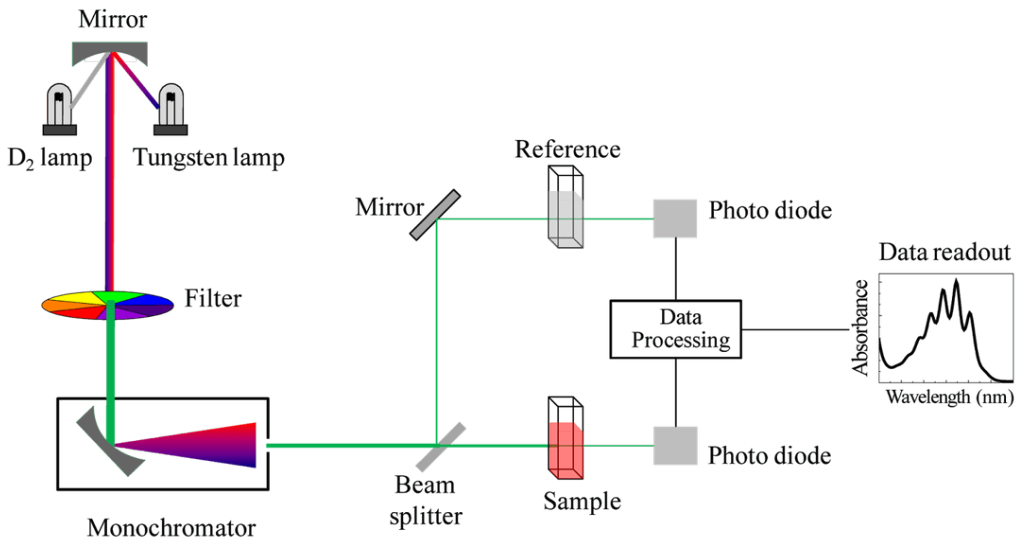

Figure A.1: Cary UV-Vis spectrophotometer. Image from Ref. (249).

concentration, C, and the path length, l. Each material will also behave differently and have a specific extinction coefficient, leading to the standard expression

$$Ext = \varepsilon Cl \tag{A.2}$$

where the extinction coefficient, ε, contains the absorbance and scattering contributions such that

$$\varepsilon(\lambda) = \alpha(\lambda) + \sigma(\lambda) \tag{A.3}$$

As the molecules in liquid solutions are typically too small to scatter light, the scattering component is negligible and hence extinction and absorbance are typically used interchangeably. This is not the case for dispersions however as nanosheets are typically >

50 nm meaning extinction spectra often contain a significant scattering contribution.

A Varian Cary 6000i (200 – 1800 nm) dual beam spectrometer was used throughout this thesis for characterising the extinction of dispersed nanomaterials. The visible-IR light is generated with a tungsten lamp and UV light is created with a deuterium arc source.[249] The composite light is resolved into its individual wavelengths by a monochromator which consists of a diffraction grating with a series of mirrors and slits. The beam splitting shown in Figure A.1 improves the accuracy of the readings by minimising the reflection, scattering, and absorption by the solvent through use of a reference. The beam splitter contains a chopper which allows the detector to easily alternate between sample and reference beams and the light is then detected using an InGaAs photodiode.

This tool can also be fitted with an integrating sphere to detect the absorption component of the extinction and, once the extinction and absorbance are known, the scattering component can be determined through Eq. A.3. The integrating sphere has an internal diameter of ~ 150 mm with a rough white reflective coating on the entirety of the inside walls. This coating diffuses the scattered light throughout the sphere which ensures the scattering component is in a steady state and can thus be subtracted from the extinction to give the absorbance. These purely absorptive measurements are important for creating the optical metrics as the extinction coefficient is strongly dependent on the size of the nanosheets.

Raman Spectroscopy

It is also possible to extract information from solid-phase samples through Raman spectroscopy. Raman analysis derives from inelastic light-matter interactions where monochromatic light is used to probe the atomic displacements in the lattice, also known as phonons. These displacements can be modelled as harmonic oscillators where the oscillatory behaviour is quantised and is a key signature of the bond strength. The majority of photons incident on a material's atomic constituents are Rayleigh scattered as the wavelength of the photons is much larger than the size of the atoms or molecules. The photons that interact with the material are inelastically scattered and thus contain information about the lattice.

The interaction is a two-photon process, where the electric field of the incident photon induces a dipole moment in the material's electron cloud and is thus a strong function of the material's polarisability. The relaxation of the dipole then emits radiation that is frequency-shifted compared to the incident light, where the shift corresponds to the energy gained or lost by the material. This shift is calculated as[250]

$$\upsilon = \frac{1}{\lambda_i} - \frac{1}{\lambda_s} \tag{A.4}$$

where λ_i and λ_s are the wavelengths of the incident and scattered light. The various possible transitions are shown in Figure A.2.[251] The scattering usually occurs between the ground state and a short-lived virtual state, a brief distortion in the electron distribution, rather than a stationary state. A Stokes Raman shift in the scattered light occurs when energy is imparted to the lattice as the excitation terminates with the atom in an excited

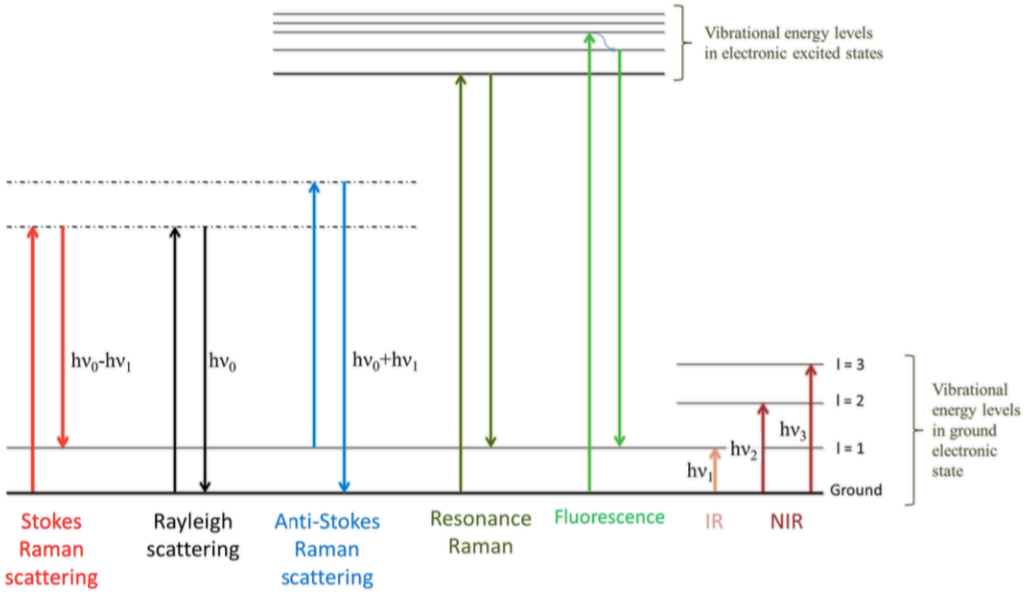

Figure A.2: Various Raman Processes. Image taken from Ref. (251).

vibrational state. An anti-Stokes shift is the opposite, where an initially excited vibrational state transitions to the ground state with the excess energy absorbed by the scattered photons. Resonant Raman scattering can also occur when the energy of the incident light is close to that of an electronic transition in the material which results in a much increased scattering amplitude.[252] This increased absorption can also cause sample damage.

The Raman spectrum is a plot of the intensity of the scattered light as a function of the Raman shift and is thus a direct measure of the phonon density of states. The shape of the spectra facilitates analysis of nanosheet features such as defects, doping, interlayer coupling, and stress making the technique integral to nanomaterial analysis.[250]

A.2 Microscopic Characterisation

Atomic Force Microscopy

Atomic force microscopy is a scanning probe technique for measuring the topography of a sample. This is achieved through force interactions between a sharp-tipped probe and the surface meaning the resolution is determined by the radius of curvature of the tip. As the tip is rastered across the surface, it is deflected by surface features and these deflections are software-interpreted into an image. The tip is attached to a cantilever which interacts with the surface according to Hooke's Law. The degree of deflection is determined by a laser that reflects from the back of the cantilever onto a photodiode. This deflection signal is used by the software to adjust the z-piezoelement so the tip remains at a constant height determined by the imaging mode.[253] The schematic in Figure A.3 outlines this procedure.

The topographical information can be collected through a number of different imaging modes that measure the static height of the cantilever or its dynamic oscillation. The simplest mode of operation was the first developed for the technique and is known as contact mode. As the tip is lowered towards the sample surface (with zero deflection), the attractive forces cause the tip to "snap-in" as it comes in contact with the surface. The contact here means that the forces being measured are repulsive. The tip is in constant contact with the sample which facilitates fast imaging but means there is also a risk of tip damage or sample degradation. This mode is generally used for high resolution imagery with rigid samples as the contact creates lateral forces which can lead to distortions or damage.[253]

In non-contact mode, an oscillating signal is fed to the cantilever so the probe will oscillate close to its resonant frequency. As the probe is lowered towards the surface, the frequency of

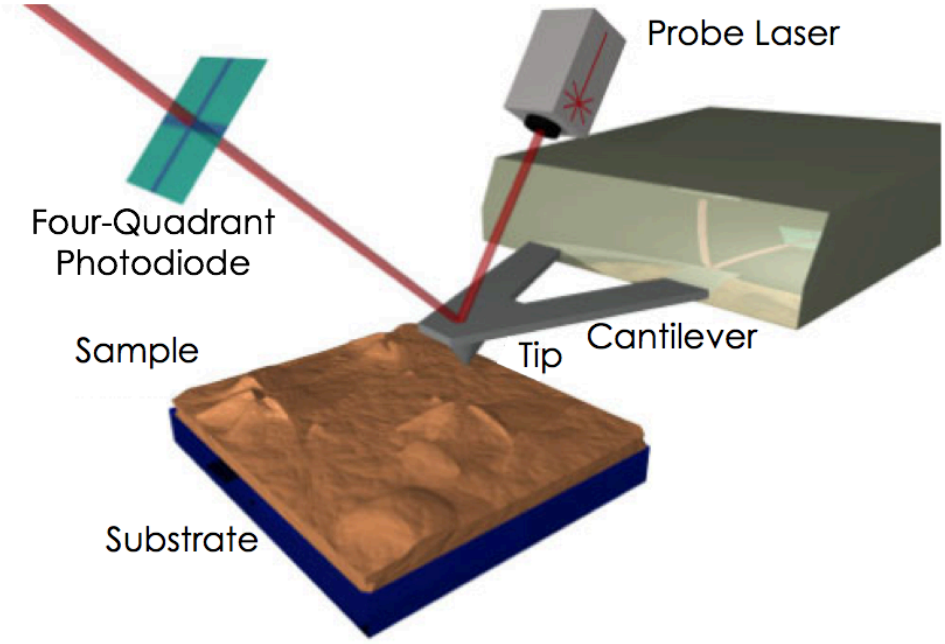

Figure A.3: A general outline of AFM operation. A laser reflects from the back of the cantilever which reflects the topology of the sample through deviations detected by a photodiode. Image taken from Ref. (253).

the oscillation will be attenuated through interactions with the sample. The frequency shift is fed back into the software where the height is then adjusted to maintain a constant oscillation frequency (or constant probe-sample interaction) and an image is thus generated. This mode is clearly useful for unbound samples but is tricky to operate in as the tip must be kept close to the surface without crossing into the repulsive force regime used in contact mode. This is challenging as there is always an adsorbed water layer on all ambient samples.[253]

The drawbacks to these two operating modes can be overcome by intermittent contact mode, or tapping mode. Here, the feedback modulates the amplitude as the tip experiences both attractive and repulsive forces. The vertical motion of the tip means that there are no lateral forces created during scanning and also that the tip will pass through the

contamination layer. These advantages have made tapping mode the most widely used of the AFM modes.

A Digital Instruments Nanoscope IIIA from Veeco systems was used for AFM analysis throughout this thesis. The measurements are all carried out in ambient with a silicon tip with a resonance frequency of ~ 300 kHz, a force constant 40 N m^{-1}, and a tip radius of 10 nm.

Transmission Electron Microscopy

Electron microscopy is an widely used technique for overcoming the resolution limits of visible light microscopy. The wavelength of the electron is tied to its momentum through the hyperbolic relationship

$$h = p\lambda = (mv)\lambda \tag{A.5}$$

where h is the Planck constant and the other symbols have their usual meaning. This means that very short wavelengths can be achieved with high velocity electrons; an accelerating voltage of 50 kV results in a wavelength of 0.05 Å. These high energy electrons can penetrate several microns into a sample or, in the case of nanomaterials, can pass completely through. As the electrons pass through the sample, they can interact elastically or inelastically and the attenuated signal intensity forms the basis for transmission electron microscopy (TEM) imagery. These images are created from the spatial variation of scattered electrons reaching the detector where their contrast forms a 2D image from a 3D sample. This is extremely useful for imaging crystalline samples as the diffraction pattern contains much useful information about the crystal structure of the sample. A schematic of a TEM

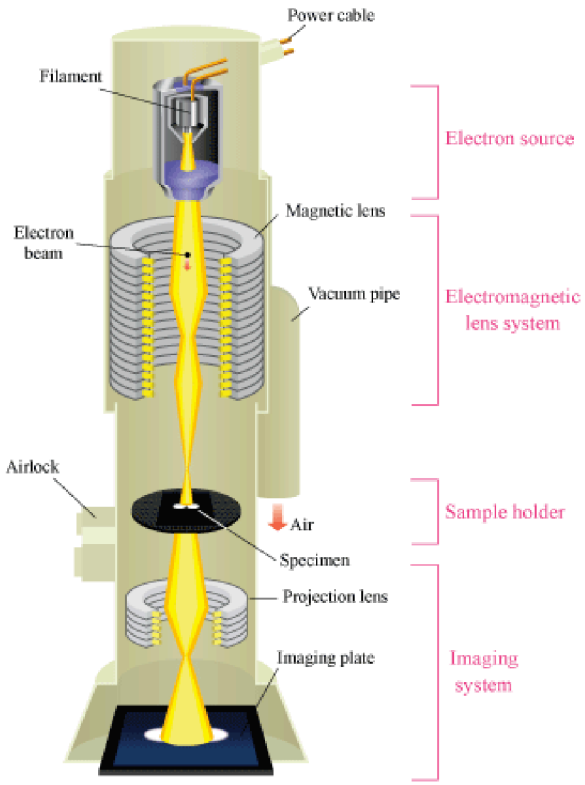

Figure A.4: A schematic representation of a TEM column. Image from Ref. (254).

column is shown in Figure A.4.[254]

The microscope is composed of 3 main elements; the illumination system, the specimen stage, and the imaging system. The illumination system contains the electron source whose type depends on the desired resolution; a thermionic LaB_6 or tungsten filament is used for normal resolution and Schottky field emission or cold field-emission guns are used in high resolution machines. Two or more condenser lenses accompany the electron gun which are used to focus the electrons onto the sample. The illumination stage determines the diameter at the sample and the intensity in the resulting image.[255] The specimen stage contains the

sample and can be inserted or withdrawn from the microscope. It is critical for well-resolved images that this stage is held completely stationary. As the beam passes through the specimen, some electrons pass straight through unimpeded while others are scattered both backwards and forwards. The emergent beam passes into the imaging system where a series of lenses project and magnify an image onto a cooled CCD to record the image. The imaging system determines the magnification of the image and the design of the lenses determines the spatial resolution.[255]

Despite the picometre wavelength, typical TEM resolutions are limited to ~ 0.5 nm by various types of component aberrations. These include spherical aberrations that occur from imperfections in the focusing system and chromatic aberrations due to disparate electron energies incident on the specimen. Astigmatisms can also occur and are caused by an asymmetric magnetic field along the pole piece.

The TEM imaging in the is work was carried out using a Jeol 2100 TEM system operating at a voltage of 200 kV. This microscope uses a LaB_6 source which allows operation between 80–200 kV which translates to a maximum high contrast resolution of 0.31 nm.

Scanning Electron Microscopy

Developed after the TEM, scanning electron microscopy (SEM) is another powerful tool for high resolution sample imaging. An SEM operates in a similar manner to a TEM where electrons are focused using electromagnetic lenses onto a sample surface although they typically operate at much lower electron energies (100 eV–50 keV). Once focused, the beam is rastered across the sample surface by modulating the current in the scanning coils, shown in Figure A.5.[256] When the beam strikes the surface, a number of interactions occur within a

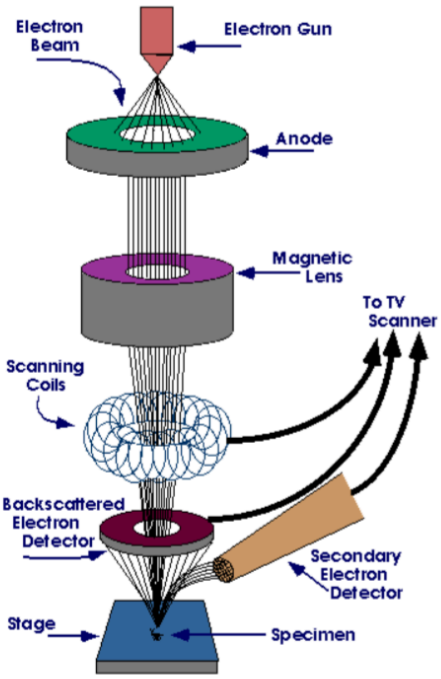

Figure A.5: Schematic of an SEM with its subsystems. Image from Ref. (256).

teardrop-shaped volume at the sample surface which are then used to create the image.[257]

The primary electrons used for imaging are those that are created through ionisation in the interaction volume (secondary electrons) and those that are backscattered. Secondary electrons are typically low energy (< 5 eV) and so only provide information for a thin layer at the sample surface. The secondary electron detector is thus used for creating topographical images. The backscattered electrons are high energy and so provide information from deeper in the interaction volume. These electrons often undergo multiple inelastic scattering events within the sample and so contain information about the sample composition. Heavier elements within a sample will backscatter electrons more strongly than lighter ones meaning regions of different chemical composition can be detected. The

backscattered electrons are not easily absorbed by the sample due to their high energy which means their probe area is larger than that of the secondary electrons. This results in a lower resolution for the backscatter detector compared to the secondary electron detector ($\sim 1\ \mu m$ *vs* 20 nm).[257]

The SEM imagery in this thesis was created with a Carl Zeiss Ultra Plus using a field emission gun as an electron source. As all of the imaging was primarily for inspection, the accelerating voltages were typically < 2 kV.

B

Derivations

B.1 Current Behaviour in a Field-Effect Transistor

To derive the basic characteristics of MOSFET behaviour, some assumptions must first be made to establish homogeneity.

1. The gate/oxide/channel stack behaves like an ideal capacitor, i.e., there are no material defects to act as interface traps, fixed oxide charges, etc.

2. Following 1, there is no interfacial scattering so the carrier mobility is constant throughout the channel.

3. Following 2, the doping is completely uniform throughout the channel.

4. The gate field perpendicular to the channel is much larger than the transverse field between the source and drain.

5. There is no diffusion current so only the drift current is considered.

6. The profile of the potential is linear across the channel (the gradual channel approximation).

The characteristics will be derived for an n-channel FET but are equally valid for a p-channel FET as p can be subbed for n throughout. The various naming conventions are shown in Figures B.1A and B.

Above a threshold voltage, V_T, the concentration of mobile charge carriers that accumulates at the semiconductor/oxide interface is given by

$$Q = -C_{ox}(V_G - V_T) \tag{B.1}$$

where Q is the amount of charge, C_{ox} is the areal capacitance of the oxide, and V_G and V_T are the gate and threshold voltages. Once the drain is biased against the source, the voltage is dropped across the channel such that $V_{ch}(y = 0) = 0$ and $V_{ch}(y = L) = V_{DS}$, shown in Figure B.1B. The charge density along the channel is thus

$$Q(y) = -en_s(y) = -C_{ox}(V_G - V_{ch}(y) - V_T) \tag{B.2}$$

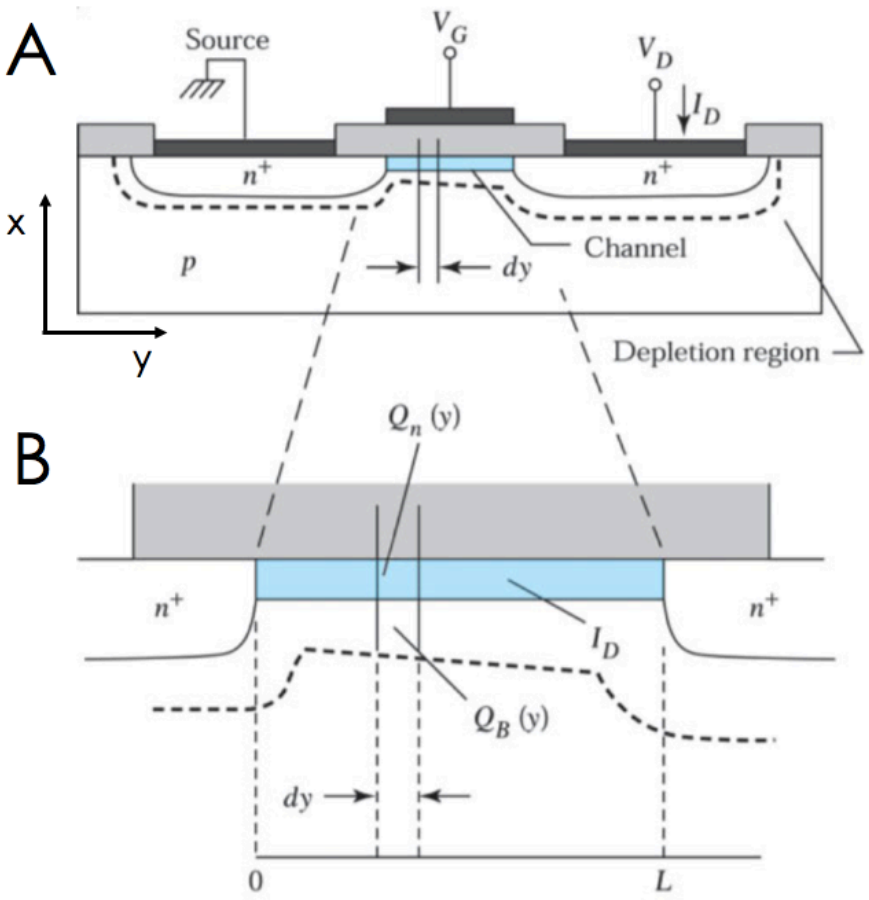

Figure B.1: MOSFET Schematic. A) A schematic representation of a MOSFET used for analysis. B) Magnified view of the channel. Images from Ref. (130).

where e is the elementary charge and n_s is the sheet density in cm^{-2}. The conductivity of the channel at point y is

$$\sigma = qn(x)\mu_n(x) \tag{B.3}$$

where $n(x)$ is the charge density in cm^{-3}, and $\mu_n(x)$ is the electron mobility. Using assumption 2 above, the mobility is constant throughout the channel so, through Ohm's

Law, the channel conductance, g, is given by

$$g = \frac{w}{L}\int_0^x \sigma(x)dx = \frac{w\mu_n}{L}\int_0^x qn(x)dx \tag{B.4}$$

where w is the electrode width and L is the channel length. Integrating the right hand side yields the total charge per unit area in the inversion layer, or $|Q(y)|$, so

$$g = \frac{w\mu_n}{L}|Q(y)| \tag{B.5}$$

The channel resistance per infinitesimal section dy is given by

$$dR = \frac{dy}{gL} = \frac{dy}{w\mu_n|Q(y)|} \tag{B.6}$$

with a corresponding voltage drop across the infinitesimal section given by

$$dV = I_{DS}dR = \frac{I_{DS}dy}{w\mu_n|Q(y)|} \tag{B.7}$$

This expression can now be integrated from $y = 0$ to $y = L$ and from $V_{ch} = 0$ to $V_{ch} = V_{DS}$ such that

$$\int_0^L I_{DS}dy = w\mu_n C_{ox}\int_0^{V_{DS}} (V_G - V_{ch}(y) - V_T)dV \tag{B.8}$$

As the current is constant between the source and drain, the left hand side of Eq B.8 gives L. On the right, the gate and threshold voltages are constant so Eq. B.8 is solved as

$$I_{DS} = \frac{w}{L}\mu_n C_{ox}\left(V_G - V_T - \frac{V_{DS}}{2}\right)V_{DS} \tag{B.9}$$

For a given gate voltage, the drain current initially increases linearly with a drain bias (the linear region) but then gradually saturates (the saturation region). For small drain biases, Eq. B.9 becomes

$$I_{DS} = \frac{w}{L}\mu_n C_{ox}(V_G - V_T)V_{DS} \qquad \text{for } V_{DS} \ll (V_G - V_T) \tag{B.10}$$

For a drain bias greater than the saturation voltage, the voltage drop across the channel is $V_{DS,sat}$ with the remaining voltage, $(V_{DS} - V_{DS,sat})$, dropped across the pinch-off region.

$$I_{DS,sat} = \frac{w}{L}\mu_n C_{ox}\left(V_G - V_T - \frac{V_{DS,sat}}{2}\right)V_{DS,sat} \qquad \text{for } V_{DS} > V_{DS,sat} \tag{B.11}$$

The charge at the end of the channel is zero due to the pinch-off region such that

$$Q(y = L) = -C_{ox}(V_G - V_{DS,sat} - V_T) = 0 \tag{B.12}$$

or

$$V_G - V_T = V_{DS,sat} \tag{B.13}$$

Thus, from Eq. B.11, the saturated current is

$$I_{DS,sat} = \frac{w}{2L}\mu_n C_{ox}(V_G - V_T)^2 \qquad \text{for } V_{DS} > V_{DS,sat} \tag{B.14}$$

Eq. B.10 and Eq. B.14 describe the behaviour in the linear and saturation regimes whose outputs are shown in Figure 3.8B in the main text. The channel conductance, g_D, and

transconductance, g_m, in the linear regime are obtained by taking the derivative of Eq. B.10 with respect to V_{DS} and V_G such that

$$g_D \equiv \left.\frac{\partial I_{DS}}{\partial V_{DS}}\right|_{V_G} = \frac{w}{L}\mu C(V_G - V_T - V_{DS}) \tag{B.15}$$

$$g_m \equiv \left.\frac{\partial I_{DS}}{\partial V_G}\right|_{V_{DS}} = \frac{w}{L}\mu C V_{DS} \tag{B.16}$$

B.2 Mass- and Volume-Fraction Relationships in Percolating Networks

The range of densities across materials means that the mass fraction of a conductive filler is not a useful metric for emerging electrical networks. This means that the mass fraction needs to be converted to the volume fraction as follows. The total volume of the film is the sum of its parts;

$$V_T = V_G + V_M + V_P \tag{B.17}$$

where V_T is the total volume, and V_G, V_M, and V_P are the volumes of the graphene, MoS_2, and the pores respectively. The volume fraction is thus

$$\varphi_i = \frac{V_i}{V_T} = \frac{\mathcal{M}_i}{\mathcal{M}_T}\frac{\varrho_T}{\varrho_i} = \mathcal{M}_{f,i}\frac{\varrho_T}{\varrho_i} \tag{B.18}$$

where $i = G, \mathcal{M}, P$, and $\mathcal{M}_{f,i}$ is its mass fraction. Eq. B.17 can then be restated as

$$\varphi_G + \varphi_M + \varphi_P = 1 \tag{B.19}$$

Through Eq. B.18, this gives

$$\varphi_G + \mathcal{M}_{f,M}\frac{\varrho_T}{\varrho_M} + \varphi_P = 1 \tag{B.20}$$

Using the fact that $\mathcal{M}_{f,G} + \mathcal{M}_{f,M} = 1$, Eq. B.20 becomes

$$\varphi_G + (1 - \mathcal{M}_{f,G})\frac{\varrho_T}{\varrho_M} + \varphi_P = 1 \tag{B.21}$$

Restating Eq. B.18 in terms of ϱ_T, the second term becomes

$$\varphi_G + \varphi_G \frac{(1 - \mathcal{M}_{f,G})}{\mathcal{M}_{f,G}} \frac{\varrho_G}{\varrho_M} + \varphi_p = 1 \tag{B.22}$$

This is rearranged to show the φ_G-dependence as

$$\varphi_G = \frac{(1 - \varphi_p)}{1 + (\mathcal{M}_{f,G}^{-1} - 1)\varrho_G/\varrho_M} \tag{B.23}$$

However, the measurement of the film porosity, φ_p, is non-trivial meaning this equation cannot be used directly to transform $\mathcal{M}_{f,G}$ into φ_G. This is resolved through the reduced volume fraction

$$\frac{(\varphi_C - \varphi_G)}{\varphi_C} \tag{B.24}$$

where φ_C is the volume fraction of the percolation threshold. This is used with Eq. B.23 to remove the porosity variable as

$$\frac{(\varphi_C - \varphi_G)}{\varphi_C} = \frac{\dfrac{(1 - \varphi_p)}{1 + (\mathcal{M}_{f,C}^{-1} - 1)\varrho_G/\varrho_M} - \dfrac{(1 - \varphi_p)}{1 + (\mathcal{M}_{f,G}^{-1} - 1)\varrho_G/\varrho_M}}{\dfrac{(1 - \varphi_p)}{1 + (\mathcal{M}_{f,C}^{-1} - 1)\varrho_G/\varrho_M}} \tag{B.25}$$

where $\mathcal{M}_{f,C}$ is the mass fraction of the percolation threshold. The common numerator, $1 - \varphi_p$, now cancels leaving

$$\frac{(\varphi_C - \varphi_G)}{\varphi_C} = 1 - \frac{1 + (\mathcal{M}_{f,C}^{-1} - 1)\varrho_G/\varrho_M}{1 + (\mathcal{M}_{f,G}^{-1} - 1)\varrho_G/\varrho_M} \tag{B.26}$$

Combining terms, this becomes

$$\frac{(\varphi_C - \varphi_G)}{\varphi_C} = \frac{(\mathcal{M}_{f,G}^{-1} - 1)\varrho_G/\varrho_M - (\mathcal{M}_{f,C}^{-1} - 1)\varrho_G/\varrho_M}{1 + (\mathcal{M}_{f,G}^{-1} - 1)\varrho_G/\varrho_M} \tag{B.27}$$

Dividing through by ϱ_M/ϱ_G gives

$$\frac{(\varphi_C - \varphi_G)}{\varphi_C} = \frac{\mathcal{M}_{f,G}^{-1} - \mathcal{M}_{f,C}^{-1}}{\varrho_M/\varrho_G + (\mathcal{M}_{f,G}^{-1} - 1)} \tag{B.28}$$

And then dividing through by $\mathcal{M}_{f,G}$ gives

$$\frac{(\varphi_C - \varphi_G)}{\varphi_C} = \frac{1 - \mathcal{M}_{f,G}/\mathcal{M}_{f,C}}{\mathcal{M}_{f,G}\varrho_M/\varrho_G + 1 - \mathcal{M}_{f,G}} \tag{B.29}$$

Finally, collecting terms gives

$$\frac{(\varphi_C - \varphi_G)}{\varphi_C} = \frac{1 - \mathcal{M}_{f,G}/\mathcal{M}_{f,C}}{1 + \mathcal{M}_{f,G}(\varrho_M/\varrho_G - 1)} \tag{B.30}$$

This equation relies on the assumption that the porosity does not change with volume fraction, which should hold true when both the filler and matrix have similar geometries.

References

[1] D. Schaming and H. Remita, "Nanotechnology: from the ancient time to nowadays," *Foundations of Chemistry*, vol. 17, no. 3, pp. 187–205, 2015.

[2] A. C. Ferrari, F. Bonaccorso, V. Fal'Ko, K. S. Novoselov, S. Roche, P. Bøggild, S. Borini, F. H. Koppens, V. Palermo, N. Pugno, *et al.*, "Science and technology roadmap for graphene, related two-dimensional crystals, and hybrid systems," *Nanoscale*, vol. 7, no. 11, pp. 4598–4810, 2015.

[3] P. R. Wallace, "The band theory of graphite," *Physical Review*, vol. 71, no. 9, pp. 622–634, 1947.

[4] R. D. Heidenreich, W. M. Hess, and L. L. Ban, "A test object and criteria for high resolution electron microscopy," *Journal of Applied Crystallography*, vol. 1, no. 1, pp. 1–19, 1968.

[5] K. S. Novoselov, A. K. Geim, S. V. Morozov, D. Jiang, Y. Zhang, S. V. Dubonos, I. V. Grigorieva, and A. A. Firsov, "Electric field effect in atomically thin carbon films," *Science*, vol. 306, no. 5696, pp. 666–669, 2004.

[6] A. K. Geim and K. S. Novoselov, "The rise of graphene," *Nat Mater*, vol. 6, no. 3, pp. 183–91, 2007.

[7] U. Dahmen, R. Erni, V. Radmilovic, C. Ksielowski, M.-D. Rossell, and P. Denes, "Background, status and future of the transmission electron aberration-corrected microscope project," *Philosophical Transactions of the Royal Society of London A: Mathematical, Physical and Engineering Sciences*, vol. 367, no. 1903, pp. 3795–3808, 2009.

[8] A. H. Castro Neto, F. Guinea, N. M. R. Peres, K. S. Novoselov, and A. K. Geim, "The electronic properties of graphene," *Reviews of Modern Physics*, vol. 81, no. 1, pp. 109–162, 2009.

[9] V. K. Sangwan and M. C. Hersam, "Electronic transport in two-dimensional materials," *Annual Review of Physical Chemistry*, vol. 69, no. 1, pp. 299–325, 2018.

[10] A. Celzard, J. Mareche, G. Furdin, and S. Puricelli, "Electrical conductivity of anisotropic expanded graphite-based monoliths," *Journal of Physics D: Applied Physics*, vol. 33, no. 23, p. 3094, 2000.

[11] P. J. Zomer, S. P. Dash, N. Tombros, and B. J. van Wees, "A transfer technique for high mobility graphene devices on commercially available hexagonal boron nitride," *Applied Physics Letters*, vol. 99, no. 23, 2011.

[12] C. S. Boland, U. Khan, G. Ryan, S. Barwich, R. Charifou, A. Harvey, C. Backes, Z. Li, M. S. Ferreira, M. E. Mobius, R. J. Young, and J. N. Coleman, "Sensitive electromechanical sensors using viscoelastic graphene-polymer nanocomposites," *Science*, vol. 354, no. 6317, pp. 1257–1260, 2016.

[13] K. S. Novoselov, D. Jiang, F. Schedin, T. J. Booth, V. V. Khotkevich, S. V. Morozov, and A. K. Geim, "Two-dimensional atomic crystals," *Proc Natl Acad Sci U S A*, vol. 102, no. 30, pp. 10451–3, 2005.

[14] R. G. Dickinson and L. Pauling, "The crystal structure of molybdenite," *Journal of the American Chemical Society*, vol. 45, no. 6, pp. 1466–1471, 1923.

[15] M. Chhowalla, H. S. Shin, G. Eda, L. J. Li, K. P. Loh, and H. Zhang, "The chemistry of two-dimensional layered transition metal dichalcogenide nanosheets," *Nature Chemistry*, vol. 5, no. 4, pp. 263–275, 2013.

[16] B. Radisavljevic, A. Radenovic, J. Brivio, i. V. Giacometti, and A. Kis, "Single-layer mos 2 transistors," *Nature nanotechnology*, vol. 6, no. 3, p. 147, 2011.

[17] Q. Liu, X. Li, Q. He, A. Khalil, D. Liu, T. Xiang, X. Wu, and L. Song, "Gram-scale aqueous synthesis of stable few-layered 1t-mos2: Applications for visible-light-driven photocatalytic hydrogen evolution," *Small*, vol. 11, no. 41, pp. 5556–5564, 2015.

[18] H. Schmidt, F. Giustiniano, and G. Eda, "Electronic transport properties of transition metal dichalcogenide field-effect devices: surface and interface effects," *Chemical Society Reviews*, vol. 44, no. 21, pp. 7715–7736, 2015.

[19] J. Kang, S. Tongay, J. Zhou, J. Li, and J. Wu, "Band offsets and heterostructures of two-dimensional semiconductors," *Applied Physics Letters*, vol. 102, no. 1, p. 012111, 2013.

[20] A. Kuc, N. Zibouche, and T. Heine, "Influence of quantum confinement on the electronic structure of the transition metal sulfidets2," *Physical Review B*, vol. 83, no. 24, 2011.

[21] K. F. Mak, C. Lee, J. Hone, J. Shan, and T. F. Heinz, "Atomically thin mos 2: a new direct-gap semiconductor," *Physical review letters*, vol. 105, no. 13, p. 136805, 2010.

[22] M.-L. Tsai, S.-H. Su, J.-K. Chang, D.-S. Tsai, C.-H. Chen, C.-I. Wu, L.-J. Li, L.-J. Chen, and J.-H. He, "Monolayer mos2 heterojunction solar cells," *ACS Nano*, vol. 8, no. 8, pp. 8317–8322, 2014.

[23] Z. Yin, H. Li, H. Li, L. Jiang, Y. Shi, Y. Sun, G. Lu, Q. Zhang, X. Chen, and H. Zhang, "Single-layer mos2 phototransistors," *ACS Nano*, vol. 6, no. 1, pp. 74–80, 2011.

[24] S. Mouri, Y. Miyauchi, and K. Matsuda, "Tunable photoluminescence of monolayer mos2 via chemical doping," *Nano Letters*, vol. 13, no. 12, pp. 5944–5948, 2013.

[25] J. Hong, Z. Hu, M. Probert, K. Li, D. Lv, X. Yang, L. Gu, N. Mao, Q. Feng, L. Xie, J. Zhang, D. Wu, Z. Zhang, C. Jin, W. Ji, X. Zhang, J. Yuan, and Z. Zhang, "Exploring atomic defects in molybdenum disulphide monolayers," *Nat Commun*, vol. 6, p. 6293, 2015.

[26] S. McDonnell, R. Addou, C. Buie, R. M. Wallace, and C. L. Hinkle, "Defect-dominated doping and contact resistance in mos2," *ACS Nano*, vol. 8, no. 3, pp. 2880–8, 2014.

[27] A. Allain and A. Kis, "Electron and hole mobilities in single-layer wse2," *ACS Nano*, vol. 8, no. 7, pp. 7180–7185, 2014.

[28] A. T. Hanbicki, M. Currie, G. Kioseoglou, A. L. Friedman, and B. T. Jonker, "Measurement of high exciton binding energy in the monolayer transition-metal dichalcogenides ws2 and wse2," *Solid State Communications*, vol. 203, pp. 16–20, 2015.

[29] D. Lembke and A. Kis, "Breakdown of high-performance monolayer mos2 transistors," *ACS Nano*, vol. 6, no. 11, pp. 10070–5, 2012.

[30] S. Das, H.-Y. Chen, A. V. Penumatcha, and J. Appenzeller, "High performance multilayer mos2 transistors with scandium contacts," *Nano Letters*, vol. 13, no. 1, pp. 100–105, 2013.

[31] A. Harvey, J. B. Boland, I. Godwin, A. G. Kelly, B. M. Szydłowska, G. Murtaza, A. Thomas, D. J. Lewis, P. O'Brien, and J. N. Coleman, "Exploring the versatility of liquid phase exfoliation: producing 2d nanosheets from talcum powder, cat litter and beach sand," *2D Materials*, vol. 4, no. 2, p. 025054, 2017.

[32] L. F. Dobrzhinetskaya, R. Wirth, J. Yang, H. W. Green, I. D. Hutcheon, P. K. Weber, and E. S. Grew, "Qingsongite, natural cubic boron nitride: The first boron mineral from the earth's mantle," *American Mineralogist*, vol. 99, no. 4, pp. 764–772, 2014.

[33] M. Engler, C. Lesniak, R. Damasch, B. Ruisinger, and J. Eichler, "Hexagonal boron nitride (hbn) - applications from metallurgy to cosmetics," *Cfi-Ceramic Forum International*, vol. 84, no. 12, pp. E49–E53, 2007.

[34] D. Golberg, Y. Bando, Y. Huang, T. Terao, M. Mitome, C. Tang, and C. Zhi, "Boron nitride nanotubes and nanosheets," *ACS Nano*, vol. 4, no. 6, pp. 2979–2993, 2010.

[35] N. G. Chopra, R. J. Luyken, K. Cherrey, V. H. Crespi, M. L. Cohen, S. G. Louie, and A. Zettl, "Boron nitride nanotubes," *Science*, vol. 269, no. 5226, pp. 966–7, 1995.

[36] M. Topsakal, E. Akturk, and S. Ciraci, "First-principles study of two- and one-dimensional honeycomb structures of boron nitride," *Physical Review B*, vol. 79, no. 11, 2009.

[37] G. Cassabois, P. Valvin, and B. Gil, "Hexagonal boron nitride is an indirect bandgap semiconductor," *Nature Photonics*, vol. 10, no. 4, pp. 262–+, 2016.

[38] A. Pakdel, Y. Bando, and D. Golberg, "Nano boron nitride flatland," *Chem Soc Rev*, vol. 43, no. 3, pp. 934–59, 2014.

[39] N. Marom, J. Bernstein, J. Garel, A. Tkatchenko, E. Joselevich, L. Kronik, and O. Hod, "Stacking and registry effects in layered materials: The case of hexagonal boron nitride," *Physical Review Letters*, vol. 105, no. 4, 2010.

[40] A. Pakdel, C. Zhi, Y. Bando, and D. Golberg, "Low-dimensional boron nitride nanomaterials," *Materials Today*, vol. 15, no. 6, pp. 256–265, 2012.

[41] C. R. Dean, A. F. Young, I. Meric, C. Lee, L. Wang, S. Sorgenfrei, K. Watanabe, T. Taniguchi, P. Kim, K. L. Shepard, and J. Hone, "Boron nitride substrates for high-quality graphene electronics," *Nature Nanotechnology*, vol. 5, no. 10, pp. 722–726, 2010.

[42] A. S. Mayorov, R. V. Gorbachev, S. V. Morozov, L. Britnell, R. Jalil, L. A. Ponomarenko, P. Blake, K. S. Novoselov, K. Watanabe, T. Taniguchi, and A. K. Geim, "Micrometer-scale ballistic transport in encapsulated graphene at room temperature," *Nano Letters*, vol. 11, no. 6, pp. 2396–2399, 2011.

[43] M. R. Laskar, L. Ma, S. Kannappan, P. Sung Park, S. Krishnamoorthy, D. N. Nath, W. Lu, Y. Wu, and S. Rajan, "Large area single crystal (0001) oriented mos2," *Applied Physics Letters*, vol. 102, no. 25, p. 252108, 2013.

[44] V. L. Nguyen, D. J. Perello, S. Lee, C. T. Nai, B. G. Shin, J.-G. Kim, H. Y. Park, H. Y. Jeong, J. Zhao, Q. A. Vu, S. H. Lee, K. P. Loh, S.-Y. Jeong, and Y. H. Lee, "Wafer-scale single-crystalline ab-stacked bilayer graphene," *Advanced Materials*, vol. 28, no. 37, pp. 8177–8183, 2016.

[45] Y. Kim, A. R. Kim, G. Zhao, S. Y. Choi, S. C. Kang, S. K. Lim, K. E. Lee, J. Park, B. H. Lee, M. G. Hahm, D. H. Kim, J. Yun, K. H. Lee, and B. Cho, "Wafer-scale integration of highly uniform and scalable mos2 transistors," *ACS Appl Mater Interfaces*, vol. 9, no. 42, pp. 37146–37153, 2017.

[46] K. Kang, S. Xie, L. Huang, Y. Han, P. Y. Huang, K. F. Mak, C. J. Kim, D. Muller, and J. Park, "High-mobility three-atom-thick semiconducting films with wafer-scale homogeneity," *Nature*, vol. 520, no. 7549, pp. 656–60, 2015.

[47] C.-M. Seah, S.-P. Chai, and A. R. Mohamed, "Mechanisms of graphene growth by chemical vapour deposition on transition metals," *Carbon*, vol. 70, pp. 1–21, 2014.

[48] S. Xie, O. M. Istrate, P. May, S. Barwich, A. P. Bell, U. Khan, and J. N. Coleman, "Boron nitride nanosheets as barrier enhancing fillers in melt processed composites," *Nanoscale*, vol. 7, no. 10, pp. 4443–4450, 2015.

[49] R. Saggar, H. Porwal, P. Tatarko, I. Dlouhý, and M. J. Reece, "Boron nitride nanosheets reinforced glass matrix composites," *Advances in Applied Ceramics*, vol. 114, no. sup1, pp. S26–S33, 2015.

[50] R. F. Frindt, "Single crystals of mos2 several molecular layers thick," *Journal of Applied Physics*, vol. 37, no. 4, pp. 1928–1929, 1966.

[51] C. Backes, K. R. Paton, D. Hanlon, S. Yuan, M. I. Katsnelson, J. Houston, R. J. Smith, D. McCloskey, J. F. Donegan, and J. N. Coleman, "Spectroscopic metrics allow in situ measurement of mean size and thickness of liquid-exfoliated few-layer graphene nanosheets," *Nanoscale*, vol. 8, no. 7, pp. 4311–23, 2016.

[52] C. Backes, B. M. Szydlowska, A. Harvey, S. J. Yuan, V. Vega-Mayoral, B. R. Davies, P. L. Zhao, D. Hanlon, E. J. G. Santos, M. I. Katsnelson, W. J. Blau, C. Gadermaier, and J. N. Coleman, "Production of highly monolayer enriched dispersions of liquid-exfoliated nanosheets by liquid cascade centrifugation," *Acs Nano*, vol. 10, no. 1, pp. 1589–1601, 2016.

[53] F. Torrisi, T. Hasan, W. Wu, Z. Sun, A. Lombardo, T. S. Kulmala, G.-W. Hsieh, S. Jung, F. Bonaccorso, P. J. Paul, D. Chu, and A. C. Ferrari, "Inkjet-printed graphene electronics," *ACS Nano*, vol. 6, no. 4, pp. 2992–3006, 2012.

[54] Q. He, Z. Zeng, Z. Yin, H. Li, S. Wu, X. Huang, and H. Zhang, "Fabrication of flexible mos2 thin-film transistor arrays for practical gas-sensing applications," *Small*, vol. 8, no. 19, pp. 2994–9, 2012.

[55] A. G. Kelly, D. Finn, A. Harvey, T. Hallam, and J. N. Coleman, "All-printed capacitors from graphene-bn-graphene nanosheet heterostructures," *Applied Physics Letters*, vol. 109, no. 2, 2016.

[56] B. C. Brodie, "On the atomic weight of graphite," *Philosophical Transactions of the Royal Society of London*, vol. 149, no. 0, pp. 249–259, 1859.

[57] W. S. Hummers and R. E. Offeman, "Preparation of graphitic oxide," *Journal of the American Chemical Society*, vol. 80, no. 6, pp. 1339–1339, 1958.

[58] F. Bonaccorso, A. Lombardo, T. Hasan, Z. Sun, L. Colombo, and A. C. Ferrari, "Production and processing of graphene and 2d crystals," *Materials Today*, vol. 15, no. 12, pp. 564–589, 2012.

[59] W. Gao, "The chemistry of graphene oxide," in *Graphene oxide*, pp. 61–95, Springer, 2015.

[60] A. Penicaud and C. Drummond, "Deconstructing graphite: graphenide solutions," *Acc Chem Res*, vol. 46, no. 1, pp. 129–37, 2013.

[61] G. Eda, H. Yamaguchi, D. Voiry, T. Fujita, M. Chen, and M. Chhowalla, "Photoluminescence from chemically exfoliated mos2," *Nano Lett*, vol. 11, no. 12, pp. 5111–6, 2011.

[62] Y. Hernandez, V. Nicolosi, M. Lotya, F. M. Blighe, Z. Y. Sun, S. De, I. T. McGovern, B. Holland, M. Byrne, Y. K. Gun'ko, J. J. Boland, P. Niraj, G. Duesberg, S. Krishnamurthy, R. Goodhue, J. Hutchison, V. Scardaci, A. C. Ferrari, and

J. N. Coleman, "High-yield production of graphene by liquid-phase exfoliation of graphite," *Nature Nanotechnology*, vol. 3, no. 9, pp. 563–568, 2008.

[63] K. R. Paton, E. Varrla, C. Backes, R. J. Smith, U. Khan, A. O'Neill, C. Boland, M. Lotya, O. M. Istrate, P. King, T. Higgins, S. Barwich, P. May, P. Puczkarski, I. Ahmed, M. Moebius, H. Pettersson, E. Long, J. Coelho, S. E. O'Brien, E. K. McGuire, B. M. Sanchez, G. S. Duesberg, N. McEvoy, T. J. Pennycook, C. Downing, A. Crossley, V. Nicolosi, and J. N. Coleman, "Scalable production of large quantities of defect-free few-layer graphene by shear exfoliation in liquids," *Nature Materials*, vol. 13, no. 6, pp. 624–630, 2014.

[64] J. N. Coleman, "Liquid exfoliation of defect-free graphene," *Acc Chem Res*, vol. 46, no. 1, pp. 14–22, 2013.

[65] D. McManus, S. Vranic, F. Withers, V. Sanchez-Romaguera, M. Macucci, H. Yang, R. Sorrentino, K. Parvez, S.-K. Son, G. Iannaccone, K. Kostarelos, G. Fiori, and C. Casiraghi, "Water-based and biocompatible 2d crystal inks for all-inkjet-printed heterostructures," *Nature Nanotechnology*, vol. 12, no. 4, pp. 343–350, 2017.

[66] E. B. Secor, S. Lim, H. Zhang, C. D. Frisbie, L. F. Francis, and M. C. Hersam, "Gravure printing of graphene for large-area flexible electronics," *Advanced Materials*, vol. 26, no. 26, pp. 4533–+, 2014.

[67] C. Backes, T. M. Higgins, A. Kelly, C. Boland, A. Harvey, D. Hanlon, and J. N. Coleman, "Guidelines for exfoliation, characterization and processing of layered materials produced by liquid exfoliation," *Chemistry of Materials*, vol. 29, no. 1, pp. 243–255, 2016.

[68] F. Bonaccorso, A. Bartolotta, J. N. Coleman, and C. Backes, "2d-crystal-based functional inks," *Advanced Materials*, vol. 28, no. 29, pp. 6136–6166, 2016.

[69] P. May, U. Khan, J. M. Hughes, and J. N. Coleman, "Role of solubility parameters in understanding the steric stabilization of exfoliated two-dimensional nanosheets by adsorbed polymers," *The Journal of Physical Chemistry C*, vol. 116, no. 20, pp. 11393–11400, 2012.

[70] P. Lynch, U. Khan, A. Harvey, I. Ahmed, and J. N. Coleman, "Graphene-mos2 nanosheet composites as electrodes for dye sensitised solar cells," *Materials Research Express*, vol. 3, no. 3, p. 035007, 2016.

[71] T. J. Mason, *Practical sonochemistry : user's guide to applications in chemistry and chemical engineering*. Ellis Horwood series in organic chemistry, New York: E. Horwood, 1991.

[72] T. J. Mason and J. P. Lorimer, *Applied sonochemistry : the uses of power ultrasound in chemistry and processing*. Weinheim: Wiley-VCH, 2001.

[73] S. Sorel, U. Khan, and J. N. Coleman, "Flexible, transparent dielectric capacitors with nanostructured electrodes," *Applied Physics Letters*, vol. 101, no. 10, p. 103106, 2012.

[74] Y. Hernandez, V. Nicolosi, M. Lotya, F. M. Blighe, Z. Y. Sun, S. De, I. T. McGovern, B. Holland, M. Byrne, Y. K. Gun'ko, J. J. Boland, P. Niraj, G. Duesberg, S. Krishnamurthy, R. Goodhue, J. Hutchison, V. Scardaci, A. C. Ferrari, and J. N. Coleman, "High-yield production of graphene by liquid-phase exfoliation of graphite," *Nature Nanotechnology*, vol. 3, no. 9, pp. 563–568, 2008.

[75] U. Khan, A. O'Neill, M. Lotya, S. De, and J. N. Coleman, "High-concentration solvent exfoliation of graphene," *Small*, vol. 6, no. 7, pp. 864–871, 2010.

[76] J. Hassoun, F. Bonaccorso, M. Agostini, M. Angelucci, M. G. Betti, R. Cingolani, M. Gemmi, C. Mariani, S. Panero, V. Pellegrini, and B. Scrosati, "An advanced lithium-ion battery based on a graphene anode and a lithium iron phosphate cathode," *Nano Lett*, vol. 14, no. 8, pp. 4901–6, 2014.

[77] A. Capasso, A. E. Del Rio Castillo, H. Sun, A. Ansaldo, V. Pellegrini, and F. Bonaccorso, "Ink-jet printing of graphene for flexible electronics: An environmentally-friendly approach," *Solid State Communications*, vol. 224, pp. 53–63, 2015.

[78] V. Nicolosi, M. Chhowalla, M. G. Kanatzidis, M. S. Strano, and J. N. Coleman, "Liquid exfoliation of layered materials," *Science*, vol. 340, no. 6139, p. 1226419, 2013.

[79] S. D. Bergin, V. Nicolosi, P. V. Streich, S. Giordani, Z. Sun, A. H. Windle, P. Ryan, N. P. P. Niraj, Z.-T. T. Wang, L. Carpenter, W. J. Blau, J. J. Boland, J. P. Hamilton, and J. N. Coleman, "Towards solutions of single-walled carbon nanotubes in common solvents," *Advanced Materials*, vol. 20, no. 10, pp. 1876–1881, 2008.

[80] Y. Hernandez, M. Lotya, D. Rickard, S. D. Bergin, and J. N. Coleman, "Measurement of multicomponent solubility parameters for graphene facilitates solvent discovery," *Langmuir*, vol. 26, no. 5, pp. 3208–3213, 2010.

[81] S. P. Ogilvie, M. J. Large, G. Fratta, M. Meloni, R. Canton-Vitoria, N. Tagmatarchis, F. Massuyeau, C. P. Ewels, A. A. K. King, and A. B. Dalton, "Considerations for spectroscopy of liquid-exfoliated 2d materials: emerging photoluminescence of n-methyl-2-pyrrolidone," *Scientific Reports*, vol. 7, no. 1, 2017.

[82] H. C. Yau, M. K. Bayazit, J. H. G. Steinke, and M. S. P. Shaffer, "Sonochemical degradation of n-methylpyrrolidone and its influence on single walled carbon nanotube dispersion," *Chemical Communications*, vol. 51, no. 93, pp. 16621–16624, 2015.

[83] A. G. Kelly, T. Hallam, C. Backes, A. Harvey, A. S. Esmaeily, I. Godwin, J. Coelho, V. Nicolosi, J. Lauth, A. Kulkarni, S. Kinge, L. D. A. Siebbeles, G. S. Duesberg, and J. N. Coleman, "All-printed thin-film transistors from networks of liquid-exfoliated nanosheets," *Science*, vol. 356, no. 6333, pp. 69–72, 2017.

[84] M. S. Arnold, A. A. Green, J. F. Hulvat, S. I. Stupp, and M. C. Hersam, "Sorting carbon nanotubes by electronic structure using density differentiation," *Nature Nanotechnology*, vol. 1, no. 1, pp. 60–65, 2006.

[85] "Ancient pigments." http://www.webexhibits.org/pigments/intro/early.html. Accessed: 20-07-18.

[86] Q. H. Wang, K. Kalantar-Zadeh, A. Kis, J. N. Coleman, and M. S. Strano, "Electronics and optoelectronics of two-dimensional transition metal dichalcogenides," *Nature nanotechnology*, vol. 7, no. 11, p. 699, 2012.

[87] I. M. Hutchings and G. Martin, *Inkjet technology for digital fabrication*. Chichester, West Sussex, United Kingdom: Wiley, 2013.

[88] N. J. Nielsen, "History of thinkjet printhead development," *Hewlett-Packard Journal*, vol. 36, no. 5, pp. 4–10, 1985.

[89] S. D. Hoath, *Fundamentals of inkjet printing: the science of inkjet and droplets*. John Wiley & Sons, 2016.

[90] J. O. O. v. Niessen, J. N. Schaper, J. H. Petersen, and N. H. Bings, "Development and characterization of a thermal inkjet-based aerosol generator for micro-volume sample introduction in analytical atomic spectrometry," *Journal of Analytical Atomic Spectrometry*, vol. 26, no. 9, pp. 1781–1789, 2011.

[91] S. I. Zoltan, "Pulsed droplet ejecting system," Aug. 8 1972. US Patent 3,683,212.

[92] B. Derby, "Inkjet printing of functional and structural materials: fluid property requirements, feature stability, and resolution," *Annual Review of Materials Research*, vol. 40, pp. 395–414, 2010.

[93] G. Hu, J. Kang, L. W. Ng, X. Zhu, R. C. Howe, C. G. Jones, M. C. Hersam, and T. Hasan, "Functional inks and printing of two-dimensional materials," *Chemical Society Reviews*, vol. 47, no. 9, pp. 3265–3300, 2018.

[94] B. Derby, "Inkjet printing of functional and structural materials: fluid property requirements, feature stability, and resolution," *Annual Review of Materials Research*, vol. 40, pp. 395–414, 2010.

[95] M. Mikolajek, A. Friedrich, W. Bauer, and J. Binder, "Requirements to ceramic suspensions for inkjet printing," in *Ceram. Forum Int*, vol. 92, pp. E25–E29, 2015.

[96] H. Hu and R. G. Larson, "Marangoni effect reverses coffee-ring depositions," *The Journal of Physical Chemistry B*, vol. 110, no. 14, pp. 7090–7094, 2006.

[97] B.-J. de Gans and U. S. Schubert, "Inkjet printing of well-defined polymer dots and arrays," *Langmuir*, vol. 20, no. 18, pp. 7789–7793, 2004.

[98] J. Kettle, T. Lamminmäki, and P. Gane, "A review of modified surfaces for high speed inkjet coating," *Surface and coatings Technology*, vol. 204, no. 12-13, pp. 2103–2109, 2010.

[99] M. Pack, H. Hu, D.-O. Kim, X. Yang, and Y. Sun, "Colloidal drop deposition on porous substrates: competition among particle motion, evaporation, and infiltration," *Langmuir*, vol. 31, no. 29, pp. 7953–7961, 2015.

[100] H. Tan, "Absorption of picoliter droplets by thin porous substrates," *AIChE Journal*, vol. 63, no. 5, pp. 1690–1703, 2017.

[101] J. M. Parramon and M. Ferron, *The Big Book of Airbrush Techniques and Materials*, vol. 1. Watson-Guptill, 1994.

[102] P. N. Nirmalraj, P. E. Lyons, S. De, J. N. Coleman, and J. J. Boland, "Electrical connectivity in single-walled carbon nanotube networks," *Nano letters*, vol. 9, no. 11, pp. 3890–3895, 2009.

[103] D. J. Lipomi, M. Vosgueritchian, B. C. Tee, S. L. Hellstrom, J. A. Lee, C. H. Fox, and Z. Bao, "Skin-like pressure and strain sensors based on transparent elastic films of carbon nanotubes," *Nature nanotechnology*, vol. 6, no. 12, p. 788, 2011.

[104] V. Scardaci, R. Coull, P. E. Lyons, D. Rickard, and J. N. Coleman, "Spray deposition of highly transparent, low-resistance networks of silver nanowires over large areas," *Small*, vol. 7, no. 18, pp. 2621–2628, 2011.

[105] Y. Dong and B. Pan, "A review of speckle pattern fabrication and assessment for digital image correlation," *Experimental Mechanics*, vol. 57, no. 8, pp. 1161–1181, 2017.

[106] X. Shen, C.-M. Ho, and T.-S. Wong, "Minimal size of coffee ring structure," *The Journal of Physical Chemistry B*, vol. 114, no. 16, pp. 5269–5274, 2010.

[107] T. Carey, S. Cacovich, G. Divitini, J. Ren, A. Mansouri, J. M. Kim, C. Wang, C. Ducati, R. Sordan, and F. Torrisi, "Fully inkjet-printed two-dimensional material field-effect heterojunctions for wearable and textile electronics," *Nature Communications*, vol. 8, no. 1, p. 1202, 2017.

[108] Y. Chen, D. T. Shaw, and L. Guo, "Field emission of different oriented carbon nanotubes," *Applied Physics Letters*, vol. 76, no. 17, pp. 2469–2471, 2000.

[109] P.-G. De Gennes, "Wetting: statics and dynamics," *Reviews of modern physics*, vol. 57, no. 3, p. 827, 1985.

[110] J. N. Coleman, S. Curran, A. B. Dalton, A. P. Davey, B. McCarthy, W. Blau, and R. C. Barklie, "Percolation-dominated conductivity in a conjugated-polymer-carbon-nanotube composite," *Physical Review B*, vol. 58, no. 12, pp. R7492–R7495, 1998.

[111] J. K. W. Sandler, J. E. Kirk, I. A. Kinloch, M. S. P. Shaffer, and A. H. Windle, "Ultra-low electrical percolation threshold in carbon-nanotube-epoxy composites," *Polymer*, vol. 44, no. 19, pp. 5893–5899, 2003.

[112] W. Bauhofer and J. Z. Kovacs, "A review and analysis of electrical percolation in carbon nanotube polymer composites," *Composites Science and Technology*, vol. 69, no. 10, pp. 1486–1498, 2009.

[113] J. Wu and D. McLachlan, "Percolation exponents and thresholds obtained from the nearly ideal continuum percolation system graphite-boron nitride," *Physical Review B*, vol. 56, no. 3, p. 1236, 1997.

[114] J. N. Coleman, S. Curran, A. Dalton, A. Davey, B. McCarthy, W. Blau, and R. Barklie, "Percolation-dominated conductivity in a conjugated-polymer-carbon-nanotube composite," *Physical Review B*, vol. 58, no. 12, p. R7492, 1998.

[115] S. Santra, G. Hu, R. Howe, A. De Luca, S. Ali, F. Udrea, J. Gardner, S. Ray, P. Guha, and T. Hasan, "Cmos integration of inkjet-printed graphene for humidity sensing," *Scientific reports*, vol. 5, p. 17374, 2015.

[116] E. B. Secor, T. Z. Gao, A. E. Islam, R. Rao, S. G. Wallace, J. Zhu, K. W. Putz, B. Maruyama, and M. C. Hersam, "Enhanced conductivity, adhesion, and environmental stability of printed graphene inks with nitrocellulose," *Chemistry of Materials*, vol. 29, no. 5, pp. 2332–2340, 2017.

[117] G. Hu, T. Albrow-Owen, X. Jin, A. Ali, Y. Hu, R. C. Howe, K. Shehzad, Z. Yang, X. Zhu, and R. I. Woodward, "Black phosphorus ink formulation for inkjet printing of optoelectronics and photonics," *Nature communications*, vol. 8, no. 1, p. 278, 2017.

[118] C. W. Foster, M. P. Down, Y. Zhang, X. Ji, S. J. Rowley-Neale, G. C. Smith, P. J. Kelly, and C. E. Banks, "3d printed graphene based energy storage devices," *Scientific Reports*, vol. 7, p. 42233, 2017.

[119] W. J. Hyun, E. B. Secor, C. Kim, M. C. Hersam, L. F. Francis, and C. D. Frisbie, "Scalable, self-aligned printing of flexible graphene micro-supercapacitors," *Advanced Energy Materials*, vol. 7, no. 17, 2017.

[120] T. Juntunen, H. Jussila, M. Ruoho, S. Liu, G. Hu, T. Albrow-Owen, L. W. Ng, R. C. Howe, T. Hasan, and Z. Sun, "Inkjet printed large-area flexible few-layer graphene thermoelectrics," *Advanced Functional Materials*, vol. 28, no. 22, p. 1800480, 2018.

[121] P. Horowitz and W. Hill, *The art of electronics*. Cambridge Univ. Press, 1989.

[122] "Introduction to capacitors." https://www.electronics-tutorials.ws/capacitor/cap_1.htmlv. Accessed: 30-07-18.

[123] N. Perea-López, A. L. Elías, A. Berkdemir, A. Castro-Beltran, H. R. Gutiérrez, S. Feng, R. Lv, T. Hayashi, F. López-Urías, and S. Ghosh, "Photosensor device based on few-layered ws2 films," *Advanced Functional Materials*, vol. 23, no. 44, pp. 5511–5517, 2013.

[124] C. Yim, M. O'brien, N. McEvoy, S. Riazimehr, H. Schäfer-Eberwein, A. Bablich, R. Pawar, G. Iannaccone, C. Downing, and G. Fiori, "Heterojunction hybrid devices from vapor phase grown mos 2," *Scientific reports*, vol. 4, p. 5458, 2014.

[125] M. Shanmugam, C. A. Durcan, and B. Yu, "Layered semiconductor molybdenum disulfide nanomembrane based schottky-barrier solar cells," *Nanoscale*, vol. 4, no. 23, pp. 7399–7405, 2012.

[126] M. Shanmugam, T. Bansal, C. A. Durcan, and B. Yu, "Schottky-barrier solar cell based on layered semiconductor tungsten disulfide nanofilm," *Applied Physics Letters*, vol. 101, no. 26, p. 263902, 2012.

[127] G. Cunningham, D. Hanlon, N. McEvoy, G. S. Duesberg, and J. N. Coleman, "Large variations in both dark- and photoconductivity in nanosheet networks as nanomaterial is varied from mos2 to wte2," *Nanoscale*, vol. 7, no. 1, pp. 198–208, 2014.

[128] M. Bernardi, M. Palummo, and J. C. Grossman, "Extraordinary sunlight absorption and one nanometer thick photovoltaics using two-dimensional monolayer materials," *Nano Letters*, vol. 13, no. 8, pp. 3664–3670, 2013.

[129] O. Lopez-Sanchez, D. Lembke, M. Kayci, A. Radenovic, and A. Kis, "Ultrasensitive photodetectors based on monolayer mos 2," *Nature nanotechnology*, vol. 8, no. 7, p. 497, 2013.

[130] S. M. Sze and M. K. Lee, *Semiconductor Physics and Devices*. Hoboken-N.J.: Wiley-Blackwell, 2012.

[131] S. D. Baranovskii, O. Rubel, and P. Thomas, "Theoretical description of hopping transport in disordered materials," *Thin Solid Films*, vol. 487, no. 1-2, pp. 2–7, 2005.

[132] C. Tanase, E. J. Meijer, P. W. M. Blom, and D. M. de Leeuw, "Unification of the hole transport in polymeric field-effect transistors and light-emitting diodes," *Physical Review Letters*, vol. 91, no. 21, 2003.

[133] R. H. Bube, "Photoconductivity," *Wiley Encyclopedia of Electrical and Electronics Engineering*, 1960.

[134] "Wikipedia: Transistor count." https://en.wikipedia.org/wiki/Transistor_count. Accessed: 20-07-18.

[135] G. E. Moore, "Ge moore, electronics 38, 114 (1965).," *Electronics*, vol. 38, p. 114, 1965.

[136] "Schematic of a mosfet." https://www.pinterest.ca/pin/414401603188468938/. Accessed: 30-07-18.

[137] R. J. E. Hueting, T. Van Hemert, B. Kaleli, R. A. M. Wolters, and J. Schmitz, "On device architectures, subthreshold swing, and power consumption of the piezoelectric field-effect transistor (<inline-formula> <tex-math notation="latex">π </tex-math></inline-formula>-fet)," *IEEE Journal of the Electron Devices Society*, vol. 3, no. 3, pp. 149–157, 2015.

[138] C. Auth, C. Allen, A. Blattner, D. Bergstrom, M. Brazier, M. Bost, M. Buehler, V. Chikarmane, T. Ghani, T. Glassman, T. Troeger, C. Weber, P. Yashar, K. Zawadzki, and K. Mistry, "A 22nm high performance and low-power cmos technology featuring fully-depleted tri-gate transistors, self-aligned contacts and high density mim capacitors," pp. 131–132, 2012.

[139] F. A. McGuire, Y.-C. Lin, K. Price, G. B. Rayner, S. Khandelwal, S. Salahuddin, and A. D. Franklin, "Sustained sub-60 mv/decade switching via the negative capacitance effect in mos2 transistors," *Nano Letters*, vol. 17, no. 8, pp. 4801–4806, 2017.

[140] A. F. Diaz and J. I. Castillo, "A polymer electrode with variable conductivity: polypyrrole," *Journal of the Chemical Society, Chemical Communications*, no. 9, p. 397, 1980.

[141] S. H. Kim, K. Hong, W. Xie, K. H. Lee, S. Zhang, T. P. Lodge, and C. D. Frisbie, "Electrolyte-gated transistors for organic and printed electronics," *Advanced Materials*, vol. 25, no. 13, pp. 1822–1846, 2013.

[142] J. Rivnay, S. Inal, A. Salleo, R. M. Owens, M. Berggren, and G. G. Malliaras, "Organic electrochemical transistors," *Nature Reviews Materials*, vol. 3, no. 2, p. 17086, 2018.

[143] H. Ohno, *Electrochemical Aspects of Ionic Liquids*. New York: Wiley & Sons, 2005.

[144] N. V. Plechkova and K. R. Seddon, "Applications of ionic liquids in the chemical industry," *Chemical Society Reviews*, vol. 37, no. 1, pp. 123–150, 2008.

[145] M. V. Fedorov and A. A. Kornyshev, "Ionic liquids at electrified interfaces," *Chemical Reviews*, vol. 114, no. 5, pp. 2978–3036, 2014.

[146] S. Chen, K. Wen, J. Fan, Y. Bando, and D. Golberg, "Progress and prospective on high voltage and safety electrolytes in advanced lithium batteries: from liquid to solid," *Journal of Materials Chemistry A*, 2018.

[147] A. Tsumura, H. Koezuka, and T. Ando, "Macromolecular electronic device: Field-effect transistor with a polythiophene thin film," *Applied Physics Letters*, vol. 49, no. 18, pp. 1210–1212, 1986.

[148] Y. L. Li, *Organic Optoelectronic Materials*. Lecture Notes in Chemistry, Springer International Publishing, 2015.

[149] C. Wang, H. Dong, W. Hu, Y. Liu, and D. Zhu, "Semiconducting π-conjugated systems in field-effect transistors: A material odyssey of organic electronics," *Chemical Reviews*, vol. 112, no. 4, pp. 2208–2267, 2012.

[150] A. Nawaz, M. S. Meruvia, D. L. Tarange, S. P. Gopinathan, A. Kumar, A. Kumar, H. Bhunia, A. J. Pal, and I. A. Hümmelgen, "High mobility organic field-effect transistors based on defect-free regioregular poly(3-hexylthiophene-2,5-diyl)," *Organic Electronics*, vol. 38, pp. 89–96, 2016.

[151] H. Zhao, Z. Wang, G. Dong, and L. Duan, "Fabrication of highly oriented large-scale tips pentacene crystals and transistors by the marangoni effect-controlled growth method," *Physical Chemistry Chemical Physics*, vol. 17, no. 9, pp. 6274–6279, 2015.

[152] G. Giri, E. Verploegen, S. C. B. Mannsfeld, S. Atahan-Evrenk, D. H. Kim, S. Y. Lee, H. A. Becerril, A. Aspuru-Guzik, M. F. Toney, and Z. Bao, "Tuning charge transport in solution-sheared organic semiconductors using lattice strain," *Nature*, vol. 480, no. 7378, pp. 504–508, 2011.

[153] H. Minemawari, T. Yamada, H. Matsui, J. y. Tsutsumi, S. Haas, R. Chiba, R. Kumai, and T. Hasegawa, "Inkjet printing of single-crystal films," *Nature*, vol. 475, no. 7356, pp. 364–367, 2011.

[154] H. Iino, T. Usui, and J.-i. Hanna, "Liquid crystals for organic thin-film transistors," *Nature Communications*, vol. 6, p. 6828, 2015.

[155] H. Dong, X. Fu, J. Liu, Z. Wang, and W. Hu, "25th anniversary article: Key points for high-mobility organic field-effect transistors," *Advanced Materials*, vol. 25, no. 43, pp. 6158–6183, 2013.

[156] H. Sirringhaus, "25th anniversary article: Organic field-effect transistors: The path beyond amorphous silicon," *Advanced Materials*, vol. 26, no. 9, pp. 1319–1335, 2014.

[157] D. Natali and M. Caironi, "Charge injection in solution-processed organic field-effect transistors: Physics, models and characterization methods," *Advanced Materials*, vol. 24, no. 11, pp. 1357–1387, 2012.

[158] J. C. Blakesley, F. A. Castro, W. Kylberg, G. F. A. Dibb, C. Arantes, R. Valaski, M. Cremona, J. S. Kim, and J.-S. Kim, "Towards reliable charge-mobility benchmark measurements for organic semiconductors," *Organic Electronics*, vol. 15, no. 6, pp. 1263–1272, 2014.

[159] C. Jongwan, S. Heeseok, K. Nakjoong, and K. Felix Sunjoo, "Development of n-type polymer semiconductors for organic field-effect transistors," *Semiconductor Science and Technology*, vol. 30, no. 6, p. 064002, 2015.

[160] J. E. Northrup and M. L. Chabinyc, "Gap states in organic semiconductors: Hydrogen- and oxygen-induced states in pentacene," *Physical Review B*, vol. 68, no. 4, p. 041202, 2003.

[161] T. Hallam, C. Duffy, T. Minakata, M. Ando, and H. Sirringhaus, "A scanning kelvin probe study of charge trapping in zone-cast pentacene thin film transistors," *Nanotechnology*, vol. 20, no. 2, p. 025203, 2009.

[162] M. Singh, H. M. Haverinen, P. Dhagat, and G. E. Jabbour, "Inkjet printing—process and its applications," *Advanced Materials*, vol. 22, no. 6, pp. 673–685, 2010.

[163] S. Logothetidis, "Flexible organic electronic devices: Materials, process and applications," *Materials Science and Engineering: B*, vol. 152, no. 1-3, pp. 96–104, 2008.

[164] C. T. White and T. N. Todorov, "Carbon nanotubes as long ballistic conductors," *Nature*, vol. 393, no. 6682, pp. 240–242, 1998.

[165] G. S. Tulevski, A. D. Franklin, D. Frank, J. M. Lobez, Q. Cao, H. Park, A. Afzali, S.-J. Han, J. B. Hannon, and W. Haensch, "Toward high-performance digital logic technology with carbon nanotubes," *ACS Nano*, vol. 8, no. 9, pp. 8730–8745, 2014.

[166] J. Zaumseil, "Single-walled carbon nanotube networks for flexible and printed electronics," *Semiconductor Science and Technology*, vol. 30, no. 7, p. 074001, 2015.

[167] T. Takeshi, J. Hehua, M. Yasumitsu, and K. Hiromichi, "High-yield separation of metallic and semiconducting single-wall carbon nanotubes by agarose gel electrophoresis," *Applied Physics Express*, vol. 1, no. 11, p. 114001, 2008.

[168] M. S. Arnold, A. A. Green, J. F. Hulvat, S. I. Stupp, and M. C. Hersam, "Sorting carbon nanotubes by electronic structure using density differentiation," *Nat Nano*, vol. 1, no. 1, pp. 60–65, 2006.

[169] S. Ghosh, S. M. Bachilo, and R. B. Weisman, "Advanced sorting of single-walled carbon nanotubes by nonlinear density-gradient ultracentrifugation," *Nat Nano*, vol. 5, no. 6, pp. 443–450, 2010.

[170] H. Liu, D. Nishide, T. Tanaka, and H. Kataura, "Large-scale single-chirality separation of single-wall carbon nanotubes by simple gel chromatography," *Nature Communications*, vol. 2, p. 309, 2011.

[171] C. Kocabas, N. Pimparkar, O. Yesilyurt, S. J. Kang, M. A. Alam, and J. A. Rogers, "Experimental and theoretical studies of transport through large scale, partially aligned arrays of single-walled carbon nanotubes in thin film type transistors," *Nano Letters*, vol. 7, no. 5, pp. 1195–1202, 2007.

[172] A. Graf, Y. Zakharko, S. P. Schießl, C. Backes, M. Pfohl, B. S. Flavel, and J. Zaumseil, "Large scale, selective dispersion of long single-walled carbon nanotubes with high photoluminescence quantum yield by shear force mixing," *Carbon*, vol. 105, pp. 593–599, 2016.

[173] A. D. Franklin, "Nanomaterials in transistors: From high-performance to thin-film applications," *Science*, vol. 349, no. 6249, p. aab2750, 2015.

[174] M. Zheng, "Sorting carbon nanotubes," *Topics in Current Chemistry*, vol. 375, no. 1, p. 13, 2017.

[175] L. Carbone and P. D. Cozzoli, "Colloidal heterostructured nanocrystals: Synthesis and growth mechanisms," *Nano Today*, vol. 5, no. 5, pp. 449–493, 2010.

[176] X. Peng, L. Manna, W. Yang, J. Wickham, E. Scher, A. Kadavanich, and A. P. Alivisatos, "Shape control of cdse nanocrystals," *Nature*, vol. 404, no. 6773, pp. 59–61, 2000.

[177] A. Nag, M. V. Kovalenko, J.-S. Lee, W. Liu, B. Spokoyny, and D. V. Talapin, "Metal-free inorganic ligands for colloidal nanocrystals: S2–, hs–, se2–, hse–, te2–, hte–, tes32–, oh–, and nh2–as surface ligands," *Journal of the American Chemical Society*, vol. 133, no. 27, pp. 10612–10620, 2011.

[178] D. V. Talapin, J.-S. Lee, M. V. Kovalenko, and E. V. Shevchenko, "Prospects of colloidal nanocrystals for electronic and optoelectronic applications," *Chemical Reviews*, vol. 110, no. 1, pp. 389–458, 2010.

[179] M. A. Rafiq, Y. Tsuchiya, H. Mizuta, S. Oda, S. Uno, Z. A. K. Durrani, and W. I. Milne, "Charge injection and trapping in silicon nanocrystals," *Applied Physics Letters*, vol. 87, no. 18, p. 182101, 2005.

[180] R. N. Pereira, S. Niesar, W. B. You, A. F. da Cunha, N. Erhard, A. R. Stegner, H. Wiggers, M. G. Willinger, M. Stutzmann, and M. S. Brandt, "Solution-processed networks of silicon nanocrystals: The role of internanocrystal medium on semiconducting behavior," *The Journal of Physical Chemistry C*, vol. 115, no. 41, pp. 20120–20127, 2011.

[181] K. Szendrei, M. Speirs, W. Gomulya, D. Jarzab, M. Manca, O. V. Mikhnenko, M. Yarema, B. J. Kooi, W. Heiss, and M. A. Loi, "Exploring the origin of the temperature-dependent behavior of pbs nanocrystal thin films and solar cells," *Advanced Functional Materials*, vol. 22, no. 8, pp. 1598–1605, 2012.

[182] J.-S. Lee, M. V. Kovalenko, J. Huang, D. S. Chung, and D. V. Talapin, "Band-like transport, high electron mobility and high photoconductivity in all-inorganic nanocrystal arrays," *Nat Nano*, vol. 6, no. 6, pp. 348–352, 2011.

[183] D. K. Kim, Y. Lai, B. T. Diroll, C. B. Murray, and C. R. Kagan, "Flexible and low-voltage integrated circuits constructed from high-performance nanocrystal transistors," *Nature communications*, vol. 3, p. 1216, 2012.

[184] W. Aigner, M. Wiesinger, H. Wiggers, M. Stutzmann, and R. N. Pereira, "Three-dimensional percolation and performance of nanocrystal field-effect transistors," *Physical Review Applied*, vol. 5, no. 5, p. 054017, 2016.

[185] S. Weis, R. Körmer, M. P. M. Jank, M. Lemberger, M. Otto, H. Ryssel, W. Peukert, and L. Frey, "Conduction mechanisms and environmental sensitivity of solution-processed silicon nanoparticle layers for thin-film transistors," *Small*, vol. 7, no. 20, pp. 2853–2857, 2011.

[186] K. H. Müller, G. Wei, B. Raguse, and J. Myers, "Three-dimensional percolation effect on electrical conductivity in films of metal nanoparticles linked by organic molecules," *Physical Review B*, vol. 68, no. 15, p. 155407, 2003.

[187] D. J. Finn, M. Lotya, G. Cunningham, R. J. Smith, D. McCloskey, J. F. Donegan, and J. N. Coleman, "Inkjet deposition of liquid-exfoliated graphene and mos 2 nanosheets for printed device applications," *Journal of Materials Chemistry C*, vol. 2, no. 5, pp. 925–932, 2014.

[188] G. Hu, T. Albrow-Owen, X. Jin, A. Ali, Y. Hu, R. C. T. Howe, K. Shehzad, Z. Yang, X. Zhu, R. I. Woodward, T.-C. Wu, H. Jussila, J.-B. Wu, P. Peng, P.-H. Tan, Z. Sun, E. J. R. Kelleher, M. Zhang, Y. Xu, and T. Hasan, "Black phosphorus ink formulation for inkjet printing of optoelectronics and photonics," *Nature Communications*, vol. 8, no. 1, 2017.

[189] Y. G. Yao, L. Tolentino, Z. Z. Yang, X. J. Song, W. Zhang, Y. S. Chen, and C. P. Wong, "High-concentration aqueous dispersions of mos2," *Advanced Functional Materials*, vol. 23, no. 28, pp. 3577–3583, 2013.

[190] S.-Y. Cho, Y. Lee, H.-J. Koh, H. Jung, J.-S. Kim, H.-W. Yoo, J. Kim, and H.-T. Jung, "Superior chemical sensing performance of black phosphorus: Comparison with mos2and graphene," *Advanced Materials*, vol. 28, no. 32, pp. 7020–7028, 2016.

[191] C. Casiraghi, M. Macucci, K. Parvez, R. Worsley, Y. Shin, F. Bronte, C. Borri, M. Paggi, and G. Fiori, "Inkjet printed 2d-crystal based strain gauges on paper," *Carbon*, vol. 129, pp. 462–467, 2018.

[192] A. Y. Polyakov, L. Yadgarov, R. Popovitz-Biro, V. A. Lebedev, I. Pinkas, R. Rosentsveig, Y. Feldman, A. E. Goldt, E. A. Goodilin, and R. Tenne, "Decoration of ws2 nanotubes and fullerene-like mos2 with gold nanoparticles," *The Journal of Physical Chemistry C*, vol. 118, no. 4, pp. 2161–2169, 2014.

[193] S. S. Chou, M. De, J. Kim, S. Byun, C. Dykstra, J. Yu, J. Huang, and V. P. Dravid, "Ligand conjugation of chemically exfoliated mos2," *Journal of the American Chemical Society*, vol. 135, no. 12, pp. 4584–4587, 2013.

[194] S. Bertolazzi, M. Gobbi, Y. Zhao, C. Backes, and P. Samorì, "Molecular chemistry approaches for tuning the properties of two-dimensional transition metal dichalcogenides," *Chemical Society Reviews*, 2018.

[195] A. Heinrichsdobler, J. C. Roigk, F. Schirmeier, C. J. Brabec, and T. Wehlus, "Pinhole-free inkjet printing strategies for organic electronics," *Advanced Materials Technologies*, vol. 2, no. 12, p. 1700166, 2017.

[196] Z. Ding, R. Xing, Q. Fu, D. Ma, and Y. Han, "Patterning of pinhole free small molecular organic light-emitting films by ink-jet printing," *Organic Electronics*, vol. 12, no. 4, pp. 703–709, 2011.

[197] J. Zhu, X. Liu, M. L. Geier, J. J. McMorrow, D. Jariwala, M. E. Beck, W. Huang, T. J. Marks, and M. C. Hersam, "Layer-by-layer assembled 2d montmorillonite dielectrics for solution-processed electronics," *Advanced Materials*, vol. 28, no. 1, pp. 63–68, 2016.

[198] C. Backes, R. J. Smith, N. McEvoy, N. C. Berner, D. McCloskey, H. C. Nerl, A. O'Neill, P. J. King, T. Higgins, D. Hanlon, *et al.*, "Edge and confinement effects allow in situ measurement of size and thickness of liquid-exfoliated nanosheets," *Nature communications*, vol. 5, p. 4576, 2014.

[199] C. Backes, K. R. Paton, D. Hanlon, S. Yuan, M. I. Katsnelson, J. Houston, R. J. Smith, D. McCloskey, J. F. Donegan, and J. N. Coleman, "Spectroscopic metrics allow in

situ measurement of mean size and thickness of liquid-exfoliated few-layer graphene nanosheets," *Nanoscale*, vol. 8, no. 7, pp. 4311–4323, 2016.

[200] A. Harvey, C. Backes, Z. Gholamvand, D. Hanlon, D. McAteer, H. C. Nerl, E. McGuire, A. Seral-Ascaso, Q. M. Ramasse, N. McEvoy, *et al.*, "Preparation of gallium sulfide nanosheets by liquid exfoliation and their application as hydrogen evolution catalysts," *Chemistry of Materials*, vol. 27, no. 9, pp. 3483–3493, 2015.

[201] A. Griffin, A. Harvey, B. Cunningham, D. Scullion, T. Tian, C.-J. Shih, M. Gruening, J. F. Donegan, E. J. Santos, C. Backes, *et al.*, "Spectroscopic size and thickness metrics for liquid-exfoliated h-bn," *Chemistry of Materials*, vol. 30, no. 6, pp. 1998–2005, 2018.

[202] S. De and J. N. Coleman, "Are there fundamental limitations on the sheet resistance and transmittance of thin graphene films?," *ACS nano*, vol. 4, no. 5, pp. 2713–2720, 2010.

[203] J. C. Slonczewski and P. R. Weiss, "Band structure of graphite," *Physical Review*, vol. 109, no. 2, pp. 272–279, 1958.

[204] G. Cunningham, D. Hanlon, N. McEvoy, G. S. Duesberg, and J. N. Coleman, "Large variations in both dark-and photoconductivity in nanosheet networks as nanomaterial is varied from mos 2 to wte 2," *Nanoscale*, vol. 7, no. 1, pp. 198–208, 2015.

[205] K. K. Kim, A. Hsu, X. Jia, S. M. Kim, Y. Shi, M. Dresselhaus, T. Palacios, and J. Kong, "Synthesis and characterization of hexagonal boron nitride film as a dielectric layer for graphene devices," *ACS nano*, vol. 6, no. 10, pp. 8583–8590, 2012.

[206] P. N. Nirmalraj, T. Lutz, S. Kumar, G. S. Duesberg, and J. J. Boland, "Nanoscale mapping of electrical resistivity and connectivity in graphene strips and networks," *Nano letters*, vol. 11, no. 1, pp. 16–22, 2010.

[207] S. Barwich, U. Khan, and J. N. Coleman, "A technique to pretreat graphite which allows the rapid dispersion of defect-free graphene in solvents at high concentration," *The Journal of Physical Chemistry C*, vol. 117, no. 37, pp. 19212–19218, 2013.

[208] F. Withers, H. Yang, L. Britnell, A. Rooney, E. Lewis, A. Felten, C. Woods, V. Sanchez Romaguera, T. Georgiou, A. Eckmann, *et al.*, "Heterostructures produced from nanosheet-based inks," *Nano letters*, vol. 14, no. 7, pp. 3987–3992, 2014.

[209] M. J. Panzer, C. R. Newman, and C. D. Frisbie, "Low-voltage operation of a pentacene field-effect transistor with a polymer electrolyte gate dielectric," *Applied Physics Letters*, vol. 86, no. 10, p. 103503, 2005.

[210] M. S. Kang, J. Lee, D. J. Norris, and C. D. Frisbie, "High carrier densities achieved at low voltages in ambipolar pbse nanocrystal thin-film transistors," *Nano letters*, vol. 9, no. 11, pp. 3848–3852, 2009.

[211] Z. Gholamvand, D. McAteer, A. Harvey, C. Backes, and J. N. Coleman, "Electrochemical applications of two-dimensional nanosheets: The effect of nanosheet length and thickness," *Chemistry of Materials*, vol. 28, no. 8, pp. 2641–2651, 2016.

[212] B. Kolodziejczyk, C. H. Ng, X. Strakosas, G. G. Malliaras, and B. Winther-Jensen, "Light sensors and opto-logic gates based on organic electrochemical transistors," *Materials Horizons*, vol. 5, no. 1, pp. 93–98, 2018.

[213] D. Khodagholy, J. Rivnay, M. Sessolo, M. Gurfinkel, P. Leleux, L. H. Jimison, E. Stavrinidou, T. Herve, S. Sanaur, R. M. Owens, *et al.*, "High transconductance organic electrochemical transistors," *Nature communications*, vol. 4, p. 2133, 2013.

[214] C. Jarrett, R. Friend, A. Brown, and D. De Leeuw, "Field effect measurements in doped conjugated polymer films: Assessment of charge carrier mobilities," *Journal of applied physics*, vol. 77, no. 12, pp. 6289–6294, 1995.

[215] Y. Wen and Y. Liu, "Recent progress in n-channel organic thin-film transistors," *Advanced Materials*, vol. 22, no. 12, pp. 1331–1345, 2010.

[216] W. H. Evers, J. M. Schins, M. Aerts, A. Kulkarni, P. Capiod, M. Berthe, B. Grandidier, C. Delerue, H. S. Van Der Zant, C. Van Overbeek, *et al.*, "High charge mobility in two-dimensional percolative networks of pbse quantum dots connected by atomic bonds," *Nature communications*, vol. 6, p. 8195, 2015.

[217] L. T. Kunneman, J. M. Schins, S. Pedetti, H. Heuclin, F. C. Grozema, A. J. Houtepen, B. Dubertret, and L. D. Siebbeles, "Nature and decay pathways of photoexcited states in cdse and cdse/cds nanoplatelets," *Nano letters*, vol. 14, no. 12, pp. 7039–7045, 2014.

[218] T. Ozel, A. Gaur, J. A. Rogers, and M. Shim, "Polymer electrolyte gating of carbon nanotube network transistors," *Nano letters*, vol. 5, no. 5, pp. 905–911, 2005.

[219] T. M. Higgins and J. N. Coleman, "Avoiding resistance limitations in high-performance transparent supercapacitor electrodes based on large-area, high-conductivity pedot: Pss films," *ACS applied materials & interfaces*, vol. 7, no. 30, pp. 16495–16506, 2015.

[220] A. Zabet-Khosousi and A.-A. Dhirani, "Charge transport in nanoparticle assemblies," *Chemical reviews*, vol. 108, no. 10, pp. 4072–4124, 2008.

[221] M. J. Hostetler, A. C. Templeton, and R. W. Murray, "Dynamics of place-exchange reactions on monolayer-protected gold cluster molecules," *Langmuir*, vol. 15, no. 11, pp. 3782–3789, 1999.

[222] N. Gaponik, D. V. Talapin, A. L. Rogach, A. Eychmüller, and H. Weller, "Efficient phase transfer of luminescent thiol-capped nanocrystals: from water to nonpolar organic solvents," *Nano Letters*, vol. 2, no. 8, pp. 803–806, 2002.

[223] J. R. Dunklin, P. Lafargue, T. M. Higgins, G. T. Forcherio, M. Benamara, N. McEvoy, D. K. Roper, J. N. Coleman, Y. Vaynzof, and C. Backes, "Production of monolayer-rich gold-decorated 2h–ws 2 nanosheets by defect engineering," *npj 2D Materials and Applications*, vol. 1, no. 1, p. 43, 2018.

[224] S. R. Pathipati, E. Pavlica, A. Schlierf, M. El Gemayel, P. Samorì, V. Palermo, and G. Bratina, "Graphene-induced enhancement of n-type mobility in perylenediimide thin films," *The Journal of Physical Chemistry C*, vol. 118, no. 43, pp. 24819–24826, 2014.

[225] G. Cunningham, M. Lotya, N. McEvoy, G. S. Duesberg, P. van der Schoot, and J. N. Coleman, "Percolation scaling in composites of exfoliated mos 2 filled with nanotubes and graphene," *Nanoscale*, vol. 4, no. 20, pp. 6260–6264, 2012.

[226] J. Ahn, P. J. Jeon, S. R. A. Raza, A. Pezeshki, S.-W. Min, D. K. Hwang, and S. Im, "Transition metal dichalcogenide heterojunction pn diode toward ultimate photovoltaic benefits," *2D Materials*, vol. 3, no. 4, p. 045011, 2016.

[227] Y. Liu, P. Stradins, and S.-H. Wei, "Van der waals metal-semiconductor junction: Weak fermi level pinning enables effective tuning of schottky barrier," *Science advances*, vol. 2, no. 4, p. e1600069, 2016.

[228] H. Hibino, H. Kageshima, M. Kotsugi, F. Maeda, F.-Z. Guo, and Y. Watanabe, "Dependence of electronic properties of epitaxial few-layer graphene on the number of layers investigated by photoelectron emission microscopy," *Physical Review B*, vol. 79, no. 12, p. 125437, 2009.

[229] R. Schlaf, O. Lang, C. Pettenkofer, and W. Jaegermann, "Band lineup of layered semiconductor heterointerfaces prepared by van der waals epitaxy: Charge transfer correction term for the electron affinity rule," *Journal of applied physics*, vol. 85, no. 5, pp. 2732–2753, 1999.

[230] H. Tian, Z. Tan, C. Wu, X. Wang, M. A. Mohammad, D. Xie, Y. Yang, J. Wang, L.-J. Li, J. Xu, *et al.*, "Novel field-effect schottky barrier transistors based on graphene-mos 2 heterojunctions," *Scientific reports*, vol. 4, p. 5951, 2014.

[231] W. Bauhofer and J. Z. Kovacs, "A review and analysis of electrical percolation in carbon nanotube polymer composites," *Composites Science and Technology*, vol. 69, no. 10, pp. 1486–1498, 2009.

[232] D. Stauffer and A. Aharony, *Introduction to percolation theory: revised second edition*. CRC press, 2014.

[233] J. Clerc, G. Giraud, J. Laugier, and J. Luck, "The electrical conductivity of binary disordered systems, percolation clusters, fractals and related models," *Advances in Physics*, vol. 39, no. 3, pp. 191–309, 1990.

[234] C. Chiteme, D. McLachlan, and G. Sauti, "Ac and dc percolative conductivity of magnetite-cellulose acetate composites," *Physical Review B*, vol. 75, no. 9, p. 094202, 2007.

[235] S. Stankovich, D. A. Dikin, G. H. Dommett, K. M. Kohlhaas, E. J. Zimney, E. A. Stach, R. D. Piner, S. T. Nguyen, and R. S. Ruoff, "Graphene-based composite materials," *nature*, vol. 442, no. 7100, p. 282, 2006.

[236] H.-x. Tan and X.-c. Xu, "Conductive properties and mechanisms of different polymers doped by carbon nanotube/polypyrrole 1d hybrid nanotubes," *RSC Advances*, vol. 5, no. 75, pp. 61383–61389, 2015.

[237] K.-J. Baeg, M. Caironi, and Y.-Y. Noh, "Toward printed integrated circuits based on unipolar or ambipolar polymer semiconductors," *Advanced Materials*, vol. 25, no. 31, pp. 4210–4244, 2013.

[238] E. B. Secor, T. Z. Gao, A. E. Islam, R. Rao, S. G. Wallace, J. Zhu, K. W. Putz, B. Maruyama, and M. C. Hersam, "Enhanced conductivity, adhesion, and environmental stability of printed graphene inks with nitrocellulose," *Chemistry of Materials*, vol. 29, no. 5, pp. 2332–2340, 2017.

[239] J. Li, F. Ye, S. Vaziri, M. Muhammed, M. C. Lemme, and M. Östling, "Efficient inkjet printing of graphene," *Advanced materials*, vol. 25, no. 29, pp. 3985–3992, 2013.

[240] S. Lim, B. Kang, D. Kwak, W. H. Lee, J. A. Lim, and K. Cho, "Inkjet-printed reduced graphene oxide/poly (vinyl alcohol) composite electrodes for flexible transparent organic field-effect transistors," *The Journal of Physical Chemistry C*, vol. 116, no. 13, pp. 7520–7525, 2012.

[241] J. Perelaer, R. Abbel, S. Wünscher, R. Jani, T. van Lammeren, and U. S. Schubert, "Roll-to-roll compatible sintering of inkjet printed features by photonic and microwave exposure: from non-conductive ink to 40% bulk silver conductivity in less than 15 seconds," *Advanced materials*, vol. 24, no. 19, pp. 2620–2625, 2012.

[242] C. Gabbett, C. S. Boland, A. Harvey, V. Vega-Mayoral, R. J. Young, and J. N. Coleman, "The effect of network formation on the mechanical properties of 1d: 2d nano: nano composites," *Chemistry of Materials*, 2018.

[243] Y. Liu, X. He, D. Hanlon, A. Harvey, U. Khan, Y. Li, and J. N. Coleman, "Electrical, mechanical, and capacity percolation leads to high-performance mos2/nanotube composite lithium ion battery electrodes," *ACS nano*, vol. 10, no. 6, pp. 5980–5990, 2016.

[244] G. Lota, K. Fic, and E. Frackowiak, "Carbon nanotubes and their composites in electrochemical applications," *Energy & Environmental Science*, vol. 4, no. 5, pp. 1592–1605, 2011.

[245] X. Huang, Z. Zeng, S. Bao, M. Wang, X. Qi, Z. Fan, and H. Zhang, "Solution-phase epitaxial growth of noble metal nanostructures on dispersible single-layer molybdenum disulfide nanosheets," *Nature communications*, vol. 4, p. 1444, 2013.

[246] L. Yuwen, F. Xu, B. Xue, Z. Luo, Q. Zhang, B. Bao, S. Su, L. Weng, W. Huang, and L. Wang, "General synthesis of noble metal (au, ag, pd, pt) nanocrystal modified mos 2 nanosheets and the enhanced catalytic activity of pd–mos 2 for methanol oxidation," *Nanoscale*, vol. 6, no. 11, pp. 5762–5769, 2014.

[247] H. Lee, S. Bak, S.-J. An, J. H. Kim, E. Yun, M. Kim, S. Seo, M. S. Jeong, and H. Lee, "Highly efficient thin-film transistor via cross-linking of 1t edge functional 2h molybdenum disulfides," *ACS nano*, vol. 11, no. 12, pp. 12832–12839, 2017.

[248] B. Clark, T. Frost, and M. Russell, *UV Spectroscopy: Techniques, instrumentation and data handling*, vol. 4. Springer Science & Business Media, 1993.

[249] Varian/Agilent, *Cary 6000i User Manual*, vol. 1. Varian/Agilent, 2012.

[250] A. C. Ferrari and D. M. Basko, "Raman spectroscopy as a versatile tool for studying the properties of graphene," *Nature nanotechnology*, vol. 8, no. 4, p. 235, 2013.

[251] M. Lotya, *PhD Thesis: Investigation of Multiferroic and Photocatalytic Properties of Li-doped $BiFeO_3$ Nanoparticles Prepared By Ultrasonication*, vol. 1. Trinity College Dublin, 2012.

[252] R. L. McCreery, *Raman spectroscopy for chemical analysis*, vol. 225. John Wiley & Sons, 2005.

[253] P. Eaton and P. West, *Atomic force microscopy*. Oxford University Press, 2010.

[254] "Image of a tem column." http://www.hk-phy.org/atomic_world/tem/tem02_e.html. Accessed: 30-07-18.

[255] R. F. Egerton *et al.*, *Physical principles of electron microscopy*. Springer, 2005.

[256] A. A. Billah, *Master's Thesis: Exfoliation and Dispersion of Layered Materials Through Liquid-Phase Processing*, vol. 1. Bangladesh University of Engineering and Technology, 2014.

[257] W. Zhou and Z. L. Wang, *Scanning microscopy for nanotechnology: techniques and applications*. Springer science & business media, 2007.